

**EVALUATING REPRODUCIBILITY
AND ACCURACY OF
HYPERSENSITRAL MINERAL
MAPS USING MULTI-TEMPORAL
AVIRIS IMAGES OF CUPRITE,
NEVADA, USA**

TINGXUAN JIANG
FEBRUARY 2019

SUPERVISORS:
Prof. Dr. Freek van der Meer
Dr. H. M. A van der Werff



EVALUATING REPRODUCIBILITY AND ACCURACY OF HYPERSENSPECTRAL MINERAL MAPS USING MULTI-TEMPORAL AVIRIS IMAGES OF CUPRITE, NEVADA, USA

TINGXUAN JIANG

Enschede, The Netherlands, February, 2019

Thesis submitted to the Faculty of Geo-Information Science and Earth Observation of the University of Twente in partial fulfilment of the requirements for the degree of Master of Science in Geo-information Science and Earth Observation.

Specialization: [Applied Earth Sciences]

SUPERVISORS:

Prof. Dr. Freek van der Meer

Dr. H. M. A van der Werff

THESIS ASSESSMENT BOARD:

Prof. Dr. N. Kerle (Chair)

Dr. Mike Buxton (External Examiner, Technical University Delft)

DISCLAIMER

This document describes work undertaken as part of a programme of study at the Faculty of Geo-Information Science and Earth Observation of the University of Twente. All views and opinions expressed therein remain the sole responsibility of the author, and do not necessarily represent those of the Faculty.

ABSTRACT

Hyperspectral remote sensing is one of the frequently used tools and techniques for geologic exploration of mineral resources. The product of a hyperspectral study often is a mineral map whose accuracy needs to be validated. The existing accuracy assessment system for hyperspectral products is unstandardized and relies on ground truth data. To fill this niche, this research proposed an idea that the reproducibility and/or consistency of mineral-maps derived from multitemporal hyperspectral images over the same area may be correlated with the accuracy of their classification results. This idea depends on the fact that the mineral distribution barely changed during a short period of time. Therefore, the aim of this research was to measure the reproducibility of hyperspectral mineral maps, investigate assumed factors (*e.g.* vegetation cover, different spectral endmembers, and classification threshold) that may disturb reproducibility and estimate the relationship between reproducibility and accuracy of hyperspectral classification.

In this study, three multitemporal AVIRIS scenes acquired in May 2006, September 2008 and October 2010 respectively and over the Cuprite, Nevada, USA were used for hyperspectral mineral mapping. These three scenes were subsetting then classified by Spectral Angle Mapper (SAM) with the spectral endmembers extracted from the images using both various threshold and the unique threshold. Mask tool was used to mask out the pixels that have vastly different values (more than ± 100 for reflectance) between the 3 pairs of images (May image and Sep image, May image and Oct image, as well as Sep image and Oct image). This process resulted in similarized images then these similarized images were classified by the various threshold set of SAM and the extracted endmembers to create new mineral maps. The Normalized Difference Vegetation Index (NDVI) was used to analyse the vegetation cover in the study area. Universal endmembers were created by averaging the three set of extracted endmember libraries and these were used to create minerals maps from the original images. Subsequently, all the classification results were compared to investigate reproducibility and the factors that affect it. Eventually, the reproduced classification results were compared with the ground truth to assess the accuracy of classification.

The classification results created by the extracted endmembers with the various thresholds shown reproducibility around 60%. However, the classification results created with the extracted endmembers and the unique threshold shown poor classification. The similarity of identified classes between mineral maps derived from the similarized May image and similarized Sep image is around 23%, between mineral maps derived from the similarized May image and similarized Oct image is around 50%, between mineral maps derived from the similarized Sep image and similarized Oct image is around 48%. On the contrary, the similarity of identified classes between mineral maps derived from the original images is around 22%. The reproducibility of mineral maps that created with the same set of the universal spectral endmembers is around 85%. The comparisons between the producer's accuracy of mineral maps that were created with the universal endmembers and reproducibility of the same set of maps shown a similar variation for every single mineral. Higher ratios of reproducibility indicated that differences of the original hyperspectral scenes and the differences amongst different endmember libraries influenced the reproducibility of hyperspectral mineral maps. The presence of similar variations in trend between the reproducibility and producer's accuracy shown the potential of using reproducibility to assess the hyperspectral classification accuracy.

ACKNOWLEDGEMENTS

I would like to offer my special thanks to my MSc thesis supervisors, Prof. Dr. Freek van der Meer and Dr. Harald van der Werff for their consistent guidance and patience as well as for the motivation to always improve my work. It is impossible to finish this work without their support. It was a pleasure to work with these great and kind supervisors.

I would like to thank Dr. Caroline Lievens for her support during the proposal step of this research.

I would like to express my thanks to Wim Bakker for his suggestions and help about HypPy software. I would also like to extend my thanks to Dr. Chris Hecker for his suggestions about classification.

I would like to thank our course coordinator Bart Krol who is always friendly support me during my study in the ITC.

I am grateful, to Amarjargal Davaadorj, Oroghene Oluwadara Chokor, and my other best classmates whose help and suggestion never left me.

Special thanks to Mr Ludwig van Beethoven whose compositions always give me strength and courage before the dawn.

Finally, I would like to thank my families who always give me support and encouragement all along my MSc study.

TABLE OF CONTENTS

1. INTRODUCTION.....	9
1.1. Background.....	9
1.2. Problem Statement.....	10
1.3. Main-assumption.....	10
1.4. Objectives and research questions.....	10
1.4.1. General objective.....	10
1.4.2. Specific objectives.....	10
1.4.3. Research questions.....	11
1.5. Thesis structure.....	11
2. DATA AND METHODOLOGY.....	12
2.1. Data.....	12
2.1.1. Study area.....	12
2.1.2. Remote sensing data.....	13
2.1.3. Ground truth data.....	14
2.2. Pre-processing.....	15
2.2.1. Atmospheric correction.....	15
2.2.2. Data resize.....	16
2.2.3. Geocoding.....	17
2.2.4. Region of interest (ROI).....	17
2.3. Processing.....	17
2.3.1. Wavelength mapping.....	17
2.3.2. Spatial-spectral endmember extraction (SSEE).....	18
2.3.3. Spectral correlation.....	19
2.3.4. Spectral angle mapper (SAM).....	19
2.3.5. Image-to-image registration.....	20
2.3.6. Confusion matrix.....	21
2.3.7. Masks.....	21
2.3.8. Change detection (CD).....	22
2.3.9. Similarization.....	23
2.3.10. Identification similarity.....	23
2.3.11. Normalized difference vegetation index (NDVI).....	23
3. RESULT.....	26
3.1. Atmospheric correction.....	26
3.2. Data resize.....	27
3.3. Wavelength mapping.....	27
3.4. Endmember extraction.....	30
3.5. Endmember similarity.....	31
3.6. Image-to-image registration.....	32
3.7. Measurement of the reproducibility.....	33

3.7.1. Mineral maps produced through the extracted endmember library	33
3.7.2. Maps classified by the unique threshold	36
3.7.3. Differences amongst the original images.....	37
3.7.4. Influence of vegetation	43
3.7.5. Influence of endmember library.....	45
3.7.6. Comparison between solo mineral maps.....	48
3.8. Accuracy assessment	51
3.8.1. Comparison between the classification results and the Cuprite Mineral Map.....	51
3.8.2. Comparison between the classification results and the wavelength map	55
3.9. The relationship between reproducibility and correctness	56
4. DISCUSSION	58
5. CONCLUSION AND RECOMMENDATION	62
6. APPENDICES.....	69

LIST OF FIGURES

Figure 2.1 Cuprite, Nevada 1995 AVIRIS Data Mineral Map Clays, Micas, Sulphates, Carbs (Source: Swayze et al., 2014) The red box shows the study area of this MSc research.....	14
Figure 2.2 Settings used for atmospheric correction of May image of model FLAASH in software ENVI	16
Figure 2.3 (A) shows the original condition of a solo mineral map; (B) presents the values of pixels of the mask file when pixels of (A) excluded by the it with the characteristic as value equal to “zero”; (C) shows the value “one” in each pixel of the original solo mineral maps is changed to the value “two”. It is because each pixel that have value as “zero” in a mask file then the value of its spatially corresponding pixel of the original image can be exchanged through the tool “applying mask”.....	21
Figure 2.4 (A) shows the original condition of a solo mineral map; (B) presents the values of pixels of the mask file when pixels of (A) excluded by the it with the characteristic as value equal to “zero”; (C) shows the value “one” in each pixel of the original solo mineral maps is changed to the value “two”. It is because each pixel that have value as “zero” in a mask file then the value of its spatially corresponding pixel of the original image can be exchanged through the tool “applying mask”.....	21
Figure 2.5 (A) shows the distribution of the pixels whose value is “two” of the “initial stat” image; similarly, (B) shows the distribution of the pixels whose value is “one” of the “final stat” image; (C) presents the result when the value of pixels of the “final state” image subtracts the value of their corresponding pixels in the “initial state” image. Meanwhile, the “initial state” image was assumed as the reference data while the “final state” image was assumed as the test data. Therefore, in graph (C), “-2” presents omission, “-1” shows that pixel was classified in both of these two mineral maps, “0” presents that pixel was not identified in both of the solo maps, and “1” indicates that pixel should be labelled as commission.....	22
Figure 3.1 (A) shows the comparison of overall spectra derived from May, Sep, and Oct image, before and after the atmospheric correction respectively.; (B) presents the comparison of overall spectra whose wavelength is 2000 - 2500nm derived from May, Sep, and Oct image, before and after the atmospheric correction respectively. Which is also the spectra surrounded by a dark outline of Figure 3.1 (A).....	26
Figure 3.2 (A), (B), and (C) shows the comparison between spectra collected from May, Sep, and Oct image respectively and their corresponding mineral spectrum from the USGS library. For the comparison of each mineral, the upper spectrum is referenced from the USGS spectral library while the lower one was collected from the images.....	27
Figure 3.3 frequency for the wavelength position of the first peak	28
Figure 3.4 (A) shows the wavelength map derived from May image; (B) is the wavelength map produced based on the Sep image; (C) presents the wavelength map created depends on the Oct image.	28
Figure 3.5 Reflectance images generated in pre-processing.....	29
Figure 3.6 Spectral endmember libraries used in this research & legend.....	30
Figure 3.7 (A) shows the GCPs distribution of Sep image; (B) shows the GCPs distribution upon the Oct image.....	32
Figure 3.8 (A), (B), and (C) are SAM classification results, that were classified though the extracted endmember libraries and one set of various thresholds, derived from May image, Sep image, and Oct image respectively.	33

Figure 3.9 (A), (B), and (C) are SAM classification results, that were classified through the extracted endmember libraries and “0.1” as threshold for every mineral, derived from May image, Sep image, and Oct image respectively.....	36
Figure 3.10 Differences maps generated by the change detection, of which (A) shows the differences between May image and Sep image; (B) presents the differences between Sep image and Oct image; (C) shows the differences between May image and Oct image; the different value from positive to negative was present from lighter red to dimmer blue in this map.	37
Figure 3.11 Comparison of identification similarity between results derived from the original images and the results derived from the similarized images.	38
Figure 3.12 (A) shows the classification result derived from the May-Sep image; (B) shows the classification result derived from the Sep-May image; (C) shows the classification result derived from the May-Oct image; (D) shows the classification result derived from the Oct-May image; (E) shows the classification result derived from the Sep-Oct image; (F) shows the classification result derived from the Oct-Sep image.....	42
Figure 3.13 (A), (B), and (C) presents the classified NDVI results that derived from May image, Sep image, and Oct image respectively.	43
Figure 3.14 Vegetation distribution in May image.....	44
Figure 3.15 vegetation distribution in Oct image.....	Error! Bookmark not defined.
Figure 3.16 Vegetation distribution in Sep image.....	Error! Bookmark not defined.
Figure 3.17 (A), (B), and (C) are SAM classification results, that were classified through the universal endmember library and one set of various threshold, derived from May image, Sep image, and Oct image respectively.	45
Figure 3.18 Reproducibility of solo maps classified with the universal endmember libraries	48
Figure 3.19 (A) show the different distribution of Alunite between reproduced mineral maps derived from May and Sep image; (B) show the different distribution of Alunite between reproduced mineral maps derived from May and Oct image; (C) show the different distribution of Alunite between reproduced mineral maps derived from Sep and Oct image; (D) show the different distribution of Buddingtonite between reproduced mineral maps derived from May and Sep image; (E) show the different distribution of Buddingtonite between reproduced mineral maps derived from May and Oct image; (F) show the different distribution of Buddingtonite between reproduced mineral maps derived from Sep and Oct image; (G) show the different distribution of Kaolinite between reproduced mineral maps derived from May and Sep image; (H) show the different distribution of Kaolinite between reproduced mineral maps derived from May and Oct image; (I) show the different distribution of Kaolinite between Sep and Oct image.....	49
Figure 3.20 (A) show the different distribution of Alunite & Kaolinite between reproduced mineral maps derived from May and Sep image; (B) show the different distribution of Alunite & Kaolinite between reproduced mineral maps derived from May and Oct image; (C) show the different distribution of Alunite & Kaolinite between reproduced mineral maps derived from Sep and Oct image; (D) show the different distribution of Hydrated silica between reproduced mineral maps derived from May and Sep image; (E) show the different distribution of Hydrated silica between reproduced mineral maps derived from May and Oct image; (F) show the different distribution of Hydrated silica between reproduced mineral maps derived from Sep and Oct image; (G) show the different distribution of Montmorillonite between reproduced mineral maps derived from May and Sep image; (H) show the different distribution of Montmorillonite between reproduced mineral maps derived from May and Oct image; (I) show the different distribution of Montmorillonite between reproduced mineral maps derived from Sep and Oct image.....	50
Figure 3.21 (A), (C), and (E) shows the comparison between the ground truth and the classification results created with the universal library through May, Sep, and Oct image respectively; (B), (D), and (F) presents	

the comparison between the ground truth and the classification results created with the customized library through May, Sep, and Oct image respectively. In the X-axis, 0 to 1 represents unclassified, 0 to 1 represents unclassified; 1 to 2 represents Alunite; 2 to 3 represents Buddingtonite; 3 to 4 represents Kaolinite; 4 to 5 represents Alunite & Kaolinite; 5 to 6 represents Hydrated silica; 6 to 7 represents Montmorillonite..... 55

Figure 3.22 Comparison between reproducibility and producer accuracy of Sep image. 56

Figure 3.23 Comparison between reproducibility and producer accuracy of May image..... 56

Figure 3.24 Comparison between reproducibility and producer accuracy of Oct image..... 57

LIST OF TABLES

Table 2.1 Attribute of datasets.....	13
Table 3.1 Linear Spectral correlation of extracted endmembers	31
Table 3.2 Linear Spectral correlation across extracted libraries and the universal library	31
Table 3.3 Confusion matrix of the comparison between May image and Sep image	34
Table 3.4 Confusion matrix of the comparison between May image and Oct image.....	34
Table 3.5 Confusion matrix of the comparison between Sep image and Oct image.....	35
Table 3.6 Comparison of classification results between Sep-Oct image and Oct-Sep image.....	39
Table 3.7 Comparison of classification results between May-Oct image and Oct-May image.....	40
Table 3.8 Comparison of classification results between Sep-Oct image and Oct-Sep image.....	40
Table 3.9 Confusion matrix of the comparison between May image and Sep image	46
Table 3.10 Confusion matrix of the comparison between May image and Oct image.....	46
Table 3.11 Confusion matrix of the comparison between Sep image and Oct image.....	47
Table 3.12 Confusion matrix of the comparison between the ground truth and May image.....	52
Table 3.13 Confusion matrix of the comparison between the ground truth and Sep image.....	53
Table 3.14 Confusion matrix of the comparison between the ground truth and Oct image	54

1. INTRODUCTION

1.1. Background

Identification or classification of minerals using reflectance spectroscopic techniques depends on the wavelength position and depth of their diagnostic absorption features. The electromagnetic wave is absorbed or reflected by different materials in various wavelength, of which the wavelength range 0.4-2.5 μm is commonly used for detection of minerals or rocks because of the concentration of their spectral signatures in this region (Bakker et al., 2013). For example, the presence or absence of water and hydroxyl, carbonate and sulphate make minerals identifiable in shortwave infrared (SWIR) wavelength range due to diagnostic absorptions in 1.4-2.5 μm range (Hunt, 1977). Water molecules show absorption features at 1.4 μm and 1.9 μm , the hydroxyls attached to the metal ions of Mg and Al give absorption features in 2.2-2.3 μm (Duke, 1994), while carbonates have diagnostic absorptions in 2.5-2.55 μm and 2.3-2.35 μm ranges (Van der Meer, 1995). Moreover, the depth of absorption features is normally associated with the relative presenting quantity of corresponding material (van der Meer et al., 2012).

The product of hyperspectral image analysis in geologic remote sensing is a mineral map, of which pixels are assigned to different mineral classes and this processing is known as classification (Bakx et al., 2013). To derive a mineral map, many spectral analysis techniques have been developed for classifying hyperspectral data. According to Asadzadeh & de Souza Filho (2016), there are two main categories named as 'per pixel', or hard classifiers, and 'sub-pixel' or soft classifiers. Hard classifiers compare reference spectra to image spectra one by one and then label each pixel to a class. However, for 'sub-pixel' or soft classifiers, each pixel is acceptable to have multiple labels. Classification methods such as spectral angle mapper (SAM), support vector machine (SVM), spectral feature fitting (SFF), Euclidean distance (ED) belong to the hard classification group. The soft classifiers include linear spectral unmixing (LSU), mixture tuned matched filtering (MTMF), iterative spectral mixture analysis (ISMA). (van der Meer et al., 2012; Asadzadeh & de Souza Filho, 2016).

However, the hyperspectral mineral map is classified by classification methods and the classification relies on the use of spectra of identified pixels within the image as training data. Thus, errors can be jointly made by these either the classification process wrongly classifying a pixel or the training data containing wrong information. Such errors will have a huge impact on the analysis of a user and the reputation of the producer of the final image products (Foody, 2004). Therefore, it is important to validate the classification results for the reduction of errors and then improve the quality of the created maps.

Approximately 1975 is considered to be the historical beginning for accuracy assessment of multispectral remote sensing data. The rapid growth of the number of analysis results derived from remote sensing data acquired by Landsat-1 resulted in researchers beginning to consider and evaluate the quality of their obtained results (Congalton & Green, 1999a). The first criteria and approaches for mapping accuracy assessment were proposed by Hord and Brooner (1976), Van Genderen and Lock (1977), and Ginevan (1979). During the 1980s, Rosenfeld (1982) and Aronoff (1985) performed in-depth-study of the methods and strategies for the validation of multispectral mapping. After the development of decades, the dominant and most common used validation approach for spectral classification results is the confusion matrix (also known as error matrix) (Congalton, 1991; Congalton & Green, 1999a). For the information about confusion matrix, see *Assessing the Accuracy of Remotely Sensed Data* by Congalton & Green (1999b).

1.2. Problem Statement

Nowadays, there are two strategies used for the collection of reference data for the validation of products created from spectroscopic techniques, which are the use of data in-situ measured or assuming a map with higher accuracy as the reference data. (Bakx et al., 2013). However, for both of these two strategies, a problem is observed that they have the indispensability of ancillary information (van der Meer et al., 2012). Moreover, for the use of ground truth data as reference data, only part of a classification result will be directly compared with the reference data since it is impractical to sample for each pixel of the classification results in the field (Congalton & Green, 1999c).

Furthermore, researchers are using various methods for the accuracy assessment of results derived from hyperspectral datasets. For instance, Boubanga-tombet et al. (2018) and Graham et al. (2018) did not report validation results. Pan et al. (2019) presented a ratio that calculated based on the field measurement for the overall accuracy of the classification results but no details about this ratio were shown. Bedini (2009) used a confusion matrix to compare the hyperspectral classification result with ground truth data. Mielke et al. (2016) proposed that the RMSE can be used to assess the accuracy of the abundant image. Kayet et al. (2018) also compare the classification result and surface truth data, but the accuracy ratio in this work is obtained by the analysis method root mean square error (RMSE). However, as opposed to the mature validation framework of the multispectral image, a standardized accuracy assessment method is still lacking in hyperspectral mineral mapping. Therefore, this research aims to fill these niches by the investigation of reproducibility and/or consistency of mineral maps derived from multitemporal hyperspectral scenes.

1.3. Main-assumption

With no standardized validation strategy for hyperspectral classification up to now and to fill the aforesaid niche, that the existing accuracy assessment indispensably depends on the ground truth data or other ancillary independent information. An assumption that estimate the reproducibility and/or consistency of the hyperspectral classification method using multitemporal hyperspectral images is proposed. Theoretically, mineral distribution on a very location should barely change over a short time. Thus, mineral mapping results created by multi-temporal hyperspectral images over the same location is supposed to present a high consistency between each other. In other words, classification results that are derived from multi-temporal hyperspectral images over the same area should be reproducible or consistently created by the same classifier.

1.4. Objectives and research questions

1.4.1. General objective

The general objective of this research is to evaluate the reproducibility and accuracy of hyperspectral mineral maps derived from multitemporal hyperspectral AVIRIS images using the SAM method.

1.4.2. Specific objectives

1. To produce mineral maps from multitemporal hyperspectral image scenes using the same mapping technique.
2. To compare hyperspectral classification results with each other for the evaluation of consistency and/or reproducibility pixel by pixel.
3. To investigate which factors are responsible for differences between mineral maps derived from multitemporal hyperspectral images acquired over the same area.
4. To assess the accuracy of mineral maps created in this research by comparing with ground truth data.
5. To evaluate the correlation and/or association between the reproducibility and accuracy.

1.4.3. Research questions

1. What are the criteria for selecting suitable multitemporal hyperspectral image scenes used in this research?
2. Which classification method should be used?
3. How to compare or/and measure the mineral maps derived from multitemporal hyperspectral images from the same area be compared?
4. How will the reproducibility or robustness amongst classification results derived from multitemporal hyperspectral images be measured and/or defined?
5. Is the difference amongst different mineral maps related to the different acquisition time of the hyperspectral images that those mineral maps were derived from?
6. Will the vegetation cover in the study area affect the reproducibility of hyperspectral classification?
7. Is there any other factor that may disturb the reproducibility of hyperspectral classification and what is it?
8. Which method should be used to assess the accuracy of mineral maps produced in this research?
9. How to verify the relationship between reproducibility and/or robustness amongst classification results and the accuracy of corresponding classification results produced in this research?

1.5. Thesis structure

This thesis has been structured into 5 chapters. Chapter 1, Introduction expounds background, problems, hypothesis, objectives and questions in this research. Chapter 2, Data and Methodology summarized data (hyperspectral data and reference data) and methods used in this research. These methods were used for pre-processing, endmember extraction, mineral mapping, validation, results of the comparison and other ancillary analyses. Chapter 3, Result presents the outcomes obtained from the processing through methods mentioned in chapter 2. Chapter 4, Discussion talked about the results derived from analysis and describes the decision basis for subsequent analysis. Chapter 5, Conclusion and Recommendation

2. DATA AND METHODOLOGY

In this research, shortwave infrared data from three hyperspectral scenes that were acquired from Cuprite, Nevada, USA were used to produce mineral maps. The Cuprite Mineral Map (shown in Figure 2.1) was used as a reference. The methodology is divided into two stages: The first is the pre-processing of the airborne hyperspectral data, in which it contains atmospheric correction, data resize, geocoding of the reference data and other pre-processing steps. The second stage is the processing part which includes endmember extraction, mineral maps production, and analysis of robustness and/or consistency amongst those mineral maps created in this research (flowcharts in Appendix I). If not particularly claiming, then methods used in this research were performed in software ENVI 5.5 (Harris Geospatial Solutions, 2018).

2.1. Data

2.1.1. Study area

The study area of this research is the Cuprite district (Figure 2.1) located in Southwest of Nevada, USA. The area is suitable for this research for the following reasons. First, it hosts different hydrothermal alteration zones containing minerals which can be identified by spectroscopic methods. Second, it has been used as a test site by NASA-JPL in many studies for sensor calibration and spectroscopic studies (van der Meer et al., 2012). Thus, image data acquired at different time over the same location are available in this area. Third, it contains abundant mineral resources with extensive well-studied mineral mapping researches and it has a wide variety of rock types exposed with sparse vegetation cover.

Cuprite mining district consists of two lithological units namely Tertiary volcanic and volcanoclastic rocks of mainly rhyolitic ash-flow tuffs with some air-fall tuff (Kruse & Boardman, 1990). Hydrothermal alteration has extensively modified the volcanic rocks to three altered zones. Such zones include argillaceous alteration zone, silicified alteration zone and the opal alteration zone (Wei et al., 2017). The mineralogy in the silicified zone is mainly quartz with minor calcite, alunite and kaolinite. The argillic zone consists of kaolinite derived from plagioclase, while opal and montmorillonite were derived from volcanic glass. The most intensely altered zone is siliceous rocks while argillized rocks are least intensely altered. The relict textures of the rocks are well preserved in all alteration zones (Ashley & Abrams, 1980).

Swayze et al. (2014) directionally named two hydrothermal alteration regions which are abundantly mineralized in the Cuprite district as the eastern centre and the western centre (shown in Figure 2.1). For the reduction of uncertainty, the study area in this research must be contained by a single scene from each of the hyperspectral datasets used and these scenes should have a relatively high spatial resolution of the hyperspectral datasets, necessary for clear understanding and distinguish of the mineral distribution. However, based on the available AVIRIS datasets, no scenes that cover both of these two hydrothermal alteration centres match the criteria mentioned above. In the other world, only one alteration centre can be focused on for analysis.

In this research, the eastern centre was selected as the study area because the selection of the western centre as the study area may complicate the analysis in this research for the following reasons. Initially, the composition of the silicified alteration region in the eastern centre shows a more concentrating distribution with bigger size than its distribution in the western centre. Besides that, four different kinds of white micas that located in the western centre will complicate the processing of endmember extraction, classification, and measurement of reproducibility in this research. Third, the spectral absorption features of *Dickite* which mineralized in the western centre with large scale is similar to the spectral curve of

Kaolinite. Thus, the classification may create confusing results for these two minerals in the western centre (Swayze et al., 2014).

2.1.2. Remote sensing data

The remote sensing datasets were used to create mineral maps for the investigation of reproducibility and/or the consistency amongst classification results derived from different classifiers in this research. They are provided by NASA (National Aeronautics and Space Administration) and collected by the AVIRIS-classic (the airborne visible/infrared imaging spectrometer) sensor that records electromagnetic radiance signal which reflected from the target in 224 continuous narrow bands. This dataset consists of three geometrically and radiometrically corrected airborne multi-temporal hyperspectral scenes (details in table 2.1) and they were acquired over the same area but have slight geographically shift with each other.

The AVIRIS images used in this research were selected from all hyperspectral images provided by NASA over the study area of this research based on the following criteria. Initially, the study area in this research must be contained by a single scene from each of the hyperspectral datasets used. This is because the uncertainty will be enhanced across scenes within the study area. This uncertainty may be a result of different illumination magnitude, solar elevation, and shadow amongst different scenes as a result of the different acquisition time of these scenes. Secondly, to clearly understand and classify the mineral distribution in the study area, a relatively high spatial resolution of the hyperspectral datasets is necessary for this research. Thirdly, each of the multitemporal hyperspectral scenes should have the same or at least similar spatial resolution to reduce the uncertainty caused by the resampling of the comparison amongst classification results derived from these scenes. Fourthly, the acquisition time of multitemporal hyperspectral images used in this research should belong to the different season for the estimation of the potential influence that is affected by vegetations.

Eventually, three images that match the four criteria mentioned above were selected and used in this research. They were acquired by the AVIRIS sensor over the same place and at a different time. The May image was acquired at 19:02 (UTC) on the 2nd May 2006, the September image was acquired at 18:39 (UTC) on the 20th Sep 2008, and Oct image acquired at 10:22 (UTC) on the 14th Oct 2010. The spatial resolution of May image and Sep image is 3.3 m while the Oct image has the pixel size as 3.2 m. The Eastern centre, the study area in this research, is completely covered by all three images.

Table 2.1 Attribute of datasets

Airborne Hyperspectral Image				Auxiliary	
Data Type	Radiance at Sensor			Data Type	Mineral Map
Name of Sensor	AVIRIS-Classic			Name of Mineral Map	Cuprite,Nevada_1995_ AVIRIS_Data_Tetracor der_Mineral_Map Clays, Micas, Sulphates, Carbs. (+legend)
Projection	UTM 11				
Datum	WGS-84				
Status	L1-B				
Flight Name	Acquisition Time	Pixel Size	Spectral Resolution	Projection	UTM 11
f060502t01p00r05	02 May 2006 UTC:19:02	3.3m	10nm	Datum	NAD27
f080920t01p00r04	20 Sep 2008 UTC:18:39	3.3m	10nm	Time	1995
f101014t01p00r04	14 Oct 2010 UTC:20:22	3.2m	10nm	Producer	Clark & Swayze

EVALUATING REPRODUCIBILITY AND ACCURACY OF HYPERSPECTRAL MINERAL MAPS USING MULTI-TEMPORAL AVIRIS IMAGES OF CUPRITE, NEVADA, USA

The multitemporal AVIRIS images used in this research were offered by NASA in L1-B status. Thus, all of them has already been both calibrated and ortho-corrected by NASA with ancillary information. Therefore, multitemporal AVIRIS images used in this research are radiance-at-sensor data. And the ortho-correction was done through a complete 3-dimensional ray tracing model and a set of DEM data in spatial resolution of 30 m. During this ortho-correction, each individual pixel of the multitemporal AVIRIS scenes was traced by the 3-d model for its location and altitude until they match the DEM data. Therefore, there is no more ortho-correction and calibration were processed in this research according to the AVIRIS scenes used in this research had already been ortho-corrected and calibrated by NASA which is an institution that produced these images (Boardman, 2007).

2.1.3. Ground truth data

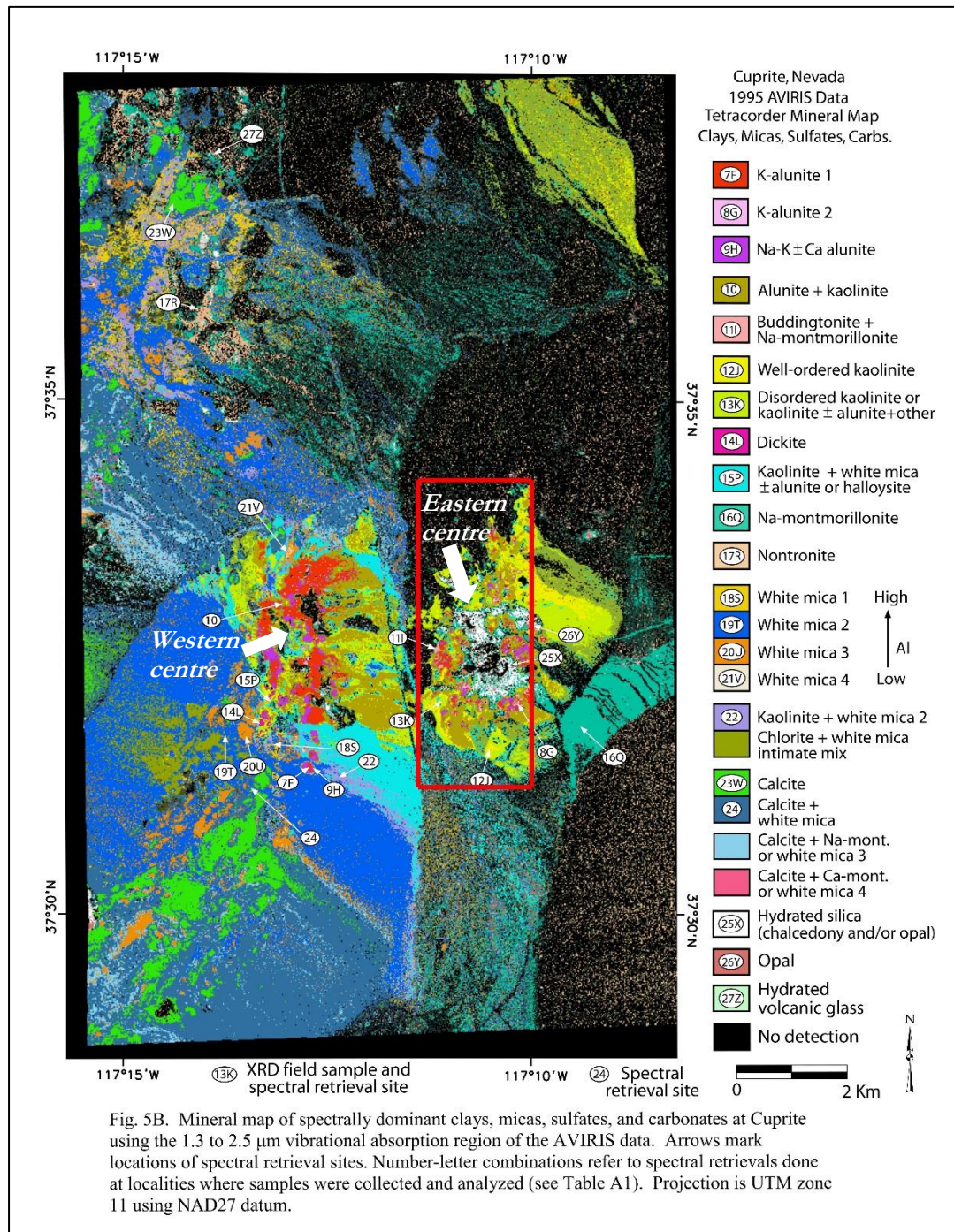


Figure 2.1 Cuprite, Nevada 1995 AVIRIS Data Mineral Map Clays, Micas, Sulphates, Carbs (Source: Swayze et al., 2014) The red box shows the study area of this MSc research

The second dataset is the Cuprite Mineral Map (shown in Figure 2.1) which mapped dominant minerals such as clays, micas, sulphates, and Carbonates, of 1.3-2.5 μm wavelength range (Swayze et al., 2014). This map was generated by Swayze et al. (2014) and it was retrieved from AVIRIS data. The Cuprite Mineral Map was validated by the authors using in-situ measurements and other ancillary information. A published and well-validated mineral map that also derived from the AVIRIS scenes was considered as the ground truth data for this research. Since there is no in-situ measurement in this research. Thus, the Cuprite Mineral Map was used for the accuracy assessment of mineral maps created based on the multi-temporal hyperspectral images in this research. The Cuprite Mineral Map was re-geocoded in this research and is presented in Figure 2.1 below. The geo-coding allows it to be linked with the multitemporal hyperspectral images used in this research as an independent ground truth material.

2.2. Pre-processing

2.2.1. Atmospheric correction

The AVIRIS data used in this research were provided by NASA-JPL (2010) and they have already been pre-processed to remove the adverse image characteristics caused by geometric and radiometric effects which are generated during the data acquisition. Therefore, the first pre-processing step in this research was an atmospheric correction to minimize redundant effects such as atmospheric path radiance which is the radiant energy scattered by the atmosphere and the adjacency effect which is reflected from the surface surrounding the target material (Kale et al., 2017).

To achieve the objectives of this research, it was necessary and important to select an appropriate atmospheric correction method. The algorithms used for atmospheric correction can be divided into two categories, which are model-based and empirical-based methods (Ben-Dor, Kindel, & Goetz, 2004). Selection of the optimal atmospheric correction method depends on the purpose, ancillary information, and scene condition in the research. Normally, a rigorous model-based algorithm (such as FLAASH) is suitable for the use of the spectral library to classify surface target (Harris Geospatial Solution Inc., 2018a) as the classification methods will be used in this research. Thus, a literature review is done to select a suitable model-based atmospheric correction algorithm. Kruse (2004) compared several model-based atmospheric correction algorithms such as FLAASH, ACORN, and ATREM and he proposed the method FLAASH is the most flexible method for the correction of generating an accurate surface reflectance image from hyperspectral or multispectral radiance data. Rani et al. (2017) concluded that the model FLAASH is a rigorous tool which has the ability to correctly compensate for the effect of atmospheric scattering and absorption. Moreover, it is better than the other model-based atmospheric correction methods in the condition of enough ancillary information. Therefore, the model FLAASH was selected in this research.

The model FLAASH (fast line-of-sight atmospheric analysis of hypercubes) which is developed by Spectral Centre and Research System, Inc. (Perkins et al., 2005) is an atmospheric correction code used to remove the interference of atmospheric scattering and the adjacency effect. The radiation transfer code of FLAASH is based on model MODTRAN4 whereas the standard MODTRAN model is used for the atmosphere and aerosol types code of FLAASH (Berk et al., 1998; Perkins et al., 2005). The result of FLAASH includes physics-based surface reflectance image, water vapor conditions, artefacts suppression, and cloud classification. FLAASH is suitable for the spectral data in the wavelength range from 0.4 μm to 2.5 μm (Rani et al., 2017), therefore the target wavelength range (2.0-2.5 μm) of this study is covered. A wavelength range from 2.0-2.5 μm was selected because this region is useful for the investigation of the hydrothermal mineralized system (Amera, 2007) which is the dominant mineralizing system of the study area. Software ENVI is used to run the model FLAASH in this research and it has already built-in the latest version of the FLAASH model.

The use of FLAASH model requires ancillary information and some of them are derived from the certain wavelength of the input data. The first portion of the auxiliaries is the gain values which is used to scale

the data. It is because the data provider of NASA/JPL used an array of gain values to convert the data type into an integer for economizing of hard disk space (Jin, 2018). With these gain values, FLAASH converts the input 16-bits integer data into radiance in the units of $\mu\text{W}/\text{cm}^2\cdot\text{sr}\cdot\text{nm}$, which will match the requirement of FLAASH. Subsequently, some auxiliary information that was recorded during the data acquisition is required, such as acquisition time, the elevation of target ground and the altitude of the sensor, pixel size, and geographic position (Perkins et al., 2005). Furthermore, to perform the water vapor retrieval, the spectral resolution of the image must better than 15nm and the certain image contains bands that cover wavelength range 1050-1210nm while the range 870-1020nm and/or 770-870nm are considered as a substitution when the band around 1050-1210nm is absent (Harris Geospatial Solution Inc., 2018a). FLAASH employs an empirical ratio-based algorithm to retrieve the aerosol conditions, in which the boundary layer aerosol optical depth will be divided by effective layer thickness (Perkins et al., 2005).

Figure 2.2 Settings used for atmospheric correction of May image of model FLAASH in software ENVI

2.2.2. Data resize

Following the atmospheric correction, hyperspectral images used in this study were spatially and spectrally subsetted to match the requirement of this research. It is because some necessary ancillary information for the atmospheric correction of the FLAASH method is recorded in certain bands which are outside of the wavelength range for the subsequent research in this research. Therefore, the atmospheric influence of the multitemporal hyperspectral images used in this research cannot be corrected without those bands but the spectral analysis and classification will be complicated without excluding those bands. Thus, the spectral subsetting must follow the atmospheric correction.

For the spatial subset, two criteria were built and the first one is the study area after the spatial subset should cover regions with abundant mineral types for the universal representation of this investigation. The second criterion is the study area should avoid all the dark boundaries in every scene. The reason for

that is because the pixel values of the dark boundary will bother the statistics results that will follow. Based on these two criteria, a region of interest file was built to generate the study area in the Cuprite mineralize district (shown in a red pane of Figure 2.1).

Spectral subsetting was conducted in two steps in this research. It is a tool for the excluding of unnecessary wavelength bands of the dataset used in research (Harris Geospatial Solution Inc., 2018b). Initially, for the purpose of focusing on the targeting minerals in this study area, spectral subsetting was first performed to focus on a wavelength range 2.0-2.5 μm . It is because this range is useful for the investigation of the hydrothermal mineralized system (Amera, 2007) which is the dominant mineralizing system of the study area. Secondly, based on the Cuprite Mineral Map produced by Swayze et al (2014), the alteration minerals in this area are identified as *alunite*, *buddingtonite*, *kaolinite*, *alunite & kaolinite*, *hydrated silica*, and *montmorillonite*. None of these minerals has the first diagnostic spectral features out of the wavelength range 2120 nm to 2250 nm. And, the shoulders of spectral signatures of this research's targeting mineral are concentrating at the wavelength range 2048-2120 nm and 2250-2350 nm. Furthermore, this result was supported by the frequency of the wavelength range of the first absorption feature (shown in Figure 3.5) generated by the wavelength mapping through software HypPy (Bakker, 2018). Thus, during wavelength mapping, the wavelength range of the hyperspectral images used was further subsetting to 2048 nm to 2308 nm in this research. Since the other bands that exclude that range will not be used for classification in this research and the that many bands will both complicate and slow the speed of analysis.

2.2.3. Geocoding

The Cuprite Mineral Map (Swayze et al., 2014) was used as independent ground truth in this research to assess the accuracy of the classification results. However, this map was georeferenced by latitude and longitude with NAD 27 but the multitemporal hyperspectral images used for classification were projected to the UTM 11 with the datum of WGS-84. Therefore, the Cuprite Mineral Map was projected to WGS-84 datum by the software Global Mapper (Blue Marble Geographics, n.d.).

2.2.4. Region of interest (ROI)

The ROI is a built-in tool of ENVI software, which is used to select pixels by particular characteristics, geometry, or drawn manually in a raster image. Afterwards, these selected pixels can be classified, be calculated for statistics, or be used to overlapped other images that have the same pixel size with them (Harris Geospatial Solution Inc., 2018c).

In this research, the tool ROI was used for three purposes. First, it was used to select pixels that represent each kind of mineral in the Cuprite Mineral Map created by Swayze et al. (2014) through the unique value of each mineral type in the green band of this RGB file. Subsequently, those ROIs that represents one mineral were classified to generate a reclassified file (see Appendix VI) for accuracy assessment by the confusion matrix. Second, there were several markers in the Cuprite Mineral Map used to label the field sampling position, and these markers were manually selected by drawing, then each of them was replaced with the same class as the pixels surrounding it. Third, the tool ROI was used to identify vegetation conditions in the NDVI results by the threshold claimed by Weier & Herring (2000).

2.3. Processing

2.3.1. Wavelength mapping

The wavelength mapping method was performed through software HypPy (Bakker, 2018) to display the distribution and depth of the deepest spectral absorption features in each pixel of the study area. This processing depends on the surface reflectance of the images.

The procedure of wavelength mapping consists of two steps. In the first step, the tool Wavelength of Minimum that consists of two techniques was used to dominate the wavelength of the deepest absorption

pixel by pixel and measure the depth of those absorption features. The first technique is continuum removal, which was performed by divide the pixel spectrum with a convex hull to highlight the deepest absorption features (Van Ruitenbeek et al., 2014). Afterwards, another interpolation technique was conducted to calculate the deepest wavelength position of the continuum removed spectrum. The interpolation is necessary because the deepest absorption feature may be located between two bands. Therefore, a parabola was fitted to the absorption curve by three consecutive bands which is the band with the smallest value and two bands on two sides of it. Thus, the corresponding wavelength to the smallest value of this polynomial is the wavelength of the deepest absorption feature (Van Ruitenbeek et al., 2014). These two techniques were performed by the tool Wavelength of Minimum pixel by pixel and to generate a map that displays the wavelength of the smallest value of the local spectrum (Bakker, 2012). For this research, wavelength mapping of only the first feature was measured because the minerals in the study area are *alunite*, *buddingtonite*, *kaolinite*, *alunite & kaolinite*, *hydrated silica*, and *montmorillonite*, and most of them can be easily separated by just the first absorption feature. Eventually, a map with two bands was produced. One band records the wavelength of the deepest absorption feature for each pixel and another band records the depth of the absorption features relative to the continuum hull (Van Ruitenbeek et al., 2014).

Following the map produced by the minimum wavelength, a new image was generated to combine and visualize two kinds of information produced by the first step. In the second step, wavelength mapping transforms the digital information to a colourful map with the HSV colour table. Of which the hue (H) of a certain pixel is dominated by its wavelength position of the deepest reflectance value and the colour value (V) of a pixel is controlled by the depth of its deepest absorption feature. Afterwards, a wavelength map is created with corresponding colour legend through setting the saturation (S) as 1 for every pixel (Van Ruitenbeek et al., 2014). This map was used to give indices for the interpolation of surface mineral and display distribution of the deepest absorption features for a different type of minerals.

Moreover, a histogram was also generated based on the minimum wavelength. This histogram summarized the frequency of the minimum wavelength for each pixel of the map produced by the minimum wavelength (Bakker, 2012). This histogram was used to support the second spectral subsetting for the multitemporal hyperspectral images in this research.

2.3.2. Spatial-spectral endmember extraction (SSEE)

The spatial-spectral endmember extraction (SSEE) method was applied on scenes modified and corrected by aforesaid pre-processing methods then the collected endmembers were compared with the spectral library proposed by the United States Geological Survey (USGS) (Rogge et al., 2007). The SSEE was selected to extract endmembers in this research because the spectral contrast will affect the ability for discrimination of pixels which carried relatively unique spectrum base on their spectral features, and it will be hard to discriminate potential endmembers which got low spectral differences. Therefore, the SSEE works on subsets which are square, have equal size, and not overlapping of a scene, thus a smaller spectra assemblage will help to classify pixels with relatively low spectral contrast (Rogge et al., 2012). Because the spectral contrast is a relative conception which hinges on the combination of spectra. In other word, for the spectrum that got low spectral contrast when compared to the whole scene may have high spectral contrast when it compared with a smaller group of spectra which surround it.

Therefore, within the square-subsetting region, the eigenvectors which clarify the major spectral characteristics of the corresponding region will be efficiently calculated and collected. Subsequently, the spectrum of each pixel in a subset region will be projected to the compiled local eigenvector, then those spectra that reach the external of the vector will be recorded as candidate endmembers (Rogge et al., 2012). Afterwards, the spatial constraining will be applied by the SSEE to average the similar endmembers which are near to each other and output those similar endmembers that are spatial independent (Rogge et al., 2007).

Eventually, endmembers that been collected with SSEE will be compared with the spectral library proposed by the USGS to label endmembers with certain minerals and the slight shifts may be caused by the error caused by calibration and/or the purity of target will be considered in this procedure. Then each endmember spectral library from each image was used to create a universal spectral library by averaging the endmember of each mineral.

2.3.3. Spectral correlation

The correlation coefficient was used to calculate the similarity among spectral endmembers of the same minerals that were collected from different images and it was calculated through the software Excel. The correlation coefficient used in this research is the linear correlation coefficient which was calculated to measure the degree of association between two variables (Asuero et al., 2006), which in this study means spectra. This coefficient is defined as the covariance of two random variables divided by the standard derivation of these two variables, therefore the drawback of covariance, which is the dependence of the measurement scale is fixed (Asuero et al., 2006). The formula of correlation is expressed as follows

$$r_{xy} = \frac{\sum(x_i - \bar{x})(y_i - \bar{y})}{\sqrt{\sum(x_i - \bar{x})^2 \sum(y_i - \bar{y})^2}} \quad i=(1,2,\dots,n) \quad (1)$$

In the above formula, \mathbf{x} and \mathbf{y} represent two random variables and r_{xy} is the correlation coefficient of these two variables. Eventually, for the result of r_{xy} ($-1 \leq r \leq 1$) will index the association between variables. Briefly, the positive association is progressively increase follow the increasing of the digital of r . In the other word, two random variables are totally positive correlated when $r = 1$, totally uncorrelated when $r=0$, and totally negative correlated when $r = -1$ (Asuero et al., 2006; Gogtay & Thatte, 2017).

In this research, the spectral correlation was used for comparing endmembers of every mineral in each of the four endmember libraries to avoid the differences of themselves unnecessarily influencing the robustness or reproducibility of classification results. Three of them are extracted libraries while one of them is the universal library. subsequently, the three extracted endmember libraries were compared with each other and the universal library was compared with each of the extracted libraries.

2.3.4. Spectral angle mapper (SAM)

The algorithm SAM was used in this research for the mapping of the mineral distribution on the ground. SAM is a method that allows fast classification by assigning image spectra to the corresponding reference spectrum. Reference spectrum can be spectra that measured from the field or in the laboratory or extracted from the image itself, based on the similarity of them (Kruse et al., 1993). The algorithm SAM measures the similarity between the reference spectrum and test spectra by project them to an n-dimensional space (n equal to the number of bands of those spectra) as vectors, then calculate the angle between them (Kruse et al., 1993). Afterwards, the user will manually set a unique threshold or a set of various thresholds for different classes of reference spectra and the test spectra with angle degree lower than this threshold will be assigned to the class of corresponding reference spectrum.

The SAM method was selected in this research to generate mineral maps for the investigation of classification reproducibility. Firstly, SAM was picked because it is widely used in the community of geological remote sensing and easily available. Bertels et al. (2005) indicated that the most popular category of the hyperspectral classification method is the similarity measurement and SAM is a commonly used method in this category. Rajendran & Nasir (2018) also claimed that SAM is one of the most often used methods for hyperspectral mineral mapping. Moreover, the standard SAM algorithm is a built-in tool of the most commonly used image processing applications (Bertels et al., 2005). Thus, SAM is an easily available algorithm for other researchers. On the other hand, it is also because SAM has already been proven as an efficient mineral mapping method. Asadzadeh & de Souza Filho (2016) claimed results of SAM shows better performance of the detecting for the boundaries of the target than the method Euclidean distance (ED) which is also in the category of similarity measurement. And Rahman (2016)

concluded that SAM processing is based on the comparison of spectral signature between the targets and reference spectra and therefore it will generate good results.

In this research, several mineral maps were produced with different sets of thresholds and different endmember libraries. Firstly, hyperspectral images were classified twice using two sets of thresholds (see Appendix II). One set of these thresholds is the various thresholds set by “trial and error” that changed from mineral to mineral. This set of thresholds were set based on the May image with the wavelength maps produced in this research and the Cuprite Mineral Map produced by Swayze et al. (2014) as references. Another set of thresholds for each mineral of each image were automatically set as a unique value “0.1” by ENVI software. Secondly, hyperspectral images were created with different endmember libraries and each hyperspectral image acquired at different time was classified with extracted endmember library and the universal endmember library respectively. These six mineral maps were compared with each other to investigate the comprehensive reproducibility and/or consistency of the SAM classification method. Afterwards, based on these six mineral maps, and the six different minerals, 36 solo mineral maps (see Appendix V) were created for the investigation of consistency and/or reproducibility mineral by mineral.

2.3.5. Image-to-image registration

Method image-to-image registration was performed through software ENVI and it is robust as well as accurate for the alignment of multi-temporal images (Jin, 2018). It is used to spatially fit multi-temporal images over the same area and to align corresponding pixels of those images so they cover with each other as much overlap as possible, with the purpose of improving the accuracy of comparison (Schowengerdt, 2007). This method consists of two parts, the ground control points selection and the image warping.

The procedure of ground control points selection contains three steps: in the initial phase, two images with the same geo-coordinate system were inputted as the basic image and the warped image respectively. Subsequently, ground control points (GCP) were selected on each of these two images as the tie to fit the warped image to the basic image. In other word, a GCP on the basic image is supposed to have the same geographic position as its corresponding GCP on the warped image. However, spatial errors of the GCPs on either image are impossible to totally eliminate, thus sufficient numbers are significant to minimize the influence caused by those spatial errors (Usman, 2018) (e.g. more than 70 GCPs were selected in this research). During the selection of GCPs, a subset window will be automatically generated by the algorithm and its size depends on the parameter set by the user. This patch slips over both of the images to measure the grey value scale within the subset window and try to find conjugate GCPs based on the similarity of the grey degree (Harris Geospatial Solution Inc., 2018d). Based on that, GCPs are selected automatically to avoid the bias derived from the manual GCPs selection.

Afterwards, the RMS error (root mean square error) will be calculated by the GCP self-test function to measure the malposition between a pair of GCPs on both of the images. The unit of the provided RMS error number is meter, it is directly calculated based on the GCPs themselves with the consideration of the spatial resolution of the input images (Barazzetti et al., 2016). And the GCP with high RMSE will be manually deleted. On the other hand, for some spots that assuredly in the same location (such as the road cross or the edge of hills) of two images, the manual GCP addition is also used to ensure both of the accuracy and number of GCPs. Eventually, GCPs with RMS error (e.g. the RMSE of GCPs in this research is 0.581 m and 0.771 m respectively) that lower than the pixel size of the images were used to align two images.

Following the second step, the warped image will be aligned to the basic image through the GCPs and a resampling processing (Harris Geospatial Solution Inc., 2018d). In this study, the hyperspectral image acquired on the 2nd May 2006 was chosen as the basic image, and the other two images were spatially fit to it. Afterwards, some slightly shift caused by the different number of pixels between the warped images and the basic image will be fixed by spatial resize.

Nevertheless, based on the conclusion of Zhou et al., (2003), any resampling models lose spectral information more or less and mix the spectra within pixels. Thus, those lost information and mixed spectra resulted in the last phase, which is the resampling, of the image-to-image registration will enhance the uncertainty for the subsequent analyses. Therefore, the input hyperspectral images will be classified first then those classification results will be rectified to fit the same basic image. Therefore, the spectra of each pixel will not be mixed by image registration and the differences across classifiers and/or multi-temple hyperspectral images can be pixel-based analysed.

2.3.6. Confusion matrix

The confusion matrix is a widely used method for comparing the classification result and the reference data to validate the correctness of the classification result (Congalton, 1991; Tobergte & Curtis, 2013). Two ratios, error of commission which means there are certain materials in the reference data but not in the classification result and error of omission which means there are certain materials in the classification result but not in the reference data are measured (Congalton, 1991; Pontius & Millones, 2011). Besides these, the user accuracy and the producer accuracy are the other two important information provided in the confusion matrix. The user accuracy is the probability that a certain class in the reference image is correctly labelled as the same class in the test image. While the producer accuracy is the probability that pixels in the test image can be actually identified as the class of reference image (Congalton, 1991; Bakx et al., 2013).

Because of the integrated information summarized in the confusion matrix, it is also very convenient for applying several analysis methods to calculate these data for accuracy assessment (Foody, 2008). The most common one of these methods is the overall accuracy which is the number of all of the correctly classified pixels divided by the total of the pixels assessed (Bakx et al., 2013).

Confusion matrix was used to compare the similarity or reproducibility of three pairs of SAM classification results derived from May image and Sep image, May image and Oct image, as well as Sep image and Oct image respectively through software ENVI. The calculation of the confusion matrix of software ENVI will calculate every pixel in the input images. On the other hand, every pixel of the six comprehensive mineral maps derived from three multitemporal hyperspectral images with the extracted and universal endmember libraries were also compared with each spatially corresponding pixel of the Cuprite Mineral Map (Swayze et al., 2014) which is the ground truth data in this research to calculate the correctness of these SAM classification results.

2.3.7. Masks

0	1	0	1
1	0	1	1
0	1	0	1
1	1	0	1

(A)

1	0	1	0
0	1	0	0
1	0	1	0
0	0	1	0

(B)

0	2	0	2
2	0	2	2
0	2	0	2
2	2	0	2

(C)

Figure 2.3 (A) shows the original condition of a solo mineral map; (B) presents the values of pixels of the mask file when pixels of (A) excluded by the it with the characteristic as value equal to “zero”; (C) shows the value “one” in each pixel of the original solo mineral maps is changed to the value “two”. It is because each pixel that have value as “zero” in a mask file then the value of its spatially corresponding pixel of the original image can be exchanged through the tool “applying mask”.

Masks are tools used to exclude pixels with particular characteristics (for instance value or position). Once a mask is built in ENVI software based on certain characteristics, pixels contain conforming characteristics will be highlighted by getting the value as one while every other pixel will get the value as zero in the raster file. Then, for the using of mask, with the tool “applying mask”, a mask file can be overlapped on an image has the same size and location with it and the value of that image can be set to exchange values of every pixel that is not highlighted in the mask (Harris Geospatial Solution Inc., 2018e). Masks were used for giving a different value to those maps with only one mineral type produced by the method SAM (shown in the conceptual graph Figure 2.3). Originally, in the solo mineral maps, pixels that identified as mineral carry the value of “one”(shown in Figure 2.3 A). However, for each mineral type there a total of three corresponding mineral maps and each of them derived from one of the three different hyperspectral images. Therefore, the differences amongst those mineral maps are hard to be completely observed based on the same value carried by every classified pixel of three various maps. Thus, pixels of solo mineral maps derived from May image and Sep image were assigned a new value of “two” by the method mask (shown in Figure C).

2.3.8. Change detection (CD)

Change detection is a method used for the detection of differences in the targets at different times (Lu et al., 2009). These three mineral maps were analysed by the built-in tool change detection difference map of ENVI software. This tool allows setting two images as “final state” image and “initial state” image respectively then the value contained by each pixel of the “final state” image will subtract the value of the spatially corresponding pixel of the “initial state” image. Subsequently, some threshold will be manually set to class the values of detected differences. Eventually, the change detection result will be present in a red and blue map, of which red indict positive differences and brighter red pixel means higher value. While blue express negative and darker blue shows an even lower value (Harris Geospatial Solution Inc, 2018f).

For the use of change detection in this research, solo mineral maps whose value was exchanged to two of the identified pixels were set as the “initial state” image (as a conceptual graph shown in Figure 2.4 A) and those solo mineral maps with original value for the identified pixels were set as “final state” image (shown in Figure 2.4 B). The “initial state” image was assumed as the reference image in this research. Then the method change detection used the value contained in each pixel of the “final state” image to subtract the value of corresponding pixels in the “initial state” image. Therefore, for those pixels that were not identified in both of these images, the value of them in the CD image remains zero and for the pixels both identified, the value of CD image is minus one. On the other hand, for those pixels only identified in the “initial state” images were recorded as omission. Similarly, those pixels only identified in the “final state” images were labelled as commission. Eventually, both the spatially and identically information was summarized and directly visualized with this method (shown in Figure 2.4 C).

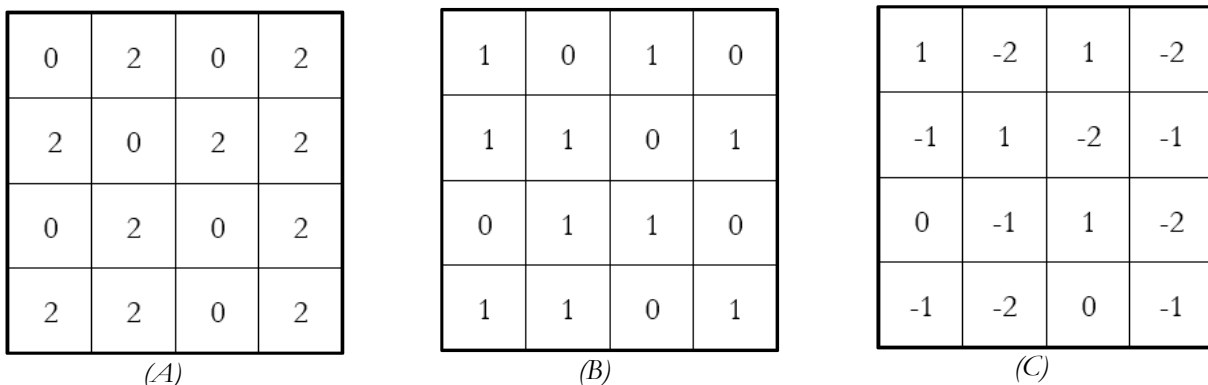


Figure 2.5 (A) shows the distribution of the pixels whose value is “two” of the “initial stat” image; similarly, (B) shows the distribution of the pixels whose value is “one” of the “final stat” image; (C) presents the result when the value of pixels of the “final state” image subtracts the value of their corresponding pixels in the “initial state” image. Meanwhile, the “initial state” image was assumed as the reference data while the “final state” image was assumed as the test data. Therefore, in graph (C), “-2” presents omission, “-1” shows that pixel was classified in both of these two mineral maps, “0” presents that pixel was not identified in both of the solo maps, and “1” indicates that pixel should be labelled as commission.

2.3.9. Similarization

A method named as similarization in this research was designed to investigate the relationship between differences amongst the original radiance datasets and the reproducibility of results derived from those datasets. Initially, three original multitemporal hyperspectral image scenes were paired to three pairs which are May image and Sep image, May image and Oct image, as well as Sep image and Oct image. Subsequently, the change detection tool was used to highlight pixels that only have the same or similar values (± 100 of the reflectance value) in the same location within these three pairs of images. Then those highlighted pixels were selected by the ROI tool. The selection of pixels with similar values based on the comparison between only two images, because more information and pixels will be excluded if the selection was based on the differences for all of the three images. Afterwards, those pixels that are from the same dataset were saved as a new image file then three pairs of new hyperspectral images were created, of which each pixel in an image only has the same or similar values to a pixel that has the same location with it of the other image in this pair.

In this research, these similarized new images were named as May-Sep image, May-Oct image, Sep-May image, Sep-Oct image, Oct-May image, and Oct-Sep image. For the name of a new image, the former part on behalf of an original image that this image is similarized from while the latter half of the name indicates which original scene this new image is similar with. For instance, the May-Sep image means this image was similarized based on the selection of pixels of May image and these pixels have the similar or same value with pixels in the same location with them in Sep image.

2.3.10. Identification similarity

The overall accuracy that used to interpret information summarized by the confusion matrix was defined as the number of all of the correctly classified pixels divided by the total of the pixels assessed (Bakx et al., 2013). But for mineral maps derived from the similarized hyperspectral images, pixels that correctly labelled as unclassified may influence the reliability of the overall accuracy. Since the only pixel that has similar value was selected in former operation and a lot of pixels that show different values were excluded during the processing of similarization. Therefore, to measure the reproducibility of classification results derived from the similarized hyperspectral images, the identification similarity was defined in this research.

The calculation of identification similarity still based on the comparison results of the confusion matrix. However, it was defined in this research as the sum of the number of pixels that identified as mineral divided by the difference of the number of all the pixels minus the number of the pixels that identified as unclassified. Therefore, this calculation can eliminate the influence by the number of unclassified pixels that produced during the similarization processing for the overall accuracy.

Subsequently, these three pairs of images were classified by SAM with the corresponding extracted endmember libraries. Therefore, for any pair of these three hyperspectral images, if the classification results that derived from each of the images in certain pair show similarity of identification between each other. Then, the assumption that the low reproducibility amongst classification results that derived from multitemporal hyperspectral images over the same area is related to the differences amongst those hyperspectral images themselves can be confirmed.

2.3.11. Normalized difference vegetation index (NDVI)

In the past three decades, NDVI (Normalized difference vegetation index) method has been widely used in many remote sensing applications, including the measurement of both green vegetations and dry vegetations in the end-of-season, for the coefficient of the vegetation land covers (Rouse et al., 1973; Bhandari et al., 2012). This algorithm is designed to use the difference between apparent reflectance of the red channel whose wavelength is around $0.66 \mu\text{m}$ and the apparent reflectance of the near-infrared channel whose wavelength is around $0.86 \mu\text{m}$ to be divided by the sum of these two values (Rouse et al., 1973). The equation of NDVI is shown below

$$NDVI=(R_{NIR}-R_{Red})/(R_{NIR}+R_{Red}) \quad (2)$$

In this equation, the R_{NIR} means the reflectance value of the near infrared channel and R_{Red} means the reflectance value of the red channel. The NDVI index will be calculated through this formula and be classified by different threshold (Gandhi et al., 2015). Empirically, very low NDVI coefficient (0.1 and below) presents the ground surface without vegetations, middle NDVI index (0.2-0.3) indicates grassland or barren on the ground, and high value of the NDVI index (0.6-0.8) presents the forest (Weier & Herring, 2000).

Swayze et al. (2014) indicated that only sparse vegetation covering (around 15%) in the study area which is the Cuprite mineralization region, Nevada of this research. However, the change of vegetation following time series might still slightly influence the classification result derived from the hyperspectral image acquired at multiple time. Thus, NDVI the best known (Tobergte & Curtis, 2013) vegetation index method was selected to map the distribution of vegetation based on the multitemporal hyperspectral images, which are the same datasets that used for mineral mapping in this research, of the study area. The NDVI results were identified by the tool ROI built-in software ENVI with the threshold claimed by Weier & Herring (2000). Then these classified results were used to analyse the vegetation cover conditions in the study area and then investigate the potential influence of vegetation to hyperspectral mineral mapping in this research.

2.3.12. Measurement of the reproducibility

There are two kinds of reproducibility that were measured in this research. The first one is the comprehensive reproducibility between the mineral maps with all the six kinds of minerals. As aforesaid, this measurement was done through the method confusion matrix by assuming one mineral map as reference data and another one as the test data. Thus, the overall accuracy calculated together with the confusion matrix can be simulated as the overall reproducibility of the compared classification images. Nevertheless, the results summarized by the confusion matrix are too complicated for the analysis of reproducibility for the single mineral type. Therefore, the second kind of measurement of reproducibility was designed to investigate reproducibility mineral by mineral.

The second measurement was designed based on the statistics in the results of the differences maps created by the method change detection and derived from the solo mineral maps. They present the number of pixels that are detected such as both unidentified, reproduced, commission result, or omission result and the number of all the pixels of these solo mineral maps by change detection. Therefore, the ratio of reproducibility between a pair of solo mineral maps that derived from different AVIRIS images was defined as

$$R=B/(S-U) \quad (3)$$

In this equation, R represents the reproducibility while B means the number of pixels that classified as the same mineral in both of the solo mineral maps classified from different hyperspectral images. S indicates the number of all the pixels in a solo mineral map. Eventually, U represents the number of pixels that unidentified in both of the solo mineral maps classified from two hyperspectral images. Therefore, the influence of the reproducibility by the number of unidentified pixels can be eliminated by this calculation. The reproducibility of mineral n carried out from image X was defined as the

$$(R_{n:x:y}+R_{n:x:z})/2 \quad (4)$$

$R_{n:x:y}$ indicates the reproducibility of mineral n between solo mineral maps derived from image X and image Y while $R_{n:x:z}$ indicates the reproducibility of mineral n between solo mineral maps derived from image X and image Z . This is because the reproducibility measurement was processed based on a

comparison between two mineral maps in this research. Therefore, this calculation can summarize the reproducibility of mineral n carried out from image X with both other two images.

2.3.13. Plot

Several different types of plots were performed by the software Excel as well as software HypPy and used in this research to visualize data extracted from the statistical results. It is a more informative and directive way than only using the digital result derived from the correlation coefficient.

Scatter plot is generated based on the projection of n times sampling of two random variables (x_i, y_i) into a two dimensional plot (Asuero et al., 2006) then it displays the visual summary of linear, nonlinear or other relationship base on the points. The scatter plots were generated to present the linear correlation calculation results of spectra of each type of the minerals amongst the universal spectral library and each of the three extracted spectral libraries. Column plot were used to compare the similarities of percentages between the reproducibility and the producer accuracy. Box plots were used to show the relationship between the position of the deepest absorption features and the classification label for the same pixel. The box plot was used to compare the classification results with the result generated by the minimum wavelength of software HypPy.

3. RESULT

This section presents the results of pre-processing, wavelength mapping, endmember extraction, scatter plot, mineral mapping, classification results comparison, accuracy assessment et al. in this research. Without particular claiming, the results presented in this section are created by software ENVI (Harris Geospatial Solutions, 2018).

3.1. Atmospheric correction

The radiance-at-sensor images were atmospherically corrected by a model-based method FLAASH. Subsequently, the result was inspected in two phases: initially, the mean spectra of the original images and post-correction images were compared to roughly check the overall quality of the atmospheric correction results (shown in Figure 3.1 A). The overall spectrum for the whole corrected image shows two over correction convex (shown in Figure 3.1 A) around the atmospheric absorption wavelength range $0.9 \mu\text{m}$ and $1.4 \mu\text{m}$ respectively. But these over correction convenes were not observed in the wavelength range ($2.0\text{-}2.5 \mu\text{m}$) that used in this research (shown in Figure 3.1 B). Afterwards, the performance of the ATM correction was specifically assessed. Pixels at the same location with six typical mineral depositing locations observed in the Cuprite Mineral Map produced by Swayze et al. (2014) were selected and the spectra within those pixels were extracted. A comparison between those extracted spectra and corresponding mineral spectra derived from the USGS library was done (shown in Figure 3.2 A, B, and C). The spectra that extracted from the corrected images shown similar spectral curves with the spectra of corresponds mineral from the USGS library.

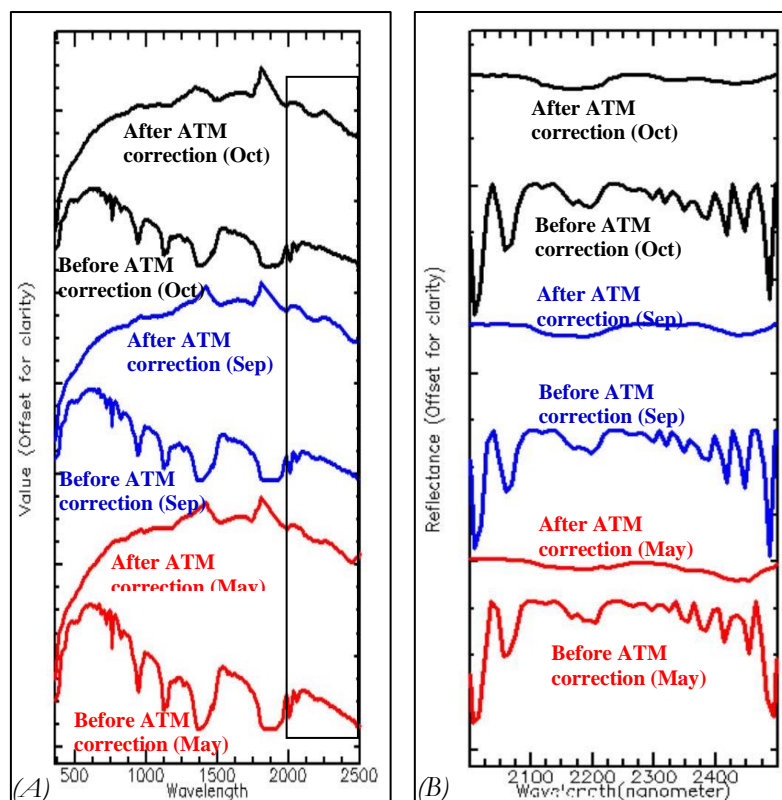


Figure 3.1 (A) shows the comparison of overall spectra derived from May, Sep, and Oct image, before and after the atmospheric correction respectively.; (B) presents the comparison of overall spectra whose wavelength is 2000 - 2500nm derived from May, Sep, and Oct image, before and after the atmospheric correction respectively. Which is also the spectra surrounded by a dark outline of Figure 3.1 (A).

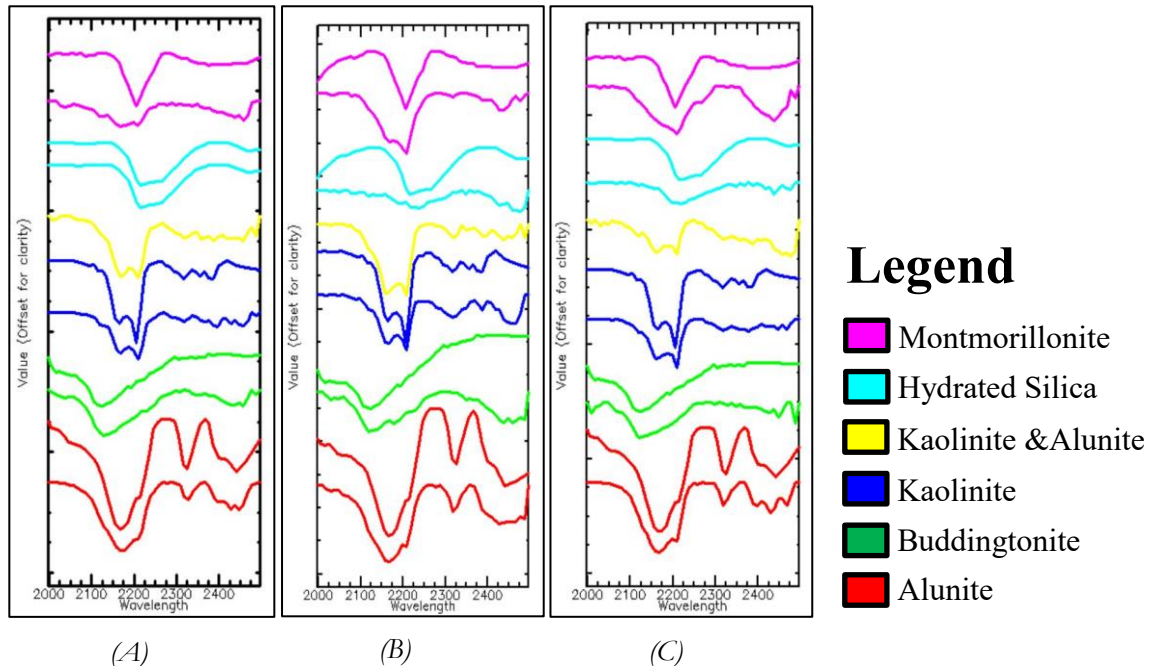


Figure 3.2 (A), (B), and (C) shows the comparison between spectra collected from May, Sep, and Oct image respectively and their corresponding mineral spectrum from the USGS library. For the comparison of each mineral, the upper spectrum is referenced from the USGS spectral library while the lower one was collected from the images.

3.2. Data resize

Figure 3.5 shows six images in greyscale, of which images (A)(C)(E) are before ATM correction and (B)(D)(F) are after ATM correction. Afterwards, the (B)(D)(F) images have been spectrally subset from 224 bands to the 1998.28-2497.04 nm. The wavelength range finally used in this research was 2048 nm to 2308 nm. The range 2120 nm to 2250 nm contains the first absorption features while 2050-2120 nm and 2250-2300 nm were the spectral shoulders of the targeting alteration minerals.

3.3. Wavelength mapping

Figure 3.3 displays the statistic result of the frequency that a wavelength value was detected as a position of the deepest absorption feature. It shows that for the spectra carried by the pixels of hyperspectral datasets used in this research, the diagnostic spectral features concentrate around two wavelength ranges which are around from 2120 nm to 2250 nm and around from 2420 nm to 2480 nm. Figure 3.4 presents wavelength maps that were created with HypPy software. The colours represent corresponding wavelength value and the brightness shows the absorption depth.

Based on Figure 3.3, another result was observed and summarized that for the spectra carried by the pixels of hyperspectral datasets used in this research, the first diagnostic spectral features concentrate around two wavelength ranges which are around from 2120 nm to 2250 nm and around from 2420 nm to 2480 nm. Based on the Cuprite Mineral Map produced by Swayze et al (2014), the alteration minerals in this area are identified as *alunite*, *buddingtonite*, *kaolinite*, *alunite & kaolinite*, *hydrated silica*, and *montmorillonite*. None of these minerals has the first diagnostic spectral features of a wavelength range from 2420 nm to 2480 nm (Swayze et al., 2014). As well as this latter wavelength concentrating range is an atmospheric absorption range (van der Werff & van der Meer, 2015), thus the wavelength range 2120 nm to 2250 nm was considered as the concentrating range of the mineral spectral signatures. Therefore, the wavelength range of the hyperspectral images used was further subsetted to 2050 nm to 2300 nm in this research. The range 2120 nm to 2250 nm contains the first absorption features while 2.05-2.12 μ m and 2.25-2.3 μ m were

EVALUATING REPRODUCIBILITY AND ACCURACY OF HYPERSPECTRAL MINERAL MAPS USING MULTI-TEMPORAL AVIRIS IMAGES OF CUPRITE, NEVADA, USA kept as the spectral shoulders of the targeting alteration minerals. The further spectral subsetting process was conducted to reduce the impact of other spectral curve features around the diagnostic absorption features of the hydrothermal alternative minerals in the study area.

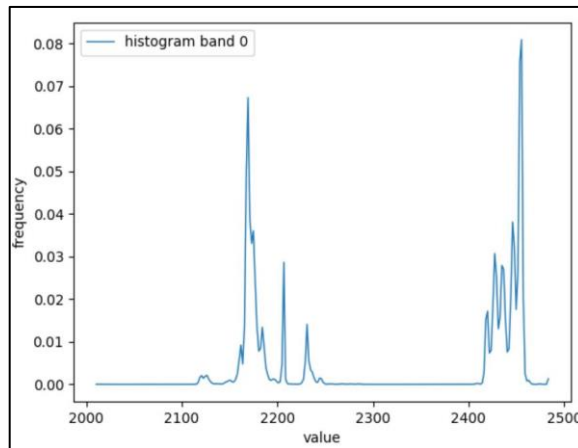


Figure 3.3 frequency for the wavelength position of the first peak

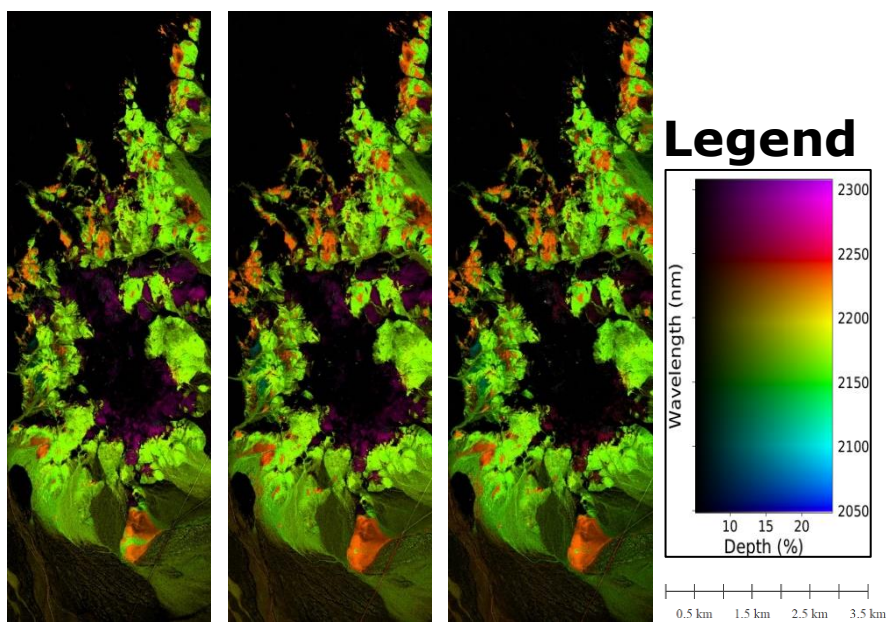
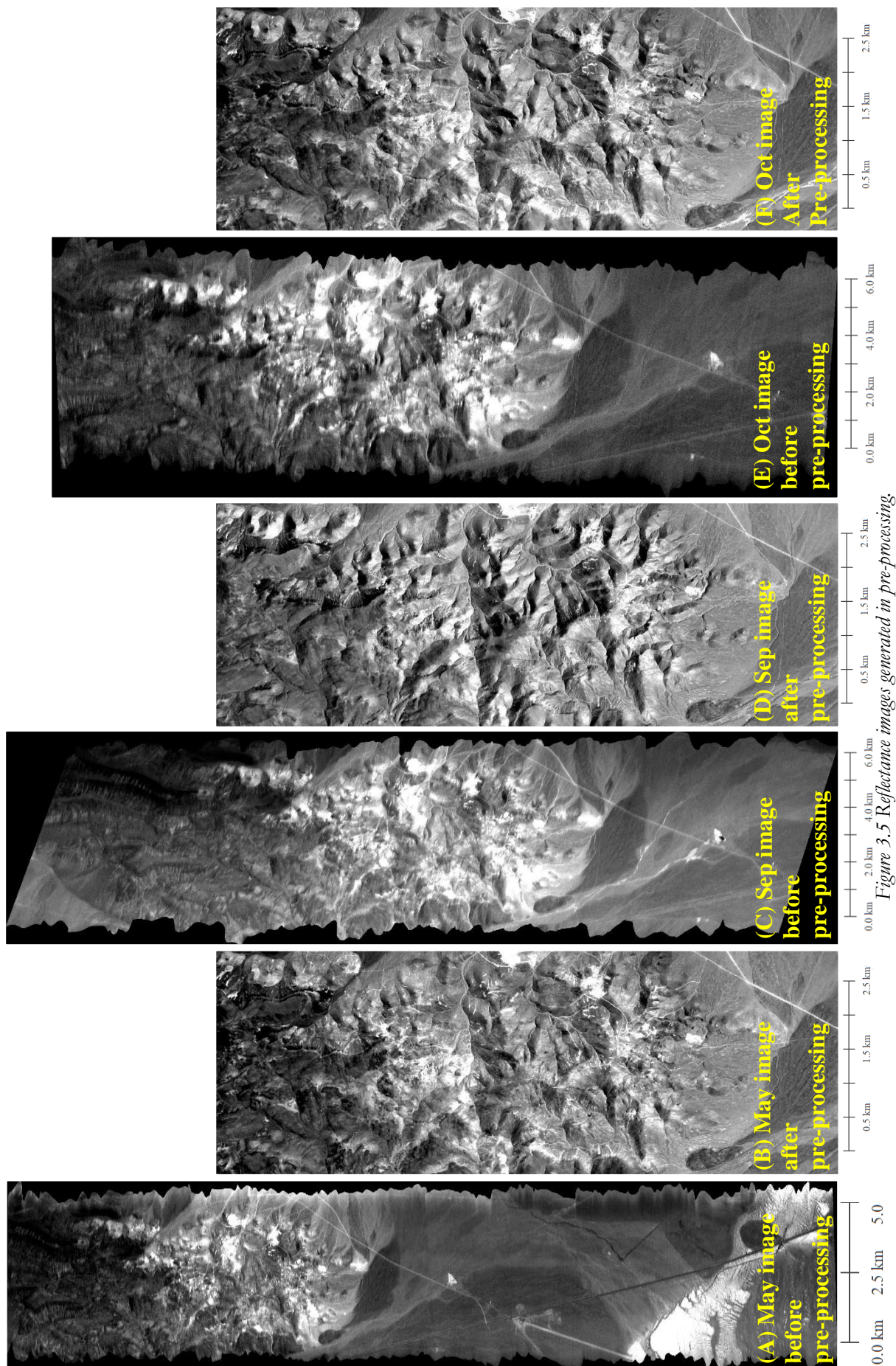


Figure 3.4 (A) shows the wavelength map derived from May image; (B) is the wavelength map produced based on the Sep image; (C) presents the wavelength map created depends on the Oct image.



3.4. Endmember extraction

The spectra of extracted endmember libraries and the universal spectral library are shown in Figure 3.6. For the extracted endmember libraries, six mineral spectra were selected and labelled from all the spectra extracted by the SSEE method for each of the hyperspectral images based on the comparison with mineral spectra from the USGS library. The spectra of the universal endmember library were created through the averaging of the three corresponding mineral spectra from each of the extracted endmember library, except for *montmorillonite*. The spectrum of *montmorillonite* in the universal library is directly selected from the endmember library of the Sep image because this spectrum was only found in the Sep image by the SSEE method. And the endmember of *montmorillonite* in the extracted libraries that derived from the May Image and the Oct image were extracted from the similar location where the spectrum of *montmorillonite* was found in the Sep image.

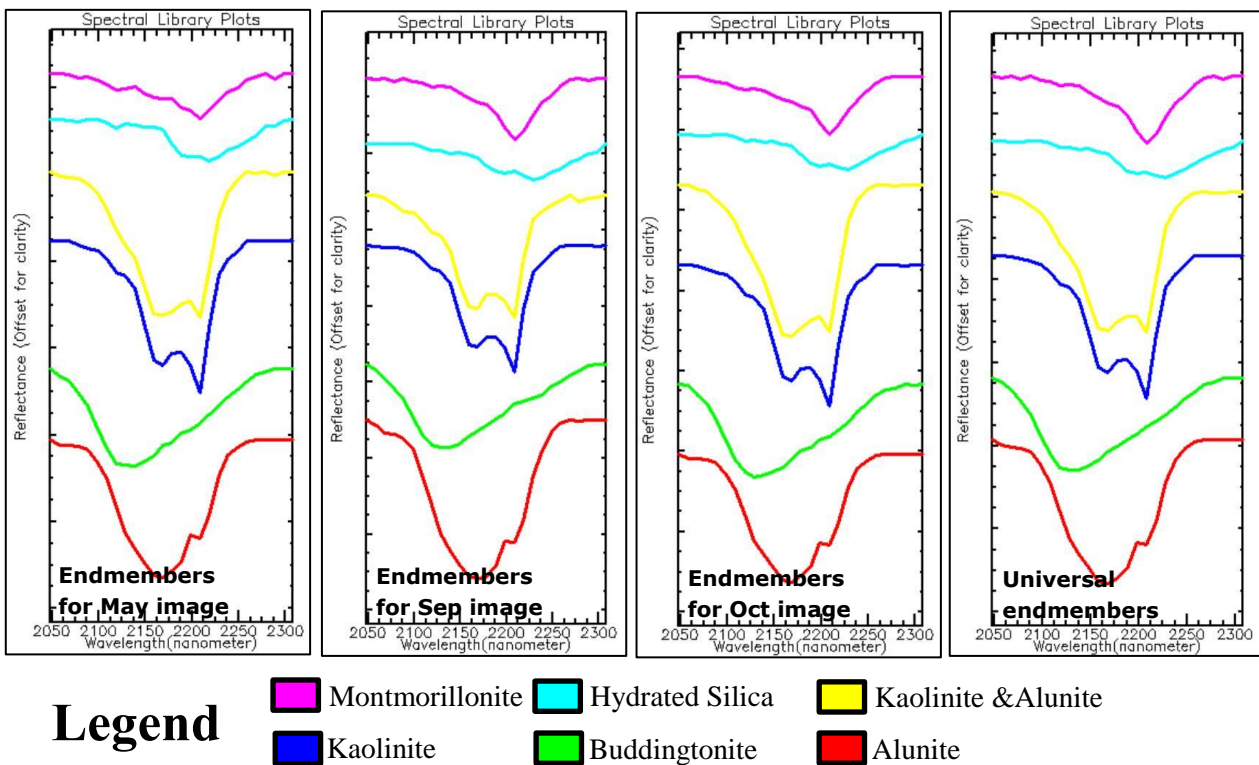


Figure 3.6 Spectral endmember libraries used in this research & legend

As Figure 3.6 shows, these spectra are *alunite*, *buddingtonite*, *kaolinite*, *alunite* & *kaolinite*, *hydrated silica*, and *montmorillonite*. *Alunite* shows diagnostic absorption features at 2168.51 nm and 2208.46 nm. *Buddingtonite* presents a wide spectral feature and its deepest absorption features of it located at 2128.51 nm. Double absorption features are shown by the endmember of *kaolinite*, the deepest feature locates at 2208.46 nm while the second peak at 2168.51 nm. *Kaolinite* & *alunite* is a mixed endmember that presents a similar spectral shape as *kaolinite*, but there is no clear absorption difference between these two peaks, which is influenced by the superposition of both *kaolinite* and *alunite*. *Hydrated silica* shows a very shallow, wide and noisy spectral features, of which the deepest absorption feature is 2228.43 nm but no clear difference with other peaks of its spectrum. Finally, the diagnostic absorption feature of *montmorillonite* has the same wavelength with *hydrated silica*, which is 2228.43 nm. But on the contrary of *hydrated silica*, the signature of *montmorillonite* shows a sharper and clearer curve even if it is also noisy. Especially for the endmember of *montmorillonite* extracted from the May image, its spectral curve shows several slight peaks around its real absorption feature (see Figure 3.6).

3.5. Endmember similarity

Before using the endmember libraries that were shown in Figure 3.6 for mineral mapping, the similarities between them were measured by linear spectral correlation (shown in Table 3.1 and Table 3.2). The tables show the linear spectral correlations across endmembers extracted from each of the hyperspectral images and corresponding endmember from the universal library. The values of correlation coefficients (shown in both Table 3.1 and Table 3.2) for the comparison between each pair of the endmembers shown in Figure 3.6 are higher than 0.95 and some of them even equal to 1.

Table 3.1 Linear Spectral correlation of extracted endmembers

	May Image: Sep Image	May Image: Oct Image	Sep Image: Oct Image
Alunite	0.994843	1	0.994843
Buddingtonite	0.992662	0.996862	0.995189
Kaolinite	0.999092	1	0.999092
Kaolinite+ Alunite	0.950897	0.996701	0.96604
Hydrated Silica	0.98984	0.99685	0.99628
Montmorillonite	0.974933	0.98503	0.994367

Table 3.2 Linear Spectral correlation across extracted libraries and the universal library

	May: Universal	Sep: Universal	Oct: Universal
Alunite	0.999429	0.997703	0.999429
Buddingtonite	0.998265	0.997519	0.999110
Kaolinite	0.999893	0.999609	0.999893
Kaolinite+ Alunite	0.992421	0.981317	0.997324
Hydrated Silica	0.997070	0.997611	0.999597
Montmorillonite	0.989456	0.996425	0.998409

3.6. Image-to-image registration

For the spatial alignment of the three multitemporal hyperspectral images, the image-to-image registration tool built-in to the software ENVI was used. 70 GCPs (ground control points) were automatically selected for the registration of the May image and Sep image, while 81 GCPs were automatically selected for the registration of the May image and Oct image (shown in Figure 3.7). The self-assessment (see in Appendix III) of these GCPs shows the RMS error as 0.508 m and 0.624 m for the accuracy of the aligning results of the May image and Sep image as well as May image and Oct image respectively. These accuracy indexes present the shift amongst pixels, with the same coordinates, from each of the hyperspectral image scenes have already much lower than one pixel, as the pixel size of the hyperspectral images used for registration is 3.3 m. Therefore, the spatial accuracy for image aligning was considered as acceptable for pixel-based comparison.

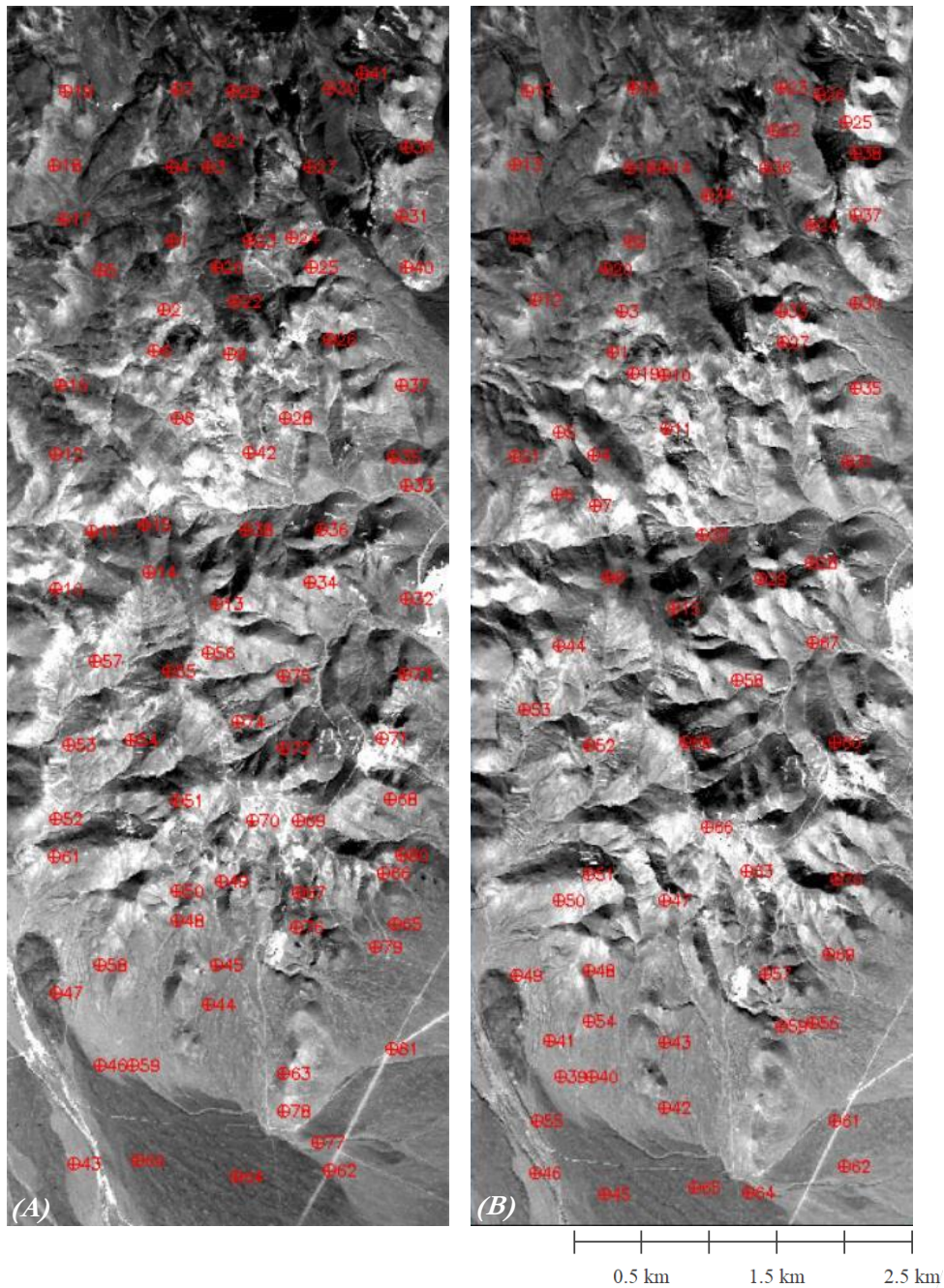


Figure 3.7 (A) shows the GCPs distribution of Sep image; (B) shows the GCPs distribution upon the Oct image.

Moreover, after the process of registration with these two portions of GCPs, the image-to-image registration results were assessed by the dynamic link through the visual inspection. And these registered results presented that they are as close as possible according to both the low RMS errors and the dynamic visual estimations. Therefore, for this research, the co-registered pixels while from different hyperspectral images are assumed as overlapping with the same coordinates.

3.7. Measurement of the reproducibility

3.7.1. Mineral maps produced through the extracted endmember library

Figure 3.8 shows the classification results derived from the multitemporal hyperspectral images and produced by the SAM method with the extracted endmembers. Huge differences can be observed that the distribution of each mineral type was changed follows the change of time (shown in Figure 3.8).

The low consistency shown in Figure 3.8 was supported by the comparison results generated by the confusion matrix (shown in Table 3.3, Table 3.4, and Table 3.5). The overall accuracy between May image and Sep image is around 59%, between May image and Oct image is around 61%, as well as between Sep image and Oct image is around 58%.

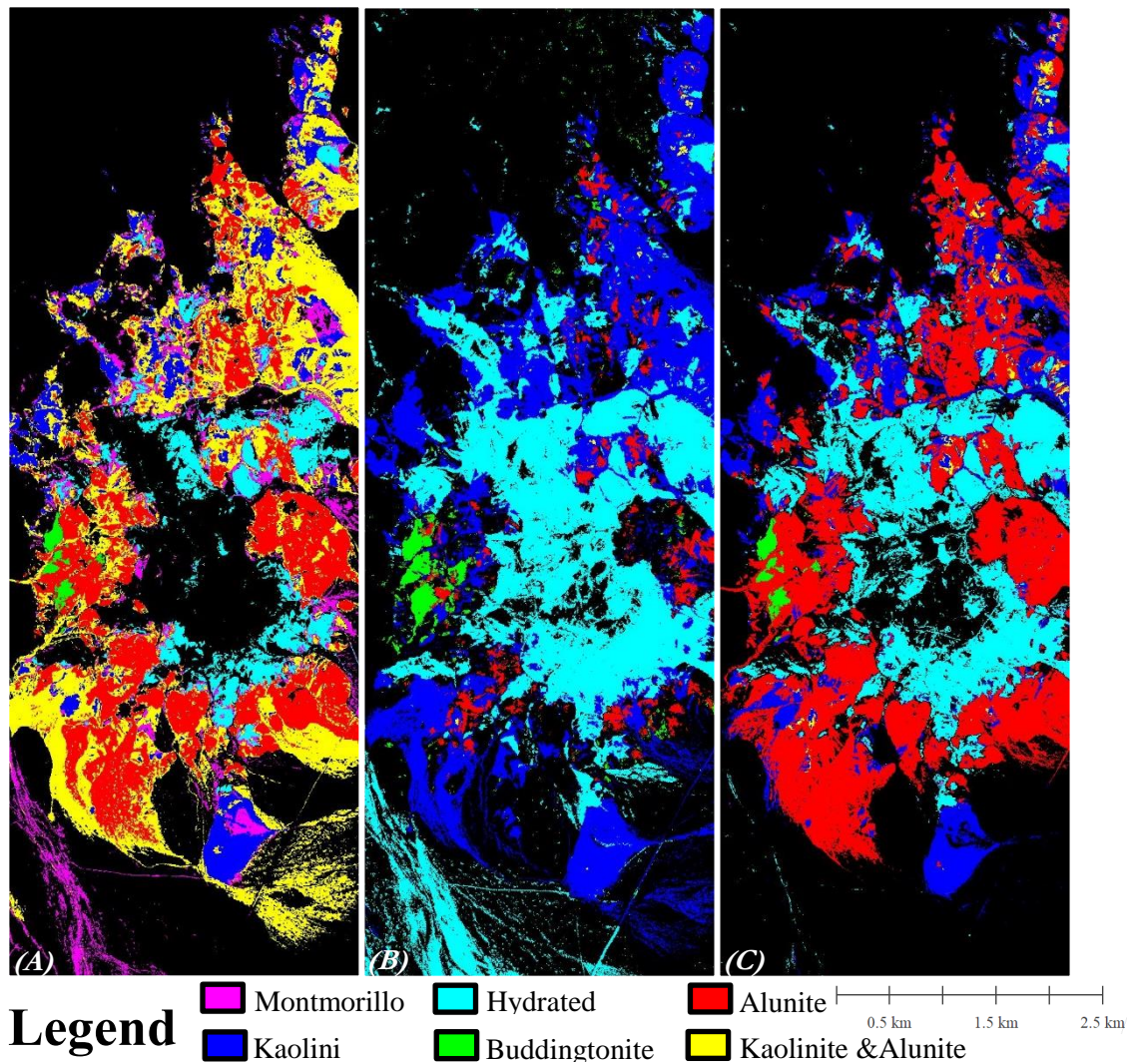


Figure 3.8 (A), (B), and (C) are SAM classification results, that were classified through the extracted endmember libraries and one set of various thresholds, derived from May image, Sep image, and Oct image respectively.

Table 3.3 Confusion matrix of the comparison between May image and Sep image

Classification result of Sep image	Classification result of May image							Total	Error of Commission(%)	User Accuracy(%)
	Unclassified	Alunite	Buddingtonite	Kaolinite	Alunite & Kaolinite	Hydrated Silica	Montmorillonite			
Unclassified	471352	92331	44	1354	37521	1909	10523	615034	23.36	76.64
Alunite	16	18056	0	5	2221	0	2	20300	11.05	88.95
Buddingtonite	1805	5590	3312	0	18	0	0	10725	69.12	30.88
Kaolinite	4593	5496	1	40715	62156	638	3148	116747	65.13	34.87
Alunite & Kaolinite	0	0	0	768	76	0	0	844	91	9
Hydrated Silica	124876	105	1	536	606	43144	31292	200560	78.49	21.51
Montmorillonite	11	0	0	15	1	13	70	110	36.36	63.64
Total	602653	121578	3358	43393	102599	45704	45035	964320		
Error of omission(%)	21.79	85.15	1.37	6.17	99.93	5.6	99.84			
Producer Accuracy(%)	78.21	14.85	98.63	93.83	0.07	94.4	0.16		Overall Accuracy	59.81%

Table 3.4 Confusion matrix of the comparison between May image and Oct image

Classification result of Oct image	Classification result of May image							Total	Error of Commission(%)	User Accuracy(%)
	Unclassified	Alunite	Buddingtonite	Kaolinite	Alunite & Kaolinite	Hydrated Silica	Montmorillonite			
Unclassified	470880	23953	1009	17918	28479	9813	23141	575193	18.14	81.86
Alunite	55005	73364	1357	7183	45358	4829	7320	194416	62.26	37.74
Buddingtonite	794	1663	957	26	202	1	0	3643	73.73	26.27
Kaolinite	17612	6510	21	14423	16270	1926	4996	61758	76.65	23.35
Alunite & Kaolinite	345	853	0	634	1847	308	144	4131	55.29	44.71
Hydrated Silica	57467	15014	5	3017	10107	28769	9277	123656	76.73	23.27
Montmorillonite	550	221	9	192	336	58	157	1523	89.69	10.31
Total	602653	121578	3358	43393	102599	45704	45035	964320		
Error of omission(%)	21.87	39.66	71.5	66.76	98.2	37.05	99.65			
Producer Accuracy(%)	78.13	60.34	28.5	33.24	1.8	62.95	0.35		Overall Accuracy	61.22%

Table 3.5 Confusion matrix of the comparison between Sep image and Oct image

Classification result of Oct image	Classification result of Sep image							Total	Error of Commission(%)	User Accuracy(%)
	Unclassified	Alunite	Buddingtonite	Kaolinite	Alunite & Kaolinite	Hydrated Silica	Montmorillonite			
Unclassified	438723	3179	3100	37076	91	92958	66	575193	23.73	76.27
Alunite	117134	11979	5247	36759	225	23045	27	194416	93.84	6.16
Buddingtonite	1622	39	1875	62	0	45	0	3643	48.53	51.47
Kaolinite	24420	1461	209	28637	416	6606	9	61758	53.63	46.37
Alunite & Kaolinite	965	230	9	2434	48	445	0	4131	98.84	1.16
Hydrated Silica	31490	3385	260	11272	64	77177	8	123656	37.59	62.41
Montmorillonite	680	27	25	507	0	284	0	1523	100	0
Total	615034	20300	10725	116747	844	200560	110	964320		
Error of omission(%)	28.67	40.99	82.52	75.47	94.31	61.52	100			
Producer Accuracy(%)	71.33	59.01	17.48	24.53	5.69	38.48	0		Overall Accuracy	57.91%

3.7.2. Maps classified by the unique threshold

For verifying of the assumption about the influence of various threshold for reproducibility of the classifier SAM, three classification results (shown in Figure 3.9) were generated again based on the May image, Sep image, and Oct image respectively with its corresponding extracted endmember libraries. However, the classification thresholds for each mineral of each image were set as a unique value “0.1”. But, these results can be easily assessed as a poor classification just by the visual comparison between these and the Cuprite Mineral Map produced by Swayze et al. (2014) as the ground truth data. Therefore, the reproducibility of classifier SAM cannot be enhanced by using a unique classification threshold.

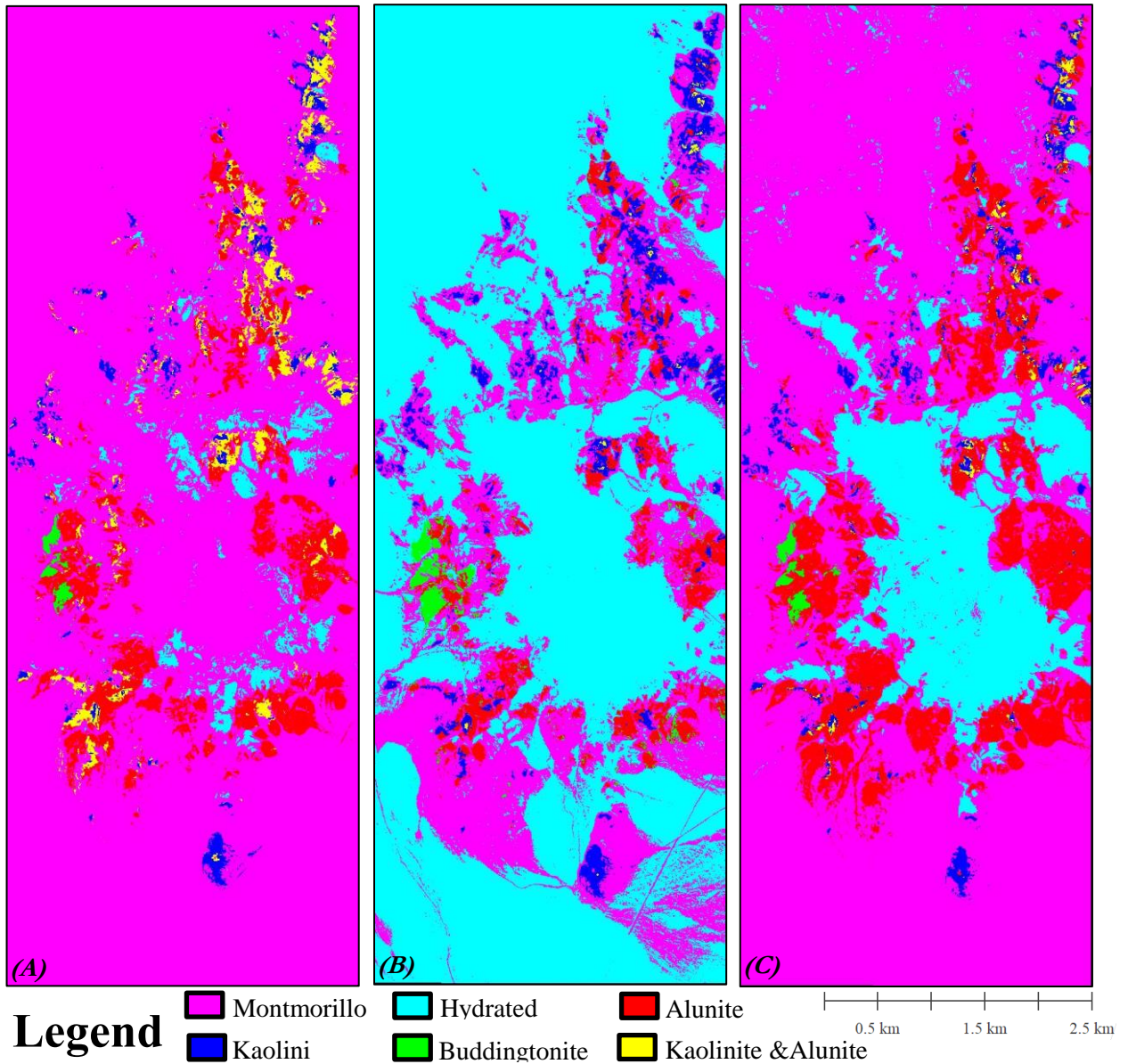


Figure 3.9 (A), (B), and (C) are SAM classification results, that were classified through the extracted endmember libraries and “0.1” as threshold for every mineral, derived from May image, Sep image, and Oct image respectively.

3.7.3. Differences amongst the original images

The assumption that the differences amongst the original radiance datasets result in the influence of reproducibility was investigated. Initially, three multitemporal hyperspectral image scenes were paired to three pairs which are May image and Sep image, May image and Oct image, and the Sep image and Oct image. Afterwards, change detection method was used to search the pixels that have different values in the same location between a pair of the original datasets used for classification (threshold see Appendix IV). The change detection result will be present in a red and blue map, of which red indict positive differences and brighter red pixel means higher value. While blue express negative and darker blue shows an even lower value (Harris Geospatial Solution Inc, 2018f). There are a lot of pixels with different values according to the difference maps (shown in Figure 3.10) created by the change detection.

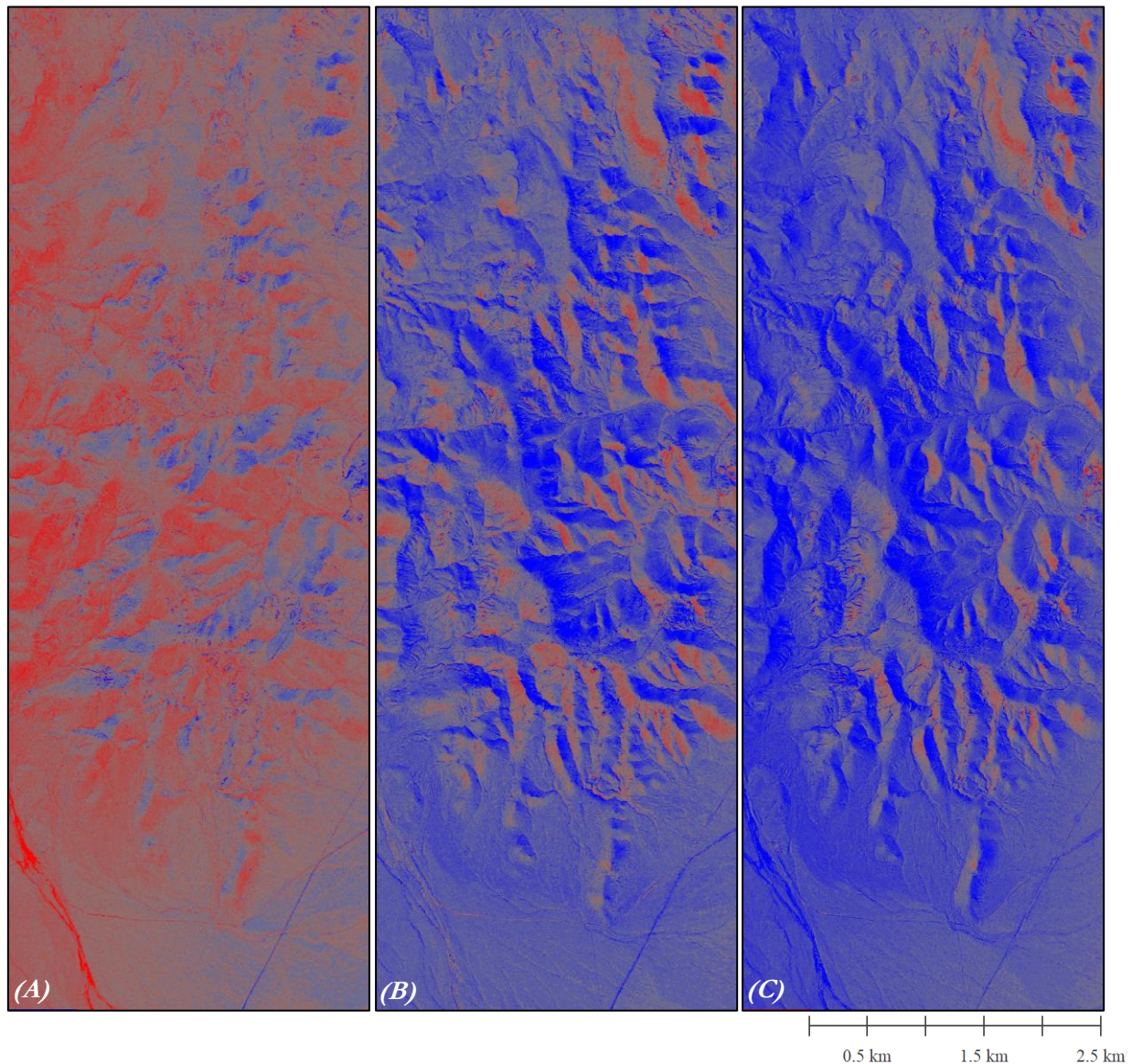


Figure 3.10 Differences maps generated by the change detection, of which (A) shows the differences between May image and Sep image; (B) presents the differences between Sep image and Oct image; (C) shows the differences between May image and Oct image; the different value from positive to negative was present from lighter red to dimmer blue in this map.

The composition of these pixels observed in Figure 3.10 presents similarity as the shape of shadow in the three original images (shown in Figure 3.5 B, D, and F). These shadows may be jointly made by the different sun angles of the multitemporal AVIRIS scenes and the complicate topography of this area. The differences amongst sun angles of different images were caused by the AVIRIS images used in this research were acquired in different seasons and time. Besides that, the size and direction of shadow in a mountain area like the Cuprite is highly related with the sun angle and other illumination conditions.

Therefore, the change of sun angles following the change of time will change the shadow condition in Cuprite. Then the consistency amongst the original multitemporal AVIRIS images of this area was disturbed by these shadow differences.

Figure 3.12 shows the classification results derived from the similarized hyperspectral images and differences of mineral distribution were still can be observed of them. Even those pixels that have hugely different values between each other have already been excluded. The pixel-based Comparison between classification results derived from May-Sep image and Sep-May image shown in Table 3.6 and the overall accuracy and/or overall similarity between them is around 82%. The pixel-based Comparison between classification results derived from May-Oct image and Oct-May image shown in Table 3.7 and the overall accuracy and/or overall similarity between them is around 94%. The pixel-based Comparison between classification results derived from Sep-Oct and Oct-Sep image are shown in Table 3.8 and the overall accuracy and/or overall similarity between them is around 96%.

The identification similarity of the comparison between May-Sep image and Sep-May image is around 25%, of the comparison between May-Oct image and Oct-May image is around 50%, as well as of the comparison between Sep-Oct and Oct-Sep image is around 48%. To clearly understand the influence of the differences between the original images, the identification similarity of the classification results that derived from the three original hyperspectral images was compared with the identification similarity of the classification results derived from the three pairs of similarized images (shown in Figure 3.11). The identification similarity of comparison between May image and Sep image is around 21%, between May image and Sep image is around 24%, and between Sep image and Oct image is around 23%.

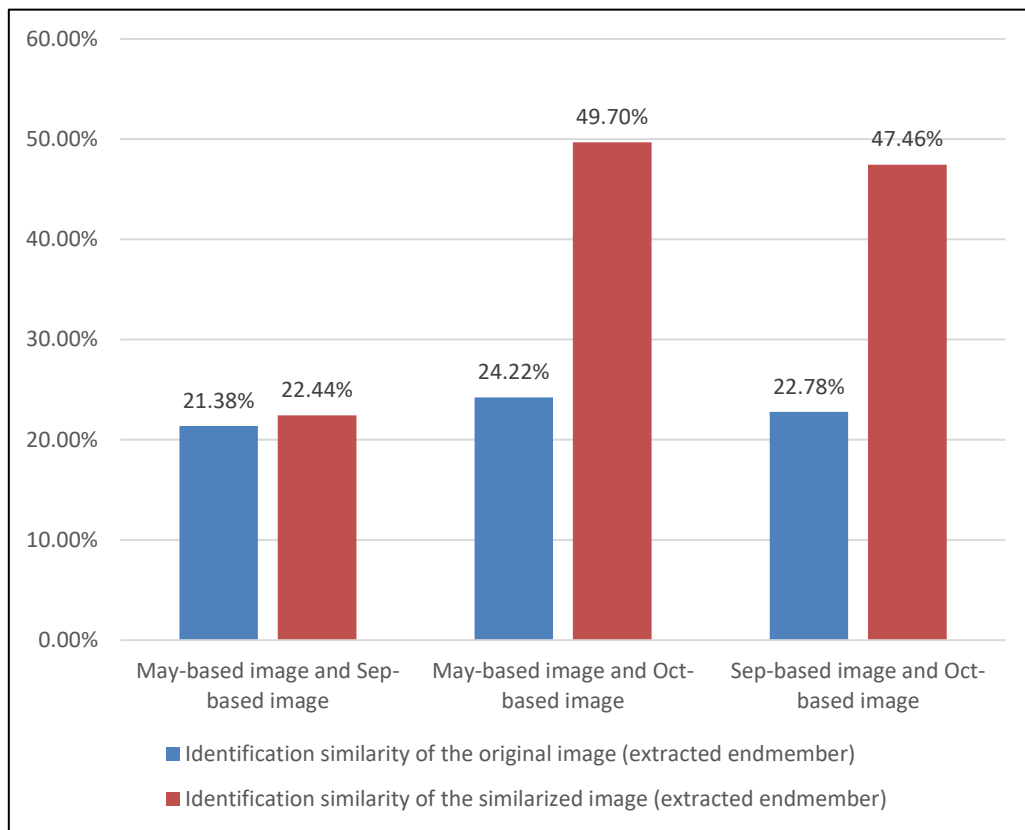


Figure 3.11 Comparison of identification similarity between results derived from the original images and the results derived from the similarized images.

Table 3.6 Comparison of classification results between May-Sep image and Sep-May image

Classification result of Sep-May image	Classification result of May-Sep image							Total	Error of Commission(%)	User Accuracy(%)
	Unclassified	Alunite	Buddingtonite	Kaolinite	Alunite & Kaolinite	Hydrated Silica	Montmorillonite			
Unclassified	742721	41654	8	643	17528	1042	4559	808155	8.1	91.9
Alunite	8	8307	0	1	961	0	0	9277	10.46	89.54
Buddingtonite	755	2031	776	0	5	0	0	3567	78.25	21.75
Kaolinite	1391	2040	0	21237	27021	245	1377	53311	60.16	39.84
Alunite & Kaolinite	0	0	0	334	16	0	0	350	95.43	4.57
Hydrated Silica	55261	48	0	235	233	19235	14020	89032	78.4	21.6
Montmorillonite	2	0	0	6	0	6	26	40	35	65
Total	800138	54080	784	22456	45764	20528	19982	963732		
Error of omission(%)	7.18	84.64	1.02	5.43	99.97	6.3	99.87		Overall Accuracy	82.21%
Producer Accuracy(%)	92.82	15.36	98.98	94.57	0.03	93.7	0.13	Identification Similarity		22.44%

Table 3.7 Comparison of classification results between May-Oct image and Oct-May image

Classification result of Oct-May image	Classification result of May-Oct image							Total	Error of Commission(%)	User Accuracy(%)
	Unclassified	Alunite	Buddingtonite	Kaolinite	Alunite & Kaolinite	Hydrated Silica	Montmorillonite			
Unclassified	842003	453	18	653	4586	463	6181	854357	1.45	98.55
Alunite	4842	35469	112	99	15396	12	90	56020	36.69	63.31
Buddingtonite	31	85	821	0	1	0	0	938	12.47	87.53
Kaolinite	532	49	1	9480	6109	163	427	16761	43.44	56.56
Alunite & Kaolinite	0	4	0	110	995	0	0	1109	10.28	89.72
Hydrated Silica	15121	11	0	72	107	13301	5416	34028	60.91	39.09
Montmorillonite	48	2	0	11	7	15	436	519	15.99	84.01
Total	862577	36073	952	10425	27201	13954	12550	963732		
Error of omission(%)	2.39	1.67	13.76	9.06	96.34	4.68	96.53		Overall Accuracy	93.65%
Producer Accuracy(%)	97.61	98.33	86.24	90.94	3.66	95.32	3.47	Identification Similarity		49.7%

Table 3.8 Comparison of classification results between Sep-Oct image and Oct-Sep image

Classification result of Oct-Sep image	Classification result of Sep-Oct image							Total	Error of Commission(%)	User Accuracy(%)
	Unclassified	Alunite	Buddingtonite	Kaolinite	Alunite & Kaolinite	Hydrated Silica	Montmorillonite			
Unclassified	886192	8	358	1506	0	7575	1	895640	1.05	98.95
Alunite	21225	4780	989	6010	0	94	0	33098	85.56	14.44
Buddingtonite	4	0	164	0	0	0	0	168	2.38	97.62
Kaolinite	563	7	0	9802	169	208	6	10755	8.86	91.14
Alunite & Kaolinite	2	49	0	848	75	0	0	974	92.3	7.7
Hydrated Silica	597	0	0	134	0	21975	0	22706	3.22	96.78
Montmorillonite	36	0	0	32	0	316	7	391	98.21	1.79
Total	908619	4844	1511	18332	244	30168	14	963732		
Error of omission(%)	2.47	1.32	89.15	46.53	69.26	27.16	50		Overall Accuracy	95.77%
Producer Accuracy(%)	97.53	98.68	10.85	53.47	30.74	72.84	50	Identification Similarity		47.46%

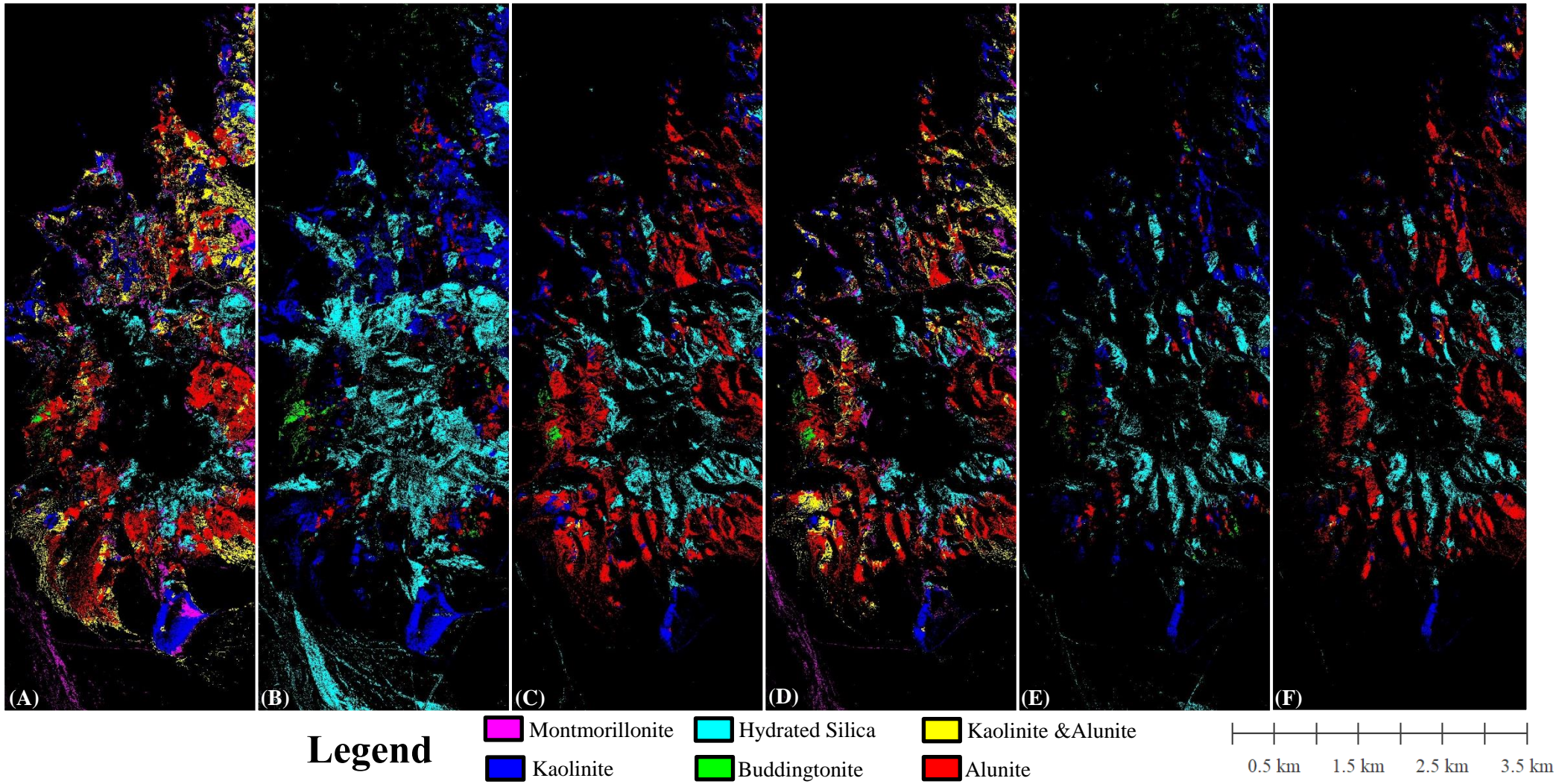


Figure 3.12 (A) shows the classification result derived from the May-Sep image; (B) shows the classification result derived from the Sep-May image; (C) shows the classification result derived from the May-Oct image; (D) shows the classification result derived from the Oct-May image; (E) shows the classification result derived from the Sep-Oct image; (F) shows the classification result derived from the Oct-Sep image.

3.7.4. Influence of vegetation

The distribution of vegetation of each hyperspectral image used was detected by the algorithm NDVI then they were classified by the tool ROI with the threshold suggested by Weier & Herring (2000) and Cheng et al.(2008) suggested that 0.1 and below presents the ground surface without vegetations, 0.1-0.2 can be considered as no vegetation or sparse vegetation, 0.2-0.3 indicates grassland or barren, and 0.6-0.8 presents the forest (shown in Figure 3.13).

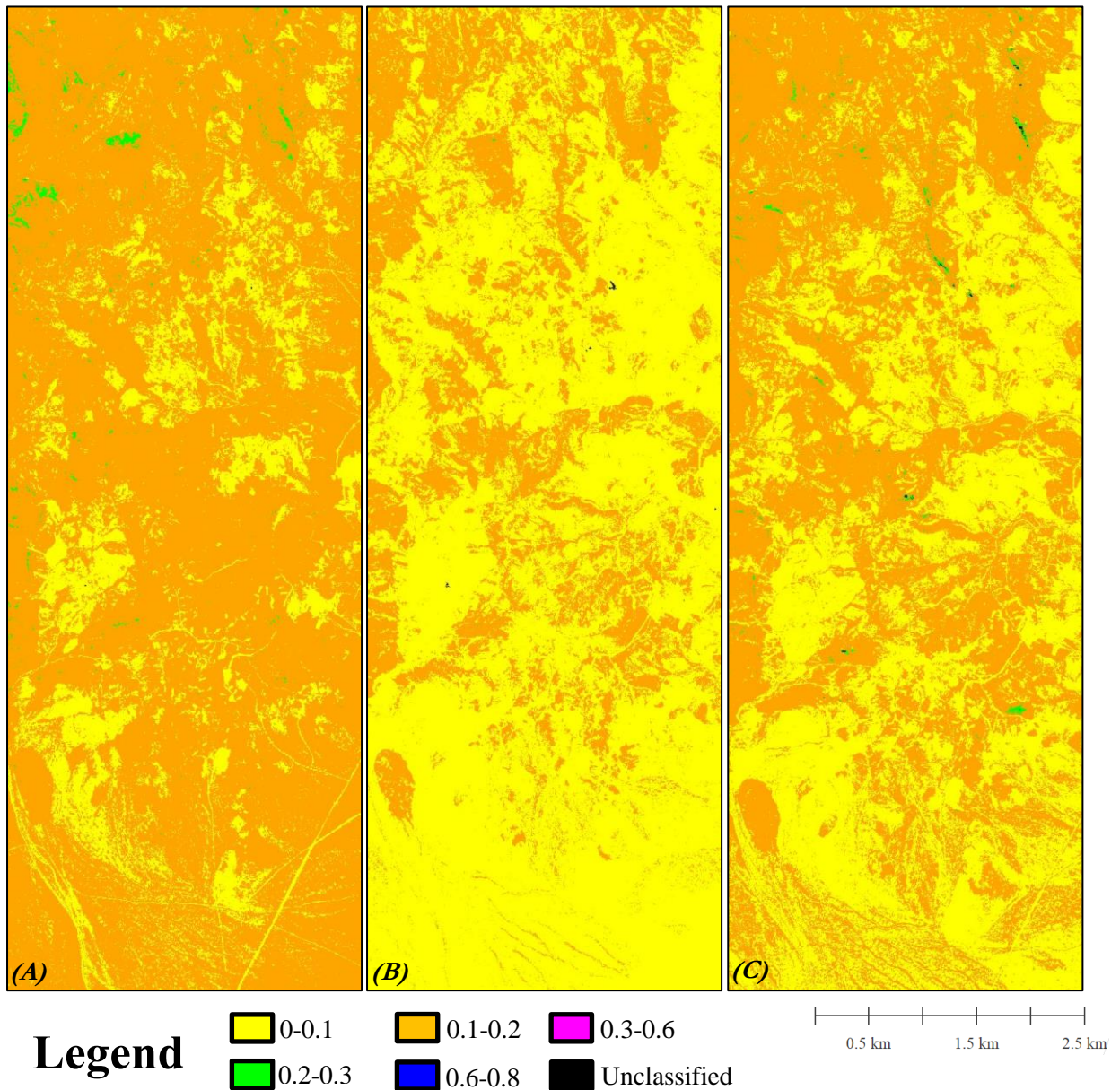


Figure 3.13 (A), (B), and (C) presents the classified NDVI results that derived from May image, Sep image, and Oct image respectively.

The interpolation results of these classified NDVI images (shown in Figure 3.14, 3.15, and 3.16) present that only sparse vegetation distributes in this region, so that the vegetation condition in the study area was considered as it cannot influence the differences of classification results as shown in Figure 3.8.

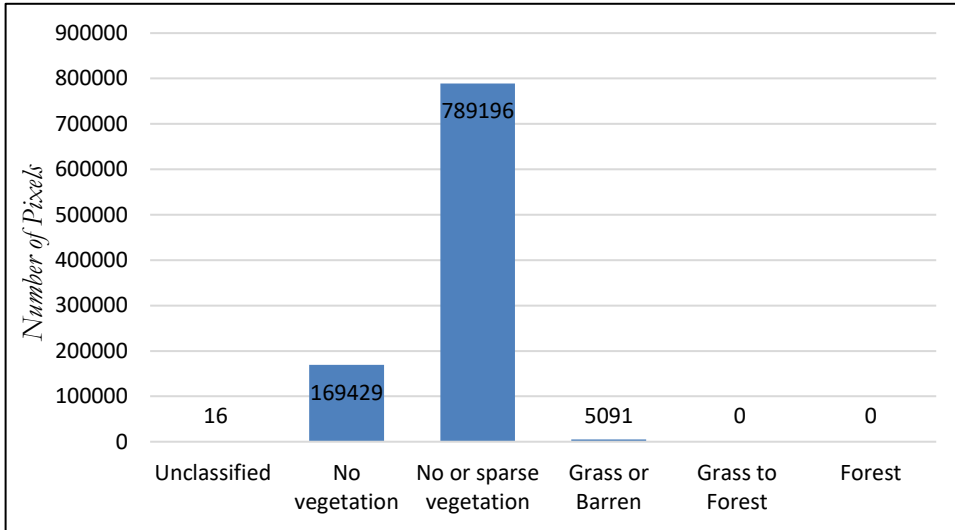


Figure 3.14 Vegetation distribution in May image

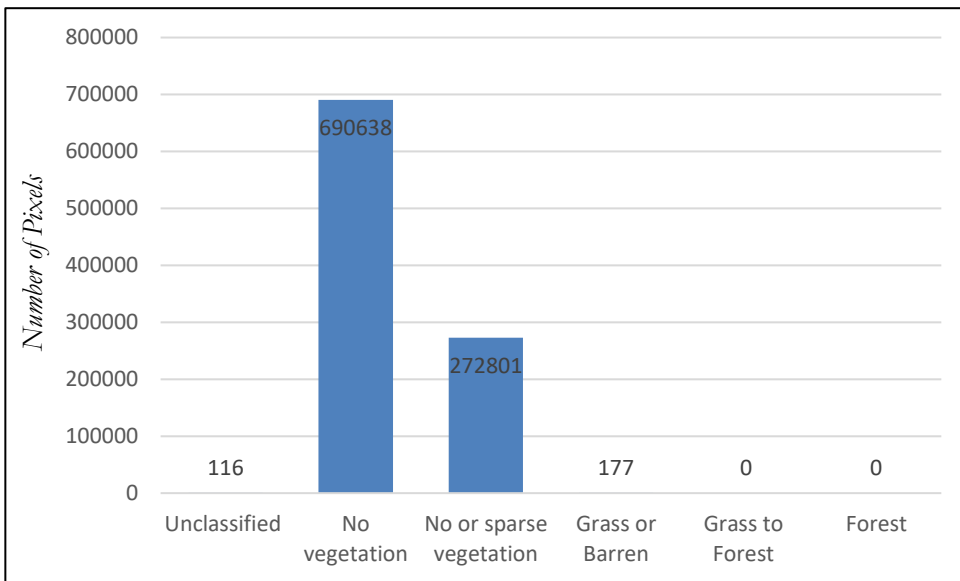


Figure 3.15 Vegetation distribution in Sep image

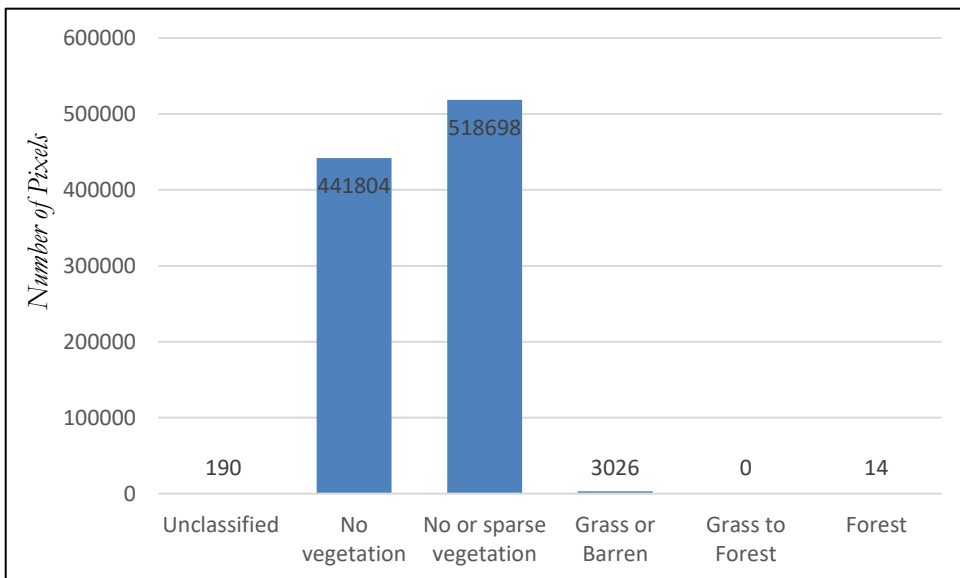


Figure 3.16 Vegetation distribution in Oct image

3.7.5. Influence of endmember library

Eventually, the last assumption that the reproducibility or consistency of SAM classifier is disturbed by the extracted endmember libraries was researched. For the verifying of this hypothesis, the universal endmember library was used for the mineral mapping of May image, Sep image, and Oct image respectively by the method SAM through the consistent classification threshold (see Appendix II) and the results are shown in Figure 3.17.

As the results shown above, results A, B, and C are similar to each other based on the visual inspection. Therefore, the similarity of them was further and specifically estimated by the confusion matrix (shown in Table 3.9, 3.10, and 3.11). Because the overall accuracy presents of the confusion matrix is considered as similarity, thus the similarity between May image and Sep image is 84%, between May image and Sep image is 83%, and between Sep image and Oct image is 89%. Therefore, the hypothesis was confirmed by the fact that multitemporal hyperspectral images over the same area with the universal endmembers can be classified consistently by the SAM.

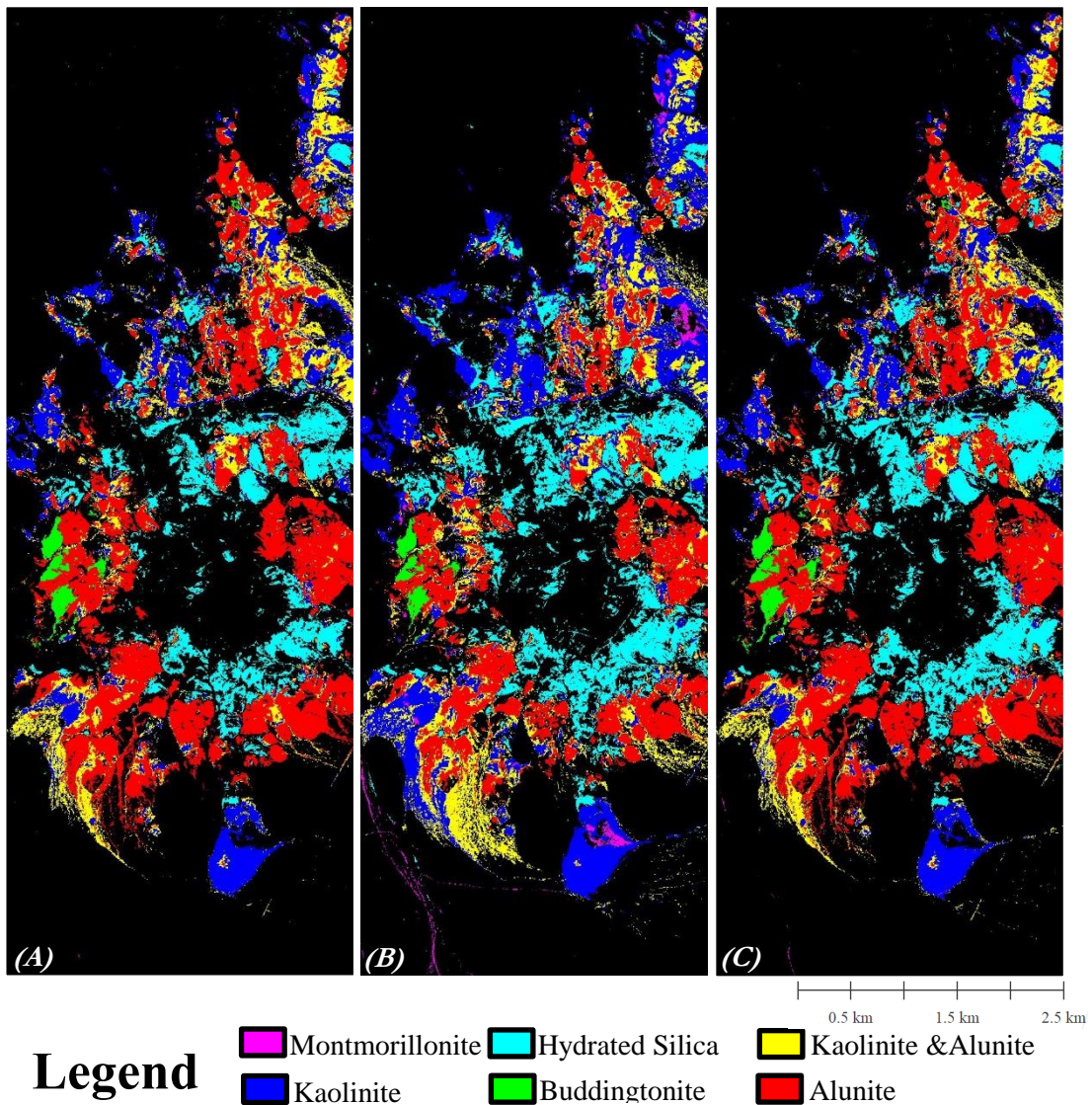


Figure 3.16 (A), (B), and (C) are SAM classification results, that were classified through the universal endmember library and one set of various threshold, derived from May image, Sep image, and Oct image respectively.

Table 3.9 Confusion matrix of the comparison between May image and Sep image

Classification result of Sep image	Classification result of May image							Total	Error of Commission(%)	User Accuracy(%)
	Unclassified	Alunite	Buddingtonite	Kaolinite	Alunite & Kaolinite	Hydrated Silica	Montmorillonite			
Unclassified	607610	1313	36	8988	20586	16176	4448	659157	7.82	92.18
Alunite	9462	77826	63	3220	25761	30	5	116367	33.12	66.88
Buddingtonite	1716	404	3716	3	12	0	0	5851	36.49	63.51
Kaolinite	2476	69	0	53849	1131	354	639	58518	7.98	92.02
Alunite & Kaolinite	4054	707	0	29727	21860	115	94	56557	61.35	38.65
Hydrated Silica	12073	8	0	299	37	53979	12	66408	18.72	81.28
Montmorillonite	230	1	0	209	9	420	593	1462	59.44	40.56
Total	637621	80328	3815	96295	69396	71074	5791	964320		
Error of Omission(%)	4.71	3.11	2.6	44.08	68.5	24.05	89.76			
Producer Accuracy(%)	95.29	96.89	97.4	55.92	31.5	75.95	10.24		Overall Accuracy	84.9752%

Table 3.10 Confusion matrix of the comparison between May image and Oct image

Classification result of Oct image	Classification result of May image							Total	Error of Commission(%)	User Accuracy(%)
	Unclassified	Alunite	Buddingtonite	Kaolinite	Alunite & Kaolinite	Hydrated Silica	Montmorillonite			
Unclassified	610194	1928	38	11230	20746	28895	4482	677513	9.94	90.06
Alunite	11096	76887	92	4367	26259	79	12	118792	35.28	64.72
Buddingtonite	1337	326	3685	3	10	0	0	5361	31.26	68.74
Kaolinite	3439	149	0	50246	1451	599	801	56685	11.36	88.64
Alunite & Kaolinite	4681	1013	0	29926	20840	282	148	56890	63.37	36.63
Hydrated Silica	6623	18	0	354	72	40720	15	47802	14.82	85.18
Montmorillonite	251	7	0	169	18	499	333	1277	73.92	26.08
Total	637621	80328	3815	96295	69396	71074	5791	964320		
Error of omission(%)	4.3	4.28	3.41	47.82	69.97	42.71	94.25			
Producer Accuracy(%)	95.7	95.72	96.59	52.18	30.03	57.29	5.75		Overall Accuracy	83.2613%

Table 3.11 Confusion matrix of the comparison between Sep image and Oct image

Classification result of Oct image	Classification result of Sep image							Total	Error of Commission(%)	User Accuracy(%)
	Unclassified	Alunite	Buddingtonite	Kaolinite	Alunite & Kaolinite	Hydrated Silica	Montmorillonite			
Unclassified	634080	6849	688	4685	8237	22302	672	677513	6.41	93.59
Alunite	7904	102799	470	679	6886	49	5	118792	13.46	86.54
Buddingtonite	441	218	4685	2	15	0	0	5361	12.61	87.39
Kaolinite	4265	607	1	44997	6126	414	275	56685	20.62	79.38
Alunite & Kaolinite	7891	5847	7	7792	35165	145	43	56890	38.19	61.81
Hydrated Silica	4104	35	0	245	93	43221	104	47802	9.58	90.42
Montmorillonite	472	12	0	118	35	277	363	1277	71.57	28.43
Total	659157	116367	5851	58518	56557	66408	1462	964320		
Error of omission(%)	3.8	11.66	19.93	23.11	37.82	34.92	75.17			
Producer Accuracy(%)	96.2	88.34	80.07	76.89	62.18	65.08	24.83		Overall Accuracy	89.7327%

3.7.6. Comparison between solo mineral maps

Solo mineral maps (shown in Figure 3.19) were generated based on the classification results shown in Figure 3.17 to check the reproducibility of each mineral type. These solo mineral maps that belong to the same mineral were compared with the change detection tool and the results were statistically summarized (shown in Figure 3.18).

Based on the information presented in the Figure 3.18, each kind of mineral shows similar reproducibility in any of the three pairs of comparison, except the reproducibility of montmorillonite between Sep image and Oct image, shows double times higher value than the other two ratios. Moreover, *Alunite*, *Kaolinite*, *Alunite & Kaolinite*, and *Hydrated silica* present relatively high consistency but similar values. The lowest reproducibility was observed of *Montmorillonite* while *Buddingtonite* shows the second lowest consistency in the comparison of these three pairs of images.

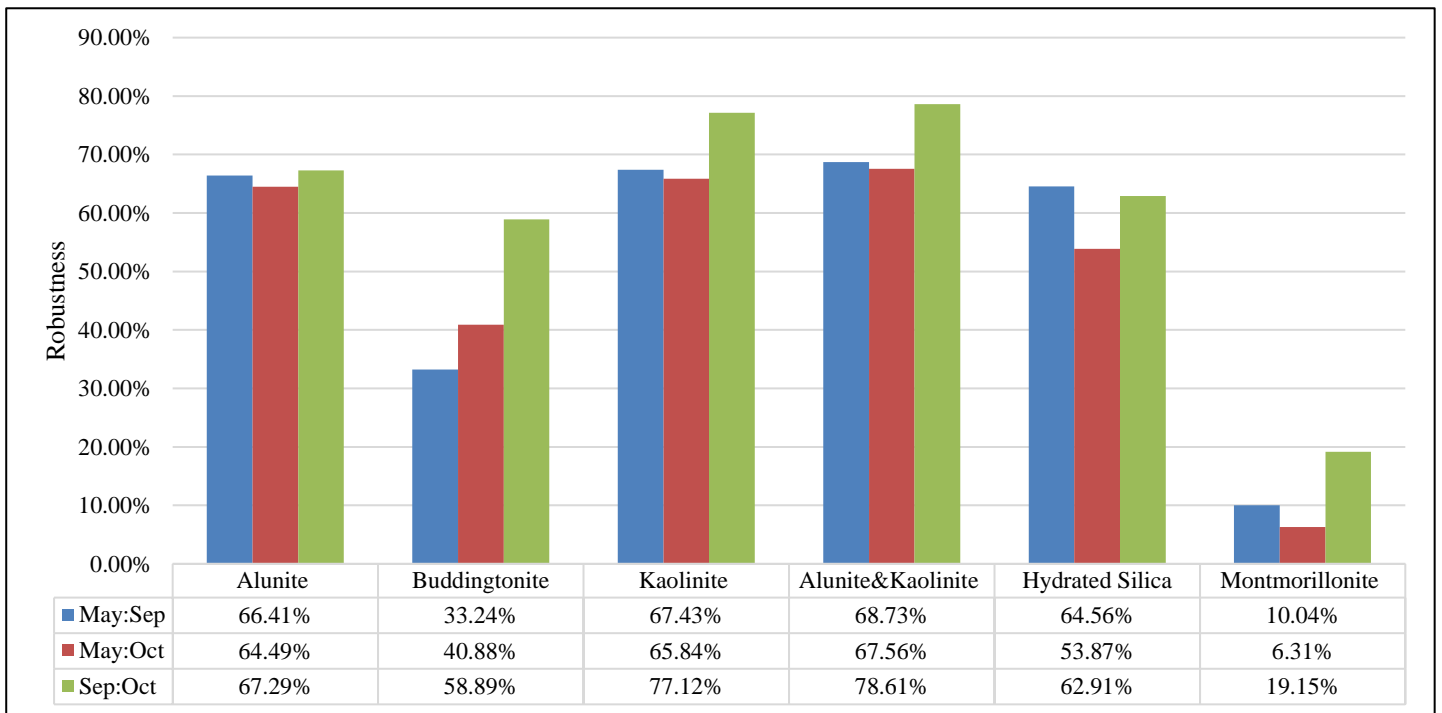


Figure 3.17 Reproducibility of solo maps classified with the universal endmember libraries

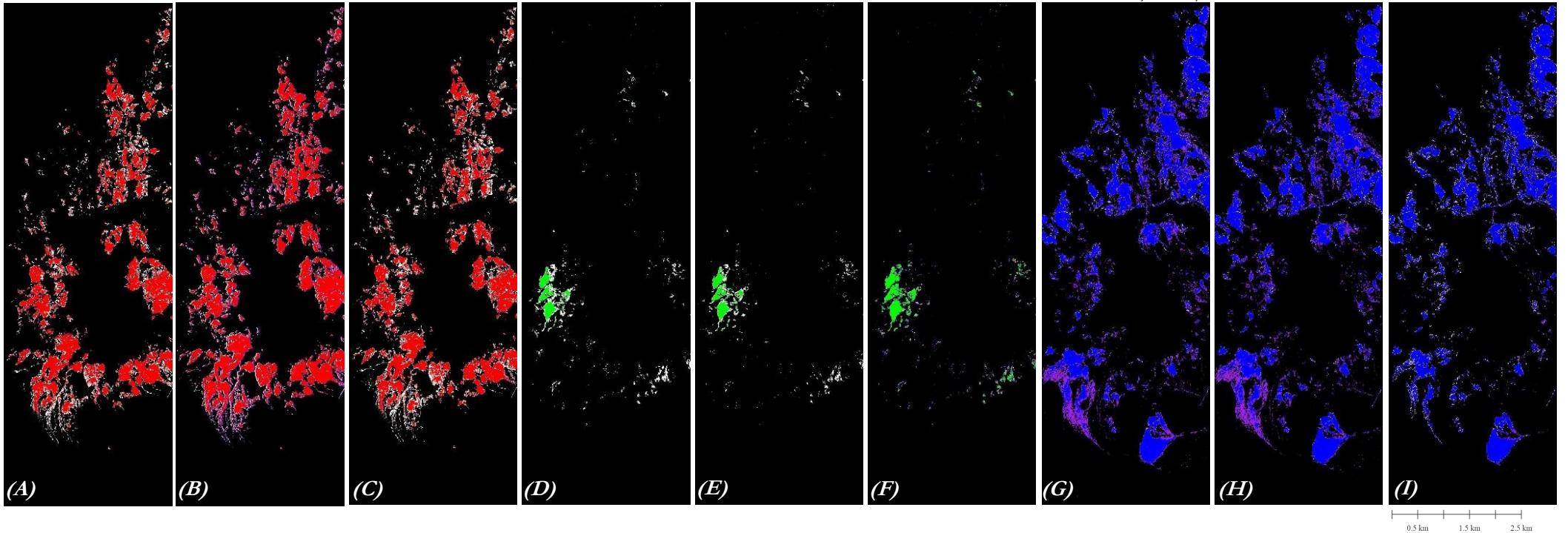


Figure 3.18 (A) show the different distribution of Alunite between reproduced mineral maps derived from May and Sep image; (B) show the different distribution of Alunite between reproduced mineral maps derived from May and Oct image; (C) show the different distribution of Alunite between reproduced mineral maps derived from Sep and Oct image; (D) show the different distribution of Buddingtonite between reproduced mineral maps derived from May and Sep image; (E) show the different distribution of Buddingtonite between reproduced mineral maps derived from May and Oct image; (F) show the different distribution of Buddingtonite between reproduced mineral maps derived from Sep and Oct image; (G) show the different distribution of Kaolinite between reproduced mineral maps derived from May and Sep image; (H) show the different distribution of Kaolinite between reproduced mineral maps derived from May and Oct image; (I) show the different distribution of Kaolinite between Sep and Oct image

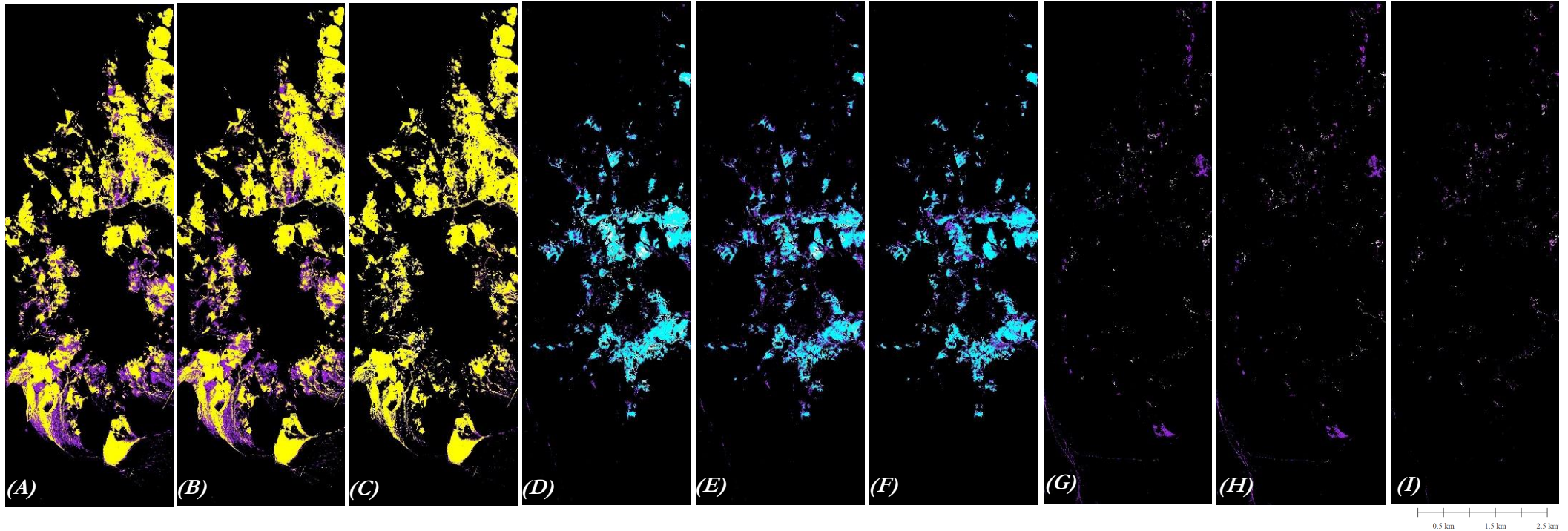


Figure 3.19 (A) show the different distribution of Alunite & Kaolinite between reproduced mineral maps derived from May and Sep image; (B) show the different distribution of Alunite & Kaolinite between reproduced mineral maps derived from May and Oct image; (C) show the different distribution of Alunite & Kaolinite between reproduced mineral maps derived from Sep and Oct image; (D) show the different distribution of Hydrated silica between reproduced mineral maps derived from May and Sep image; (E) show the different distribution of Hydrated silica between reproduced mineral maps derived from May and Oct image; (F) show the different distribution of Hydrated silica between reproduced mineral maps derived from Sep and Oct image; (G) show the different distribution of Montmorillonite between reproduced mineral maps derived from May and Sep image; (H) show the different distribution of Montmorillonite between reproduced mineral maps derived from May and Oct image; (I) show the different distribution of Montmorillonite between reproduced mineral maps derived from Sep and Oct image

3.8. Accuracy assessment

3.8.1. Comparison between the classification results and the Cuprite Mineral Map

Initially, a reclassified file derived from geo-coded the Cuprite Mineral Map (Swayze et al.2014) was generated through the unique value for each mineral mapped upon it in the green band as the ground truth. Then correctness of the reproduced mineral maps was estimated by the comparison between the classification results created by SAM and the ground truth through confusion matrix (shown in Table 3.12, Table 3.13, and Table 3.14). The overall accuracy of the classification result derived from the May image and classified by the various thresholds using the universal endmembers is around 64%. The overall accuracy of the classification result derived from the Sep image and classified by the various thresholds using the universal endmembers is around 63%. The overall accuracy of the classification result derived from the Oct image and classified by the various thresholds using the universal endmembers is around 64%.

Table 3.12 Confusion matrix of the comparison between the ground truth and May image

May Image	Ground Truth							Total	Error of Commission(%)	User Accuracy(%)
	Unclassified	Alunite	Buddingtonite	Kaolinite	Kaolinite & Alunite	Hydrated Silica	Montmorillonite			
Unclassified	531187	4161	951	35659	46791	5691	12595	637035	16.62	83.38%
Alunite	51880	5855	499	2690	19129	17	258	80328	92.71	7.29%
Buddingtonite	2588	235	804	86	98	0	4	3815	78.93	21.07%
Kaolinite	36380	379	93	46172	12655	125	491	96295	52.05	47.95%
Kaolinite & Alunite	27500	1267	157	12171	27947	70	284	69396	59.73	40.27%
Hydrated Silica	44432	604	39	2455	8829	7661	7054	71074	89.22	10.78%
Montmorillonite	3686	6	7	1453	613	0	24	5789	99.59	0.41%
Total	697653	12507	2550	100686	116062	13564	20710	963732		
Error of omission(%)	23.86%	53.19%	68.47%	54.14%	75.92%	43.52%	99.88%			
Producer Accuracy(%)	76.14%	46.81%	31.53%	45.86%	24.08%	56.48%	0.12%	Overall Accuracy = 64.3%		

Table 3.13 Confusion matrix of the comparison between the ground truth and Sep image

Sep Image	Ground Truth								Error of Commission(%)	User Accuracy(%)
	Unclassified	Alunite	Buddingtonite	Kaolinite	Kaolinite & Alunite	Hydrated Silica	Montmorillonite	Total		
Unclassified	539971	3491	911	39148	52781	4665	12902	653869	17.42	82.58%
Alunite	69207	7516	693	3870	34941	2	138	116367	93.54	6.46%
Buddingtonite	3858	295	834	377	483	0	4	5851	85.75	14.25%
Kaolinite	18514	143	42	36214	3433	26	146	58518	38.11	61.89%
Kaolinite & Alunite	20057	521	28	19790	16056	11	94	56557	71.61	28.39%
Hydrated Silica	40268	532	40	1072	8251	8858	7387	66408	86.66	13.34%
Montmorillonite	1103	4	2	215	117	2	15	1458	98.97	1.03%
Total	692978	12502	2550	100686	116062	13564	20686	959028		
Error of omission(%)	22.08	39.88	67.29	64.03	86.17	34.69	99.93			
Producer Accuracy(%)	77.92%	60.12%	32.71%	35.97%	13.83%	65.31%	0.07%	Overall Accuracy = 63.55%		

Table 3.14 Confusion matrix of the comparison between the ground truth and Oct image

Oct Image	Ground Truth								Error of Commission(%)	User Accuracy(%)
	Unclassified	Alunite	Buddingtonite	Kaolinite	Kaolinite & Alunite	Hydrated Silica	Montmorillonite	Total		
Unclassified	551466	3573	941	40107	54618	6722	14794	672221	17.96	82.04%
Alunite	70219	7597	673	Oct-11	35841	1	144	118792	93.6	6.40%
Buddingtonite	3506	253	812	349	438	0	3	5361	84.85	15.15%
Kaolinite	18303	129	45	34742	3288	20	158	56685	38.71	61.29%
Kaolinite & Alunite	20398	542	49	20368	15405	14	114	56890	72.92	27.08%
Hydrated Silica	28107	404	28	655	6352	6807	5449	47802	85.76	14.24%
Montmorillonite	979	4	2	148	120	0	24	1277	98.12	1.88%
Total	692978	12502	2550	100686	116062	13564	20686	959028		
Error of omission(%)	20.42	39.23	68.16	65.49	86.73	49.82	99.88			
Producer Accuracy(%)	79.58%	60.77%	31.84%	34.51%	13.27%	50.18%	0.12%	Overall Accuracy = 64.32%		

3.8.2. Comparison between the classification results and the wavelength map

The classification results with both the universal endmember library and the extracted endmember library are also assessed by making a comparison with the wavelength positions of the first peak produced by the software HypPy, through a box plot (shown in Figure 3.20). In these plots, the Y-axis shows the wavelength of the deepest absorption position of the spectral curve carried by a pixel in the hyperspectral images while X-axis shows the classes of the classification results. In conclusion, these plots present the wavelength position of the first peak for classified pixels. Thus, if the boxes shown in Figure 3.20 are concentrating to the wavelength of the absorption feature represents the mineral that box belongs to, then certain mineral is accurately identified.

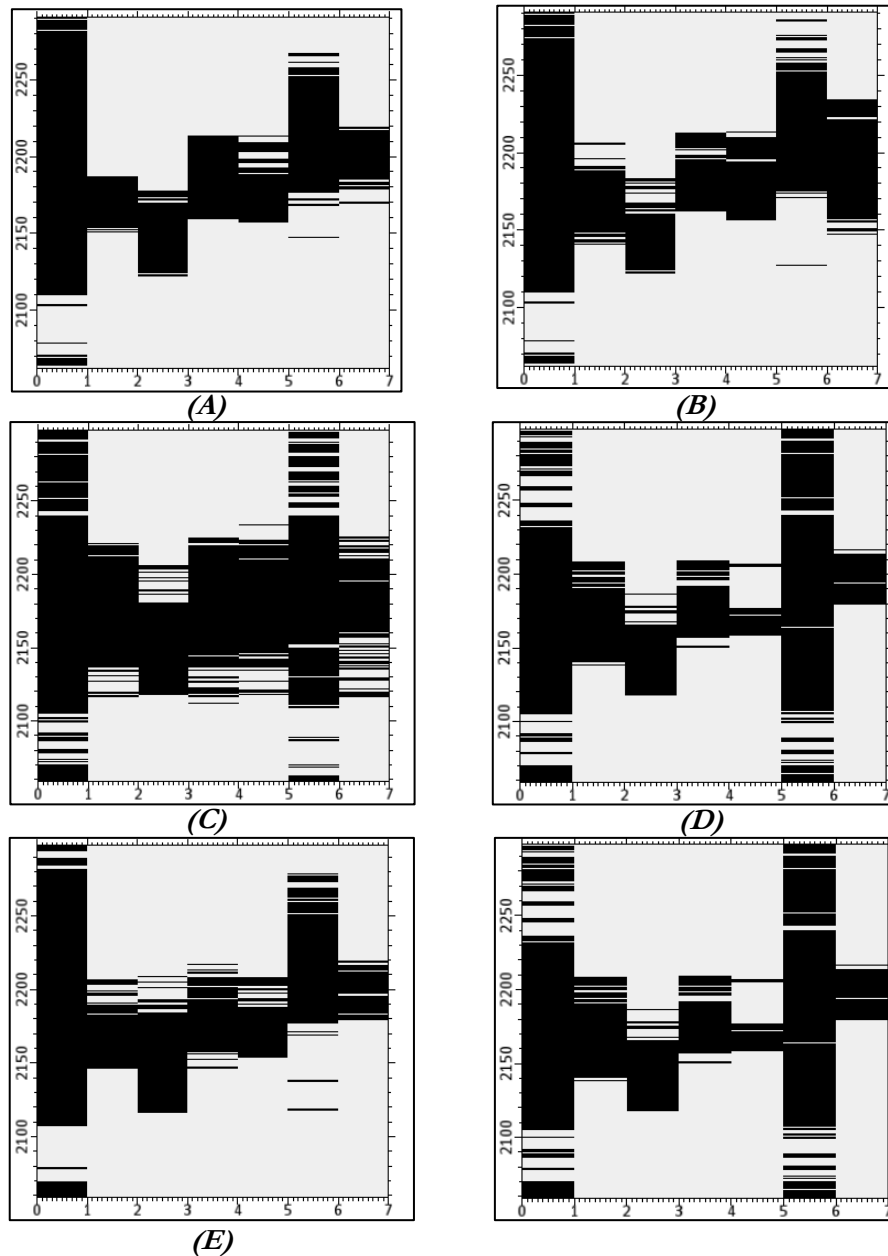


Figure 3.20 (A), (C), and (E) shows the comparison between the ground truth and the classification results created with the universal library through May, Sep, and Oct image respectively; (B), (D), and (F) presents the comparison between the ground truth and the classification results created with the customized library through May, Sep, and Oct image respectively. In the X-axis, 0 to 1 represents unclassified; 1 to 2 represents Alunite; 2 to 3 represents Buddingtonite; 3 to 4 represents Kaolinite; 4 to 5 represents Alunite & Kaolinite; 5 to 6 represents Hydrated silica; 6 to 7 represents Montmorillonite

Based on the observation of the results in Figure 3.20, the classification result of images that have been classified with the universal endmembers cover a large wavelength range. For each class, its corresponding box is not concentrating toward the wavelength that represents its deepest absorption feature.

3.9. The relationship between reproducibility and correctness

To verify the main-assumption that the measurement of reproducibility is the first step for the accuracy assessment without the ground truth data proposed at the beginning of this research. The reproducibility that measured in this research of the classified solo mineral maps that created with the SAM classifier and the universal endmember libraries derived from the May image, Sep image, and Oct image were compared with their producer accuracy (shown in Figure 3.21, 3.22, and 3.23). The producer accuracy was selected to compare because it is defined as the ratio that pixels in the test image labelled in the same class to the pixels in the same location of the reference image (Bakx et al., 2013), thus this ratio is more related to the processing of classification than the user accuracy or the overall accuracy.

Based on Figure 3.21, 3.22, and 3.23, the reproducibility of every single mineral shows similarity in trend with the producer accuracy of the corresponding mineral. Only the mixed mineral that *alunite & kaolinite* shows high differences in trend. Moreover, the mineral *montmorillonite* shows the lowest ratio for both the reproducibility and producer accuracy.

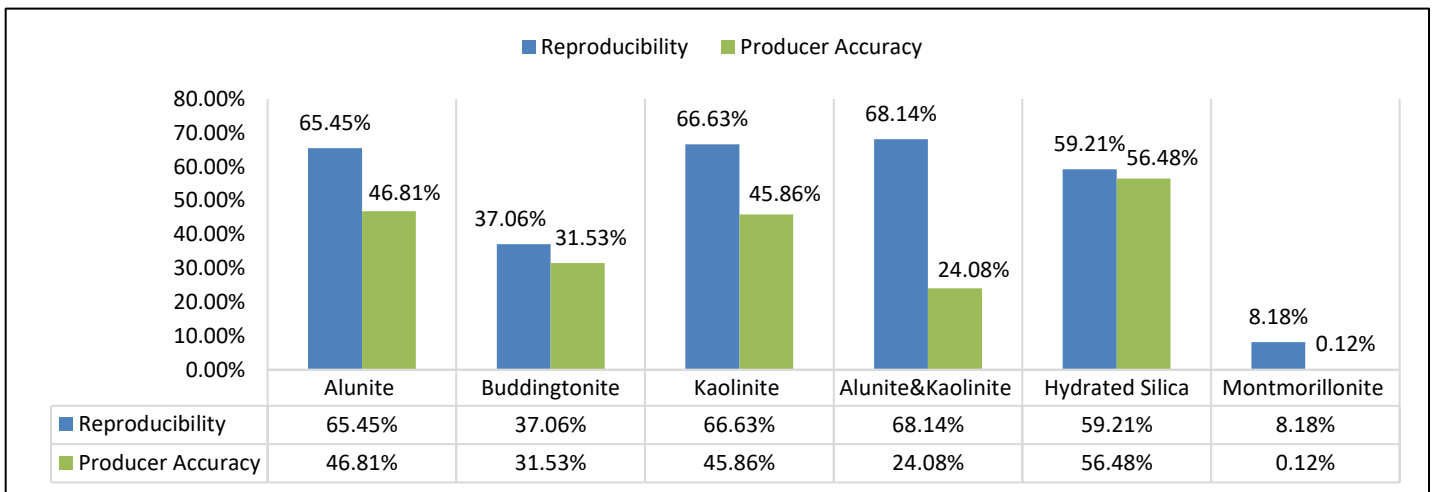


Figure 3.22 Comparison between reproducibility and producer accuracy of May image.

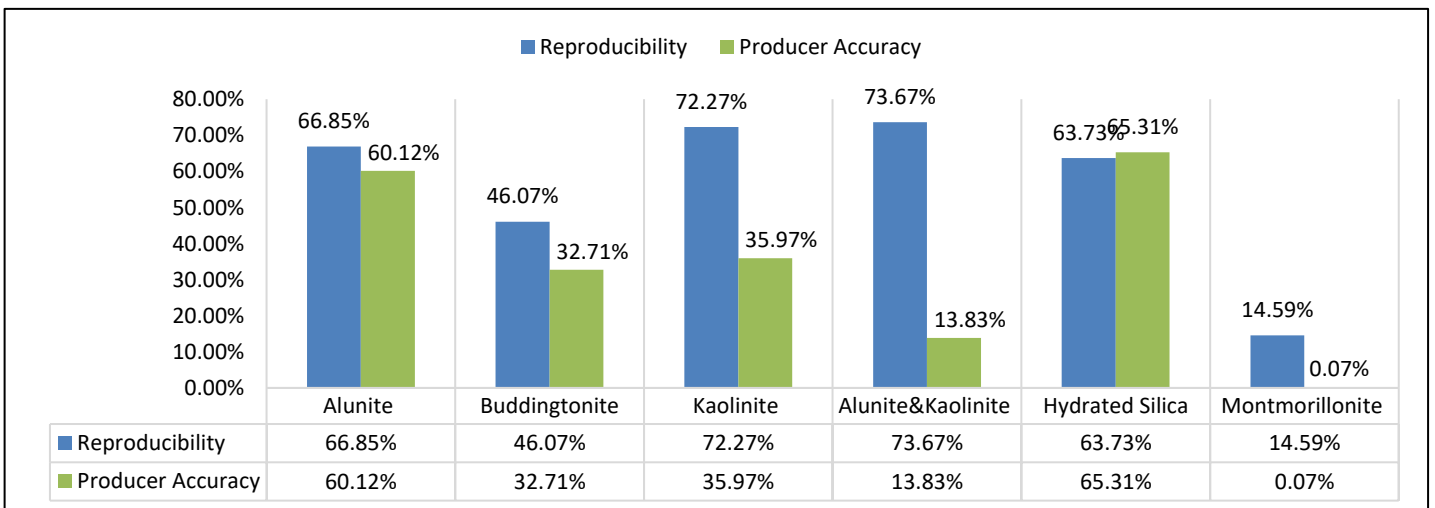


Figure 3.21 Comparison between reproducibility and producer accuracy of Sep image.

EVALUATING REPRODUCIBILITY AND ACCURACY OF HYPERSPECTRAL MINERAL MAPS USING MULTITEMPORAL AVIRIS IMAGES OF CUPRITE, NEVADA, USA

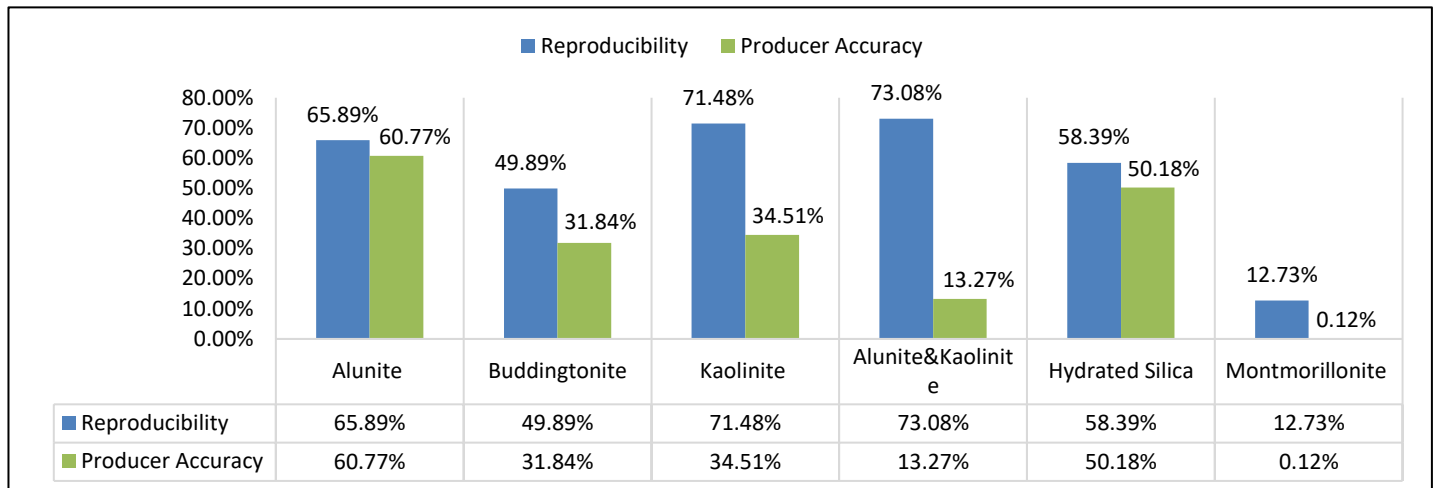


Figure 3.23 Comparison between reproducibility and producer accuracy of Oct image.

4. DISCUSSION

The inspection of the atmospheric correction shows that both the operation and the overall reflectance spectra indicate that the model was able to transfer the radiance at sensor data to surface reflectance image. It was observed that some bands in the atmospheric absorption wavelength (around 0.9 μm and 1.4 μm) were over-corrected by the FLAASH method (shown in Figure 3.1 A), but the spectral curve of the other wavelength range, like bands in wavelength range from 2.05 μm to 2.3 μm used in this research, was not influenced (shown in Figure 3.1 B). Furthermore, the ATM absorption curves around 2.0 and 2.45 μm disappeared after ATM correction (shown in Figure 3.1 B).

For assessing the quality of atmospheric correction, the endmembers manually extracted from three ATM corrected hyperspectral images and endmember of their corresponding minerals from the USGS library were compared. Figure 3.2 shows three sets of spectra which are comparison results between endmembers from the USGS library and spectra manually extracted from three ATM corrected hyperspectral images. In these comparison results, the extracted spectra present the same absorption features as its corresponding endmember from the USGS library. Therefore, the quality of atmospheric correction results in this research was decided to be acceptable because for the absorption feature of the same mineral of the image spectra and the USGS library spectra were similar.

Based on the Cuprite Mineral Map produced by Swayze et al (2014), the alteration minerals in this area are identified as *alunite*, *buddingtonite*, *kaolinite*, *alunite & kaolinite*, *hydrated silica*, and *montmorillonite*. None of these minerals has the first diagnostic spectral features of a wavelength range from 2420 nm to 2480 nm (Swayze et al., 2014). As well as the latter wavelength concentrating range is an atmospheric absorption range (van der Werff & van der Meer, 2015), thus the wavelength range 2120 nm to 2250 nm was considered as the concentrating range of the mineral spectral signatures. Therefore, during wavelength mapping, the wavelength range of the hyperspectral images used was further subsetted to 2050 nm to 2300 nm in this research. The range 2120 nm to 2250 nm contains the first absorption features while 2.05-2.12 μm and 2.25-2.3 μm were kept for the spectral shoulders of the targeting alteration minerals. Therefore, the wavelength range used in this research was further spectrally subsetted to 2048 nm to 2308 nm. This further subset was conducted to reduce the impact of other spectral curve features around the diagnostic absorption features of the hydrothermal alterative minerals in the study area.

To carry out mineral classification, two kinds of endmember libraries were created in this research (shown in Figure 3.6). The first type is three extracted spectral endmember libraries and they were directly extracted from each of the multitemporal hyperspectral images used in this research. However, the spectral endmembers that extracted from different images may have some slight differences which may enhance the uncertainty for the analysis of reproducibility amongst the classification results that created with those extracted endmembers. Therefore, a special kind of endmember library which is the universal spectral endmember library was also created in this research. For higher representability of endmember that used to classify all of the three multitemporal hyperspectral images, the universal endmember was designed as the average of endmembers of the corresponding mineral from the three extracted endmember libraries.

The correlation was used to evaluate the differences between spectral endmembers for the same mineral but extracted from different images. Furthermore, the extracted endmember and the universal endmember of the same mineral was also been evaluated for the similarity. Based on the results shown in Table 3.1 and Table 3.2, the correlation coefficient amongst each pair of the compared endmembers is over 0.95 and some of them are even equal to 1. This implies that the spectral endmembers of each of the extracted

endmember library or the universal endmember library representing the same mineral type but derived from different images are highly associated or totally same based on the criteria mentioned by Asuero et al. (2006). Therefore, differences caused by using those highly associated endmembers for classification will only slightly happen or not even happened. Thus, an assumption proposed in this research, that the reproducibility of classification may be disturbed by the differences of the extracted endmember that extracted from different hyperspectral images was theoretically disproved. Thus, extracted endmembers were firstly used for classification by the method SAM. Since, unlike the universal endmembers, they were not mixed by the process of averaging.

The self-assessment (see in Appendix III) of the GCPs that was used for the registration of images shows an RMS error as 0.508 m and 0.624 m for the accuracy of the aligning results of the May image and Sep image as well as May image and Oct image respectively (shown in Figure 3.7). These ratios, in the unit of meter (Barazzetti et al., 2016) present the shift amongst pixels with the same coordinates. Therefore, from each of the hyperspectral image scenes, the RMS error is much lower than the size of one pixel, as the pixel size of the hyperspectral images used for registration is 3.3 m. Otherwise, when the RMS error is larger than one ground sampling distance the alignment will be inaccurate (Barazzetti et al., 2016). Therefore, the spatial accuracy for image aligning was considered as acceptable for pixel-based comparison. Moreover, after the process of registration with these two portions of GCPs, the image-to-image registration results were assessed by the dynamic link through the visual inspection. And these registered results presented that they are as close as possible according to both the low RMS errors and the dynamic visual estimations. Therefore, for this research, the co-registered pixels while from different hyperspectral images are assumed as overlapping with the same coordinates.

Changes in mineral distribution as the time changes can be visually observed from mineral maps created by the extracted endmembers (shown in Figure 3.8). For more specific estimation, the reproducibility for the performance of the method SAM was measured through the confusion matrix (shown in Table 3.3, 3.4, and 3.5). The overall accuracy was assumed as the similarity between these two images since the overall accuracy was calculated based on the comparison of their classification results. The similarities calculated with the confusion matrix (shown in Tables 3.3, 3.4, and 3.5) show low values relative to the results produced with the universal endmembers. The comparison between the classification results derived from May image and Sep image is around 60%, overall similarities of the comparison between the classification results derived from May image and Oct image is around 61%, and overall similarities of the comparison between the classification results derived from Sep image and Oct image is around 58%. Therefore, both of the visual inspection and these low similarity ratios indicate the performance of the SAM classifier performed low reproducibility and/or consistency for the classifying of multitemporal images using the extracted endmembers and various threshold.

To further investigate the reason of low consistency and/or reproducibility between mineral maps derived from three multitemporal hyperspectral images and to enhance it, four reasons that may reduce the reproducibility of the SAM classification were assumed by this research. First, low consistency may be caused by the various threshold used for classification. Second, the differences between the original hyperspectral images used in this research may result in the low reproducibility. Third, the changes of vegetation with time series may be the reason. Last but not least, the spectral endmembers used for classification caused the low consistency even though they have already very similar according to the results of the spectral correlation. Thus, all of these four assumptions were investigated in this research for the enhancement of reproducibility and/or consistency.

Both the lower consistency and accuracy can be visually observed by the mineral maps (shown in Figure 3.9) created by the unique classification threshold. Therefore, the reproducibility of classifier SAM cannot be enhanced by using a unique classification threshold.

The different classification results following changes in time can be observed in Figure 3.12. Further analysis for those classification results by confusion matrix shows very high similarities. The overall accuracy from the confusion matrix (shown in Table 3.6, 3.7, and 3.8) between the classification results derived from May image and Sep image is around 82%, overall accuracy of the comparison between the classification results derived from May image and Oct image is around 93%, and overall accuracy of the comparison between the classification results derived from Sep image and Oct image is around 96%. The differences between visual inspection and overall accuracy may be caused by the overlap of some identified mineral types. On the other hand, the high accuracies (shown in Table 3.6, 3.7, and 3.8) may relate with the larger number of pixels that labelled as unclassified since the only pixel that has similar value was selected in former operation. Therefore, the calculation of identification similarity makes more sense since this calculation eliminates the influence of all the pixels that were labelled as unclassified.

The identification similarity (IdS) was measured to further verify the assumption that differences of the original hyperspectral images may affect the reproducibility. The IdS from the confusion matrix (shown in Table 3.6, 3.7, and 3.8) between the classification results derived from similarized May image and similarized Sep image is around 23%, IdS of the comparison between the classification results derived from similarized May image and similarized Oct image is around 50%, and IdS of the comparison between the classification results derived from similarized Sep image and similarized Oct image is around 47%. The IdS from the confusion matrix (shown in Table 3.6, 3.7, and 3.8) between the classification results derived from May image and Sep image is around 21%, IdS of the comparison between the classification results derived from May image and Oct image is around 24%, and IdS of the comparison between the classification results derived from similarized Sep image and similarized Oct image is around 22%. Thus, the identification similarity between the classification results that were derived from the original images is much lower ratios than the identification similarity between the classification results that were derived from the similarized images (shown in Figure 3.11). Therefore, the assumption that the low reproducibility may be caused by the differences of the original images was confirmed and the differences between the original images were considered as a main reason for the low reproducibility of classification for multitemporal hyperspectral images over the same area.

The statistical results (shown in Figure 3.14, 3.15, and 3.16) of the classified NDVI images (shown in Figure 3.13) present that vegetation was barely present in this region in any season. So that the vegetation condition was considered as cannot disturb the reproducibility of classification results and result in huge differences as shown in Figure 3.8.

The mineral maps created from the universal endmembers show high consistency as seen in Figure 3.17. Moreover, as the overall accuracy presents of the confusion matrix (shown in Table 3.6, Table 3.7, and Table 3.8) is considered as similarity, thus the similarity between May image and Sep image is around 84%, between May image and Sep image is around 83%, and between Sep image and Oct image is around 89%. Therefore, the assumption was confirmed by the fact that the similarity between each pair of the classification results that were created with the universal endmembers shows a much higher ratio than the similarity between mineral maps created using the extracted endmember libraries. Thus, another main factor that may disturb the reproducibility of SAM classifier to create mineral maps based on multi-temporal hyperspectral images was considered as the endmembers used.

The low reproducibility ratio of Buddingtonite was shown in Figure 3.18. This can be explained by the fact that only a few pixels were identified as *Buddingtonite*, therefore even a small number of the misclassified pixels can result in a relatively high influence for the reproducibility of this mineral. The lowest ratio of reproducibility was found in the mineral of *montmorillonite*. It may be caused by the fact mentioned before, that *montmorillonite* was classified by the most vague endmember. The endmember of *montmorillonite* even cannot be extracted by the algorithm SSEE in the May image and Oct image.

The geo-coded Cuprite Mineral Map (Swayze et al., 2014) was used as the ground truth data to estimate the accuracy of the reproduced mineral maps (shown in Figure 3.17) created in this research. This is because the producers have already validated the Cuprite Mineral Map and also this map was generated based on the AVIRIS data (Swayze et al., 2014). Therefore, as there is no field data collected in this research, the Cuprite Mineral Map that well-validated by the authors using both published information and the field data is the best independent ground truth data that can be used in this research.

The overall accuracies of the reproduced mineral maps are around 65% (shown in Table 3.9, 3.10, and 3.11). The relatively low overall accuracies maybe caused by the fact that pixels which are representing minerals were omitted during the transformation from the Cuprite Mineral Map to a classified image that can be compared by the confusion matrix. This is because, for the boundary of polygons in a vector image like the Cuprite Mineral Map, they will be gradually changed during the conversion from vector to raster. However, the value of these gradually changed pixels will be too complicated to select, thus the number of identified pixels was undercounted. Therefore, the real overall accuracy of the reproduced classification results could be higher than the ratios shown above.

Based on the observation of the box plots of wavelength position seen in Figure 3.20, the classification results, that the minerals classified with the universal endmember libraries or the universal endmembers are not very accurate. Because for each mineral class, its corresponding box is not concentrating toward the wavelength that represents its deepest absorption feature. However, the information of absorption depth which is related with the content of targets (van der Meer et al., 2012) has not been considered in the results of the box plots, and the number of pixels whose spectral curve has the disperse the first peak is not been shown either. Thus, this method could be a nice tool to assess the accuracy of the classification results without the need for in-situ measurement. It also offers a nice way to furtherly link the wavelength map and the classification results. But based on the drawbacks mentioned above, the box plot still needs more research to improve the information summarized by it.

The reproducibility and producer accuracy present highly associated values based on the observation of the results shown in Figure 3.21, Figure 3.22, and Figure 3.23, except the ratio of *Alunite & Kaolinite*. However, the Cuprite Mineral Map which was used as the ground truth in this research was produced by the classifier Tetracorder (Swayze et al. 2014) and the mineral maps generated in this research were classified by the method SAM. For, two different classifiers, it is too difficult to create similar results for a mixed class of two similar mineral type like *Alunite & Kaolinite*. Moreover, only this class shows low association and never shows high associations across all of these three comparisons. Therefore, the low correlation results of class *Alunite & Kaolinite* was considered as a result of the mixed endmember and different classifier in this research. In other word, the reproducibility and producer accuracy are highly correlated with each other based on all the analysis and results shown above.

5. CONCLUSION AND RECOMMENDATION

- In this research, the reproducibility of mineral maps that were derived from multitemporal hyperspectral images and classified with the universal spectral library by the SAM classifier shows a great potential to validate the classification result. Since the similar variation trend between the reproducibility for each mineral and the producer accuracy for the corresponding mineral. The use of reproducibility or robustness to estimate the accuracy of classification results does not rely on any ground truth data.
- The accuracies of mineral maps created in this research are acceptable based on the validation results that the overall accuracy for mineral maps derived from three multitemporal hyperspectral images are around 64%. And the real accuracy should higher than this ratio as some information was lost during the re-classification of the Cuprite Mineral Map.
- The use of “0.1” the default unique classification threshold of classifier SAM is not appropriate for the creation of both correct and consistent classification results. Since the results shown huge different amongst each other and each of the result shown huge differences from the ground truth map.
- The investigation of the similarity between the mineral maps that were derived from the similarized hyperspectral images shows that the difference between the original images is a factor contributing to the low reproducibility of the classification processing. Since huge differences amongst different original hyperspectral images and the higher identification similarity amongst the mineral maps derived from the similarized hyperspectral images.
- The evaluation for vegetation condition of the study area shows that only very sparse vegetation cover was detected, by the interpretation of NDVI results of Cuprite, from all of the three hyperspectral images. And this sparse vegetation cover does not show any relationship with the huge differences amongst mineral maps that derived from multitemporal hyperspectral images and classified by SAM with the extracted endmember libraries. On the other hand, the Cuprite was confirmed again as a good site for the research of remote sensing since it has sparse vegetation cover.
- The spectral correlation calculations present very high association between the extracted spectral endmember libraries that were directly extracted from each of the multitemporal hyperspectral images. However, the use of these three extracted spectral endmember libraries still showed a huge influence on the reproducibility of classification results. Therefore, based on the high similarity shown by the comparison between the classification results that were created using the universal endmember library. Mineral maps derived from multitemporal hyperspectral images can be robustly and/or reproducibly classified by the classifier SAM through the using of the universal spectral endmembers.

The recommendations of this research are shown below

- The change detection results show the differences amongst each of the three multitemporal hyperspectral images are similar to the shadow. The reproducibility of ortho-correction for radiance-at-sensor datasets should be further investigated.

- The box plot shows its great potential to assess the classification results by the comparison of these results with corresponding wavelength maps. However, the drawback of this method is that the information summarized by it is not enough to completely validate the classification results. of absorption depth which is related to the content of targets (van der Meer et al., 2012) to the box plot. Moreover, the number of pixels whose spectral curve have expanded wavelength distribution is not been summarized by the box plot either. Therefore, this research suggests further study to add these two types of information to the box plot. Then the box plot may become a powerful method for the accuracy assessment of classification results without the use of ground truth data.
- The accuracy for the conclusion of this research was built upon the pixel-by-pixel comparison between mineral maps created in this research and the Cuprite Mineral Map as ground truth data. However, some pixels were lost during the reclassification of the Cuprite Mineral Map. Therefore, for higher reliability, this research highly suggests further investigation to repeat the conclusion proposed in this research with in-situ measurement data and also repeat this research in other regions.

LIST OF REFERENCES

- Amera, S. A. (2007). *Spectral Remote Sensing of Hydrothermal Alteration associated with Volcanogenic Massive Sulphide Deposits, Gorob-Hope area, Namibia*. the International Institution fro Geo-information Science and Earth Observation, Enschede, the Netherlands.
- Aronoff, S. (1985). The Minimum Accuracy Value as an Index of Classification Accuracy. *Photogrammetric Engineering and Remote Sensing*, 51(1), 99–111.
- Asadzadeh, S., & de Souza Filho, C. R. (2016). A review on spectral processing methods for geological remote sensing. *International Journal of Applied Earth Observation and Geoinformation*, 47, 69–90. <https://doi.org/10.1016/j.jag.2015.12.004>
- Ashley, R. P., & Abrams, M. J. (1980). *Alteration Mapping Using Multispectral Image - Cuprite Mining District, Esmeralda County, Nevada*. U. S. Geological Survey Open-File Report.
- Asuero, A. G., Sayago, A., & González, A. G. (2006). The correlation coefficient: An overview. *Critical Reviews in Analytical Chemistry*, 36(1), 41–59. <https://doi.org/10.1080/10408340500526766>
- Bakker, W. (2018). HYPPY HYPERSPETRAL PYTHON. Retrieved from <https://blog.utwente.nl/bakker/hyppy/>
- Bakker, W., Bakx, W., Bijker, W., Grabmaier, K., Janssen, L., Horn, J., ... Woldai, T. (2013). Sensor. In D. R. Tobergte & S. Curtis (Eds.), *The core of GIScience: a process-based approach* (pp. 125–166). Enschede, the Netherlands: ITC, University of Twente.
- Bakker, W. H. (2012). HypPy User Manual. Retrieved from <http://www.itc.nl/personal/bakker/hyppy.html>
- Bakx, A., Janssen, L., & Schetselaar, E. (2013). Image analysis. In D. R. Tobergte & S. Curtis (Eds.), *The core of GIScience: a systems-based approach* (pp. 205–225). Enschede, the Netherlands.
- Barazzetti, L., Roncoroni, F., Brumana, R., & Previtali, M. (2016). Georeferencing accuracy analysis of a single worldview-3 image collected over milan. In *ISPRS - International Archives of the Photogrammetry, Remote Sensing and Spatial Information Sciences* (Vol. XLI-B1, pp. 429–434). Prague, Czech Republic. <https://doi.org/10.5194/isprsarchives-XLI-B1-429-2016>
- Bedini, E. (2009). Mapping lithology of the Sarfartoq carbonatite complex, southern West Greenland, using HyMap imaging spectrometer data. *Remote Sensing of Environment*, 113(6), 1208–1219. <https://doi.org/10.1016/j.rse.2009.02.007>
- Ben-Dor, E., Kindel, B., & Goetz, A. F. H. (2004). Quality assessment of several methods to recover surface reflectance using synthetic imaging spectroscopy data. *Remote Sensing of Environment*, 90(3), 389–404. <https://doi.org/10.1016/j.rse.2004.01.014>
- Berk, A., Bernstein, S., Robertson, C., & Acharya, K. (1998). MODTRAN Cloud and Multiple Scattering Upgrades with Application to AVIRIS. *Remote Sensing Environment*, 65(3), 367–375.
- Bertels, L., Deronde, B., Debruyne, W., & Provoost, S. (2005). Optimized Spectral Angle Mapper classification of spatially heterogeneous dynamic dune vegetation , a case study along the Belgian coastline Optimized Spectral Angle Mapper classification of spatially heterogeneous dynamic dune vegetation , a case study a. In *The 9th International Symposium on Physical Measurements and Signatures in Remote Sensing (ISPMRS)*. Beijing, China.
- Bhandari, A. K., Kumar, A., & Singh, G. K. (2012). Feature Extraction using Normalized Difference Vegetation Index (NDVI): A Case Study of Jabalpur City. *Procedia Technology*, 6, 612–621. <https://doi.org/10.1016/j.protcy.2012.10.074>
- Blue Marble Geographics. (n.d.). Global Mapper - All-in-one GIS Software. Retrieved from <https://www.bluemarblegeo.com/products/global-mapper.php>
- Boardman, J. W. (2007). *New Aviris Orthorectification Processing And Products*. Retrieved from https://aviris.jpl.nasa.gov/data/data_process_resources.html
- Boubanga-tombet, S., Huot, A., Vitins, I., Heuberger, S., & Chamberland, M. (2018). Thermal Infrared Hyperspectral Imaging for Mineralogy Mapping of a Mine Face. *Remote Sensing*, 10(10), 1518. <https://doi.org/10.3390/rs10101518>
- Cheng, W. C., Chang, J. C., Chang, C. P., Su, Y., & Tu, T. M. (2008). A Fixed-Threshold Approach to Generate High-Resolution Vegetation Maps for IKONOS Imagery. *Sensors*, 8(7), 4308–4317. <https://doi.org/10.3390/s8074308>
- Congalton, R. . (1991). A Review of Assessing the Accuracy of Classifications of Remotely Sensed Data. *Remote Sensing of Environment*, 37(3), 35–46. <https://doi.org/10.5698/1535-7511-16.3.198>
- Congalton, R. G., & Green, K. (1999a). *Assessing the Accuracy of Remotely Sensed Data: Principles and Practices*. U. S: Lewis Publishers.

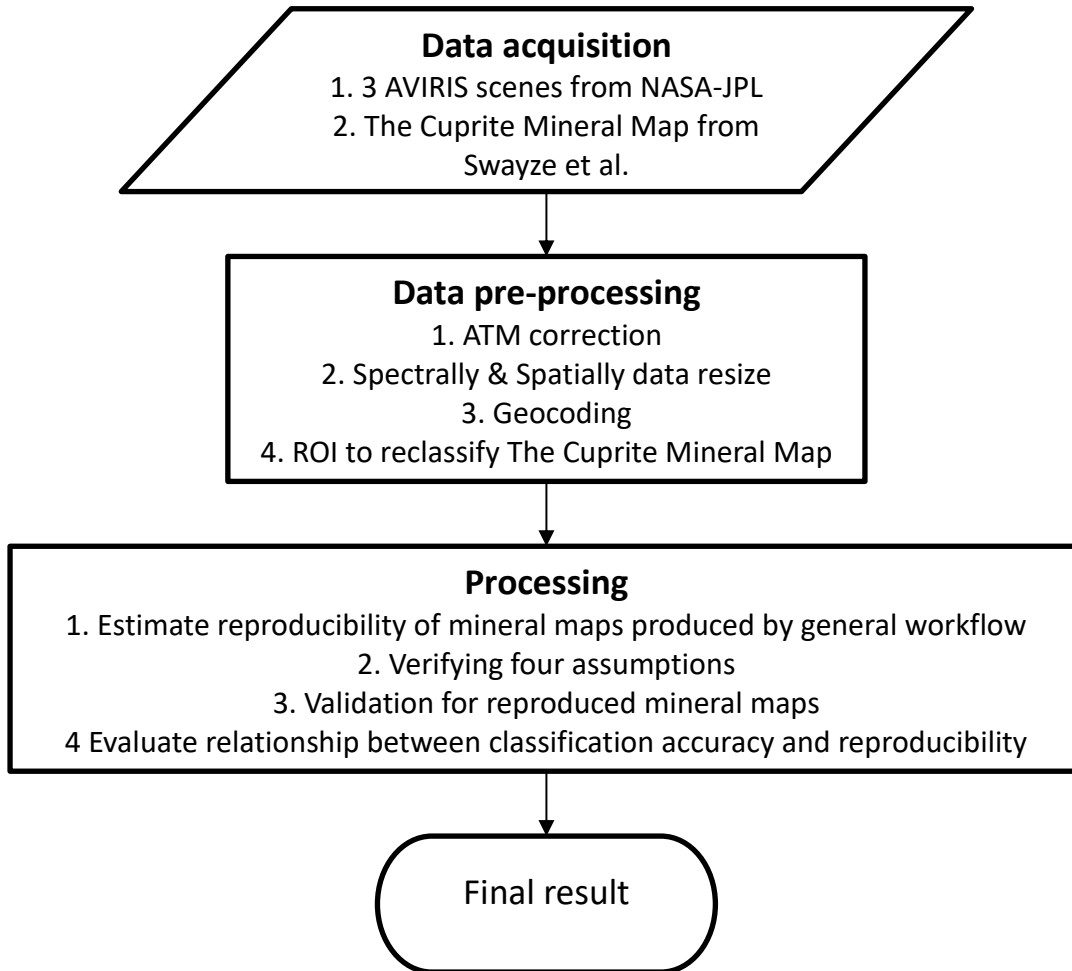
- Congalton, R. G., & Green, K. (1999b). Introduction. In *Assessing the Accuracy of Remotely Sensed Data: Principles and Practices* (pp. 8–12). U. S: Lewis Publishers.
- Congalton, R. G., & Green, K. (1999c). Overview. In *Assessing the Accuracy of Remotely Sensed Data: Principles and Practices* (pp. 13–16). U. S: Lewis Publishers.
- Duke, E. F. (1994). Near infrared spectra of muscovite, Tschermak substitution, and metamorphic reaction progress: Implications for remote sensing. *Geology*, 22(7), 621–624. [https://doi.org/10.1130/0091-7613\(1994\)022<0621:NISOMT>2.3.CO;2](https://doi.org/10.1130/0091-7613(1994)022<0621:NISOMT>2.3.CO;2)
- El_Rahman, S. A. (2016). Performance of Spectral Angle Mapper and Parallelepiped Classifiers in Agriculture Hyperspectral Image. *International Journal of Advanced Computer Science and Applications*, 7(5), 55–63. Retrieved from www.ijacsa.thesai.org
- Footy, G. (2008). Harshness in image classification accuracy assessment. *International Journal of Remote Sensing*, 29(11), 3137–3158. <https://doi.org/10.1080/01431160701442120>
- Footy, G. M. (2004). Thematic map comparison: evaluating the statistical significance of differences in classification accuracy. *Photogrammetric Engineering & Remote Sensing*, 70(5), 627–633. [https://doi.org/0099-1112/04/7005-0627/\\$3.00/0](https://doi.org/0099-1112/04/7005-0627/$3.00/0)
- Gandhi, G. M., Parthiban, S., Thummalu, N., & Christy, A. (2015). Ndvi: Vegetation Change Detection Using Remote Sensing and Gis - A Case Study of Vellore District. *Procedia Computer Science*, 57, 1199–1210. <https://doi.org/10.1016/j.procs.2015.07.415>
- Gao, B. (2018). *Quantitative Improvement to the Estimation of NDVI Values From AVIRIS Data By Correcting Thin Cirrus Scattering Effects*.
- Ginevan, M. E. (1979). Testing land-use map accuracy: another look. *Photogrammetric Engineering and Remote Sensing*, 45(10), 1371–1377.
- Gogtay, N. J., & Thatte, U. M. (2017). Statistics for researchers principles of correlation analysis. *Journal of The Association of Physicians of India*, 65(March), 78–81.
- Graham, G. E., Kokaly, R. F., Kelley, K. D., Hoefen, T. M., Johnson, M. R., Hubbard, B. E., & Al, G. E. T. (2018). Application of Imaging Spectroscopy for Mineral Exploration in Alaska: A Study over Porphyry Cu Deposits in the Eastern Alaska Range. *Economic Geology*, 113(2), 489–510. <https://doi.org/10.5382/econgeo.2018.4559>
- Harris Geospatial Solution Inc. (2018a). Automatic Image to Image Registration Tutorial. Retrieved from <https://www.harrisgeospatial.com/docs/RegistrationImageToImage.html>
- Harris Geospatial Solution Inc. (2018b). Create ROIs from Geometry, 1–11. Retrieved from <https://www.harrisgeospatial.com/docs/RegionOfInterestTool.html#ROIGeometry>
- Harris Geospatial Solution Inc. (2018c). ENVI Atmospheric Correction Module: QUAC and FLAASH user's guide. Retrieved from <http://scholar.google.com/scholar?hl=en&btnG=Search&q=intitle:ENVI+Atmospheric+Correction+Module:+QUAC+and+FLAASH+user's+guide#0>
- Harris Geospatial Solution Inc. (2018d). Mask. Retrieved from <https://www.harrisgeospatial.com/docs/masks.html>
- Harris Geospatial Solution Inc. (2018e). *Spatial Subset*. Retrieved from <https://www.harrisgeospatial.com/docs/subsetting.html>
- Harris Geospatial Solution Inc. (2018). Change Detection Difference Map. Retrieved from <https://www.harrisgeospatial.com/docs/ChangeDetectionAnalysis.html>
- Harris Geospatial Solutions. (2018). ENVI - The Leading Geospatial Analytics Software | Harris Geospatial. Retrieved from <https://www.harrisgeospatial.com/Software-Technology/ENVI>
- Hord, R. M., & Brooner, W. (1976). Land-use map accuracy criteria. *Photogrammetric Engineering and Remote Sensing*, 42(5), 671–677
- Hunt, G. R. (1977). SPECTRAL SIGNATURES OF PARTICULATE MINERALS IN THE VISIBLE AND NEAR INFRARED. *GEOPHYSICS*, 42(3), 501–513. <https://doi.org/10.1190/1.1440721>
- Jin, X. (2018). *ENVI Automated Image Registration Whitepapers*. Retrieved from https://www.harrisgeospatial.com/portals/0/pdfs/ENVI_Image_Registration_Whitepaper.pdf
- Kale, K. V., Solankar, M. M., Nalawade, D. B., Dhumal, R. K., & Gite, H. R. (2017). A Research Review on Hyperspectral Data Processing and Analysis Algorithms. *Proceedings of the National Academy of Sciences India Section A - Physical Sciences*, 87(4), 541–555. <https://doi.org/10.1007/s40010-017-0433-y>
- Kayet, N., Pathak, K., Chakrabarty, A., & Sahoo, S. (2018). Mapping the distribution of iron ore minerals and spatial correlation with environmental variables in hilltop mining areas. *Environmental Earth Sciences*, 77(8), 1–14. <https://doi.org/10.1007/s12665-018-7482-7>
- Kruse, F. A., & Boardman, W. (1990). Mineral Mapping at Cuprite, Nevada with a 63-Channel Imaging Spectrometer. *Photogrammetric Engineering & Remote Sensing*, 56(1), 83–92. Retrieved from

- Kruse, F. A., Lefkoff, A. B., Boardman, J. W., Heidebrecht, K. B., Shapiro, A. T., Barloon, P. J., & Goetz, A. F. H. (1993). The spectral image processing system (SIPS)—interactive visualization and analysis of imaging spectrometer data. *Remote Sensing of Environment*, 44(2–3), 145–163. [https://doi.org/10.1016/0034-4257\(93\)90013-N](https://doi.org/10.1016/0034-4257(93)90013-N)
- Kruse. (2004). Comparison of ATREM, ACORN, and FLAASH atmospheric corrections using low-altitude AVIRIS data of Boulder, Co. In *In Proceedings of the Summaries of 13th JPL Airborne Geoscience Workshop*. Pasadena, CA, U.S.
- Lu, D., Moran, E., Hetrick, S., & Li, G. (2009). Land-Use and Land-Cover Change Detection. In Q. Weng (Ed.), *Advances in Environmental Remote Sensing* (pp. 273–288). Boca Raton, FL, USA: Taylor & Francis.
- Mielke, C., Rogass, C., Boesche, N., Segl, K., & Altenberger, U. (2016). EnGeoMAP 2.0—automated hyperspectral mineral identification for the German EnMAP space mission. *Remote Sensing*, 8(2). <https://doi.org/10.3390/rs8020127>
- NASA-JPL. (2010). AVIRIS Distribution Document. Retrieved from https://aviris.jpl.nasa.gov/documents/100625_ortho.readme
- Pan, Z., Liu, J., Ma, L., Chen, F., Zhu, G., & Qin, F. (2019). Research on Hyperspectral Identification of Altered Minerals in Yemaquan West Gold Field, Xinjiang. *Sustainability*, 11(2). <https://doi.org/10.3390/su11020428>
- Perkins, T., Adler-Golden, S., Matthew, M., Berk, A., Anderson, G., Gardner, J., & Felde, G. (2005). Retrieval of atmospheric properties from hyper and multispectral imagery with the FLAASH atmospheric correction algorithm. In *In remote sensing of clouds and the atmosphere X. Proceedings of SPIE* (Vol. 5979, p. 11). Bruges, Belgium. <https://doi.org/10.1117/12.626526>
- Pontius, R. G., & Millones, M. (2011). Death to Kappa: Birth of quantity disagreement and allocation disagreement for accuracy assessment. *International Journal of Remote Sensing*, 32(15), 4407–4429. <https://doi.org/10.1080/01431161.2011.552923>
- Rajendran, S., & Nasir, S. (2018). ASTER capability in mapping of mineral resources of arid region: A review on mapping of mineral resources of the Sultanate of Oman. *Ore Geology Reviews*, (April), 0–1. <https://doi.org/10.1016/j.oregeorev.2018.04.014>
- Rani, N., Mandla, V. R., & Singh, T. (2017). Spatial distribution of altered minerals in the Gadag Schist Belt (GSB) of Karnataka, Southern India using hyperspectral remote sensing data. *Geocarto International*, 32(3), 225–237. <https://doi.org/10.1080/10106049.2015.1132484>
- Rani, N., Mandla, V. R., & Tejpal, S. (2017). Evaluation of atmospheric corrections on hyperspectral data with special reference to mineral mapping. *Geoscience Frontiers*, 8(4), 797–808. <https://doi.org/10.1016/j.gsf.2016.06.004>
- Rogge, D., Bachmann, M., Rivard, B., & Feng, J. (2012). Spatial sub-sampling using local endmembers for adapting OSP and SSEE for large-scale hyperspectral surveys. *IEEE Journal of Selected Topics in Applied Earth Observations and Remote Sensing*, 5(1), 183–195. <https://doi.org/10.1109/JSTARS.2011.2168513>
- Rogge, D. M., Rivard, B., Zhang, J., Sanchez, A., Harris, J., & Feng, J. (2007). Integration of spatial-spectral information for the improved extraction of endmembers. *Remote Sensing of Environment*, 110(3), 287–303. <https://doi.org/10.1016/j.rse.2007.02.019>
- Rosenfeld, G. H. (1982). Sample design for estimating change in land use and land cover. *Photogrammetric Engineering and Remote Sensing*, 48(5), 793–801.
- Rouse, J. W., Hass, R. H., Schell, J. A., & Deering, D. W. (1973). Monitoring Vegetation Systems in the Great Plains with ERTS. In *Third Earth Resources Technology Satellite-1 Symposium*.
- Schowengerdt, R. A. (2007). Correction and Calibration. In R. A. Schowengerdt (Ed.), *Remote Sensing: Models and Methods for Image Processing* (Third, pp. 285–354). San Diego, CA, USA: Elsevier. <https://doi.org/10.1016/B978-012369407-2/50010-3>
- Swayze, G. A., Clark, R. N., Goetz, A. F. H., Livo, K. E., Breit, G. N., Kruse, F. A., ... Ashley, R. P. (2014). Mapping Advanced Argillic Alteration at Cuprite, Nevada, Using Imaging Spectroscopy. *Economic Geology*, 109(5), 1179–1221. <https://doi.org/10.2113/econgeo.109.5.1179>
- Tobergte, D. R., & Curtis, S. (2013). Glossary. In D. R. Tobergte & S. Curtis (Eds.), *The core of GIScience: a process-based approach* (pp. 491–519). Enschede, the Netherlands: ITC, University of Twente.
- Usman, M. S. (2018). *Evaluating ASTER and WorldView-3 mineral mapping capabilities in an epithermal alteration system*. ITC, University of Twente.
- Van der Meer, F. (1995). Spectral reflectance of carbonate mineral mixtures and bidirectional reflectance theory: Quantitative analysis techniques for application in remote sensing. *Remote Sensing Reviews*, 13(1–2), 67–94. <https://doi.org/10.1080/02757259509532297>

- van der Meer, F. D., van der Werff, H. M. A., van Ruitenbeek, F. J. A., Hecker, C. A., Bakker, W. H., Noomen, M. F., ... Woldai, T. (2012). Multi- and hyperspectral geologic remote sensing: A review. *International Journal of Applied Earth Observation and Geoinformation*, *14*(1), 112–128. <https://doi.org/10.1016/j.jag.2011.08.002>
- van der Werff, H., & van der Meer, F. (2015). Sentinel-2 for mapping iron absorption feature parameters. *Remote Sensing*, *7*(10), 12635–12653. <https://doi.org/10.3390/rs71012635>
- Van Genderen, J., & Lock, B. (1977). Testing land use map accuracy. *Photogrammetric Engineering and Remote Sensing*, *43*, 1135–1137.
- Van Ruitenbeek, F. J. A., Bakker, W. H., Van Der Werff, H. M. A., Zegers, T. E., Oosthoek, J. H. P., Omer, Z. A., ... Van Der Meer, F. D. (2014). Mapping the wavelength position of deepest absorption features to explore mineral diversity in hyperspectral images. *Planetary and Space Science*, *101*, 108–117. <https://doi.org/10.1016/j.pss.2014.06.009>
- Wei, J., Ming, Y., Jia, Q., & Yang, D. (2017). Simple mineral mapping algorithm based on multitype spectral diagnostic absorption features: a case study at Cuprite, Nevada. *Journal of Applied Remote Sensing*, *11*(2), 026015. <https://doi.org/10.1117/1.JRS.11.026015>
- Weier, J., & Herring, D. (2000). MEASURING VEGETATION (NDVI&EVI). Retrieved from <https://earthobservatory.nasa.gov/features/MeasuringVegetation>
- Zhou, Q., Jing, Z., & Jiang, S. (2003). Remote sensing image fusion for different spectral and spatial resolutions with bilinear resampling wavelet transform. *IEEE Conference on Intelligent Transportation Systems, Proceedings, ITSC*, *2*, 1206–1213. <https://doi.org/10.1109/ITSC.2003.1252676>

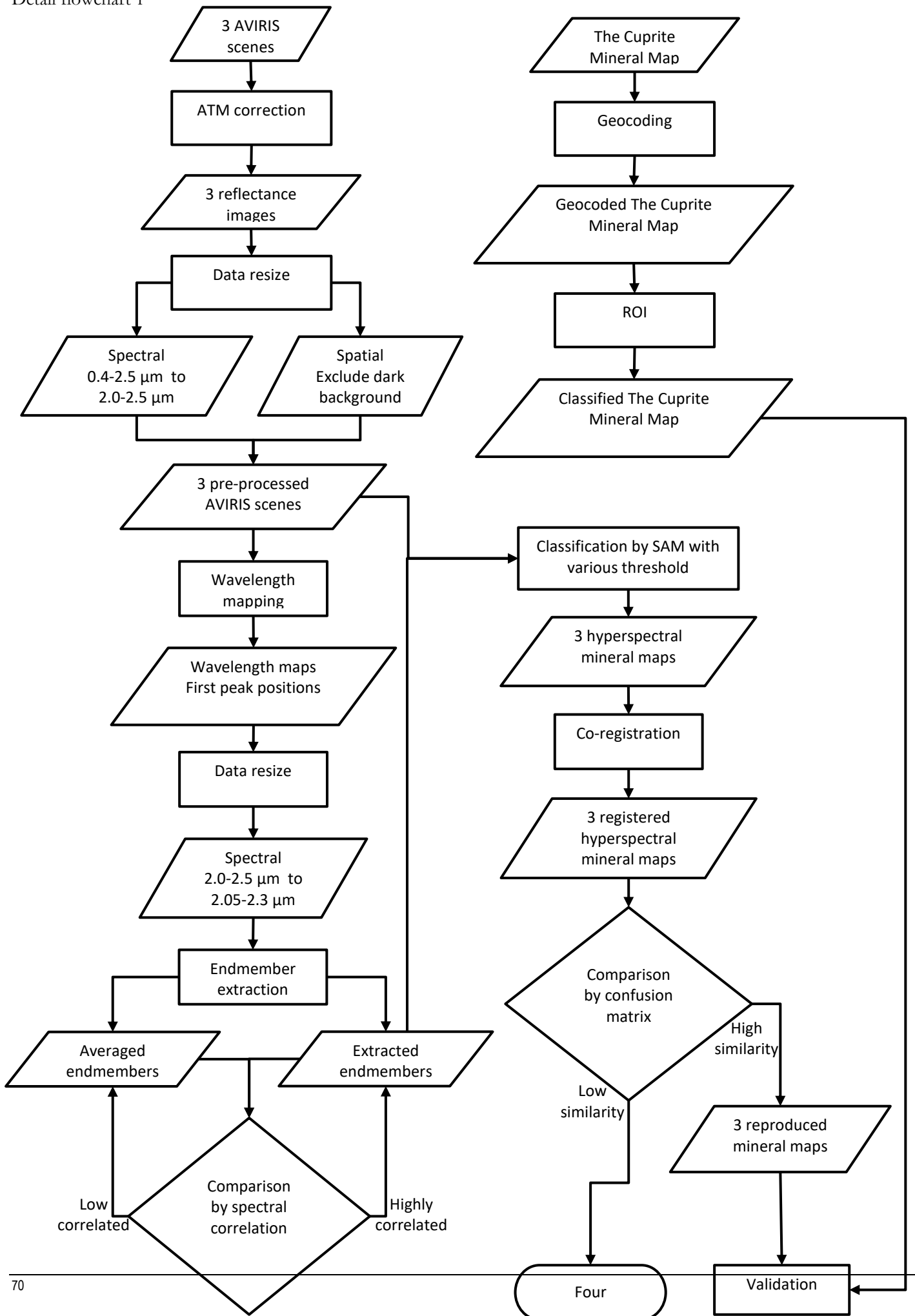
6. APPENDICES

Appendix I. Flowcharts illustrating methodology

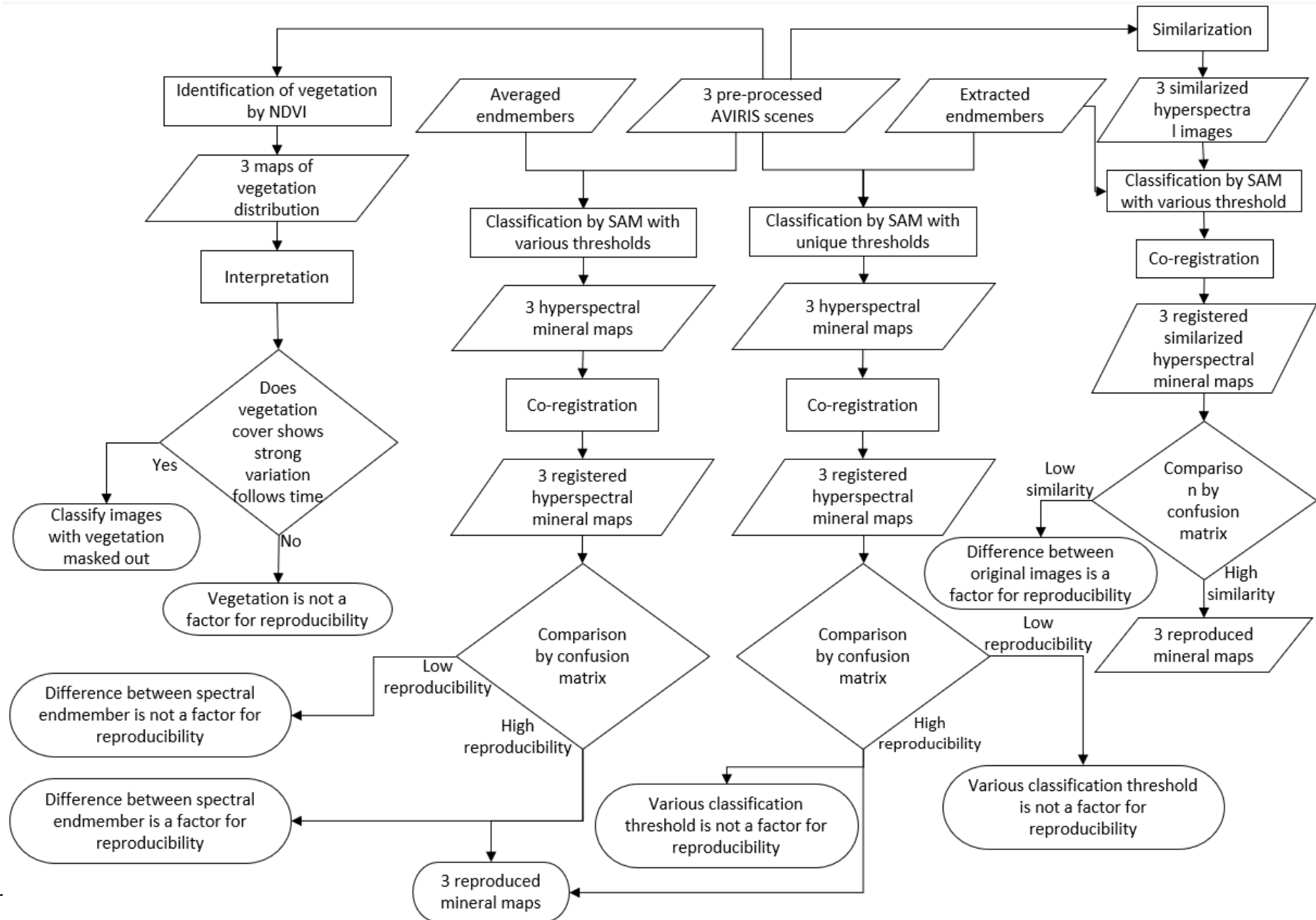


Above is the flow chat for general information. The following detail flowchart 1 presents the pre-processing and the processing of estimation for reproducibility of mineral maps produced by general workflow. Detail flowchart 2 shows the verifying for four assumptions. Detail flowchart 3 presents the validation of reproduced mineral maps and the evaluation of the relationship between classification accuracy and reproducibility.

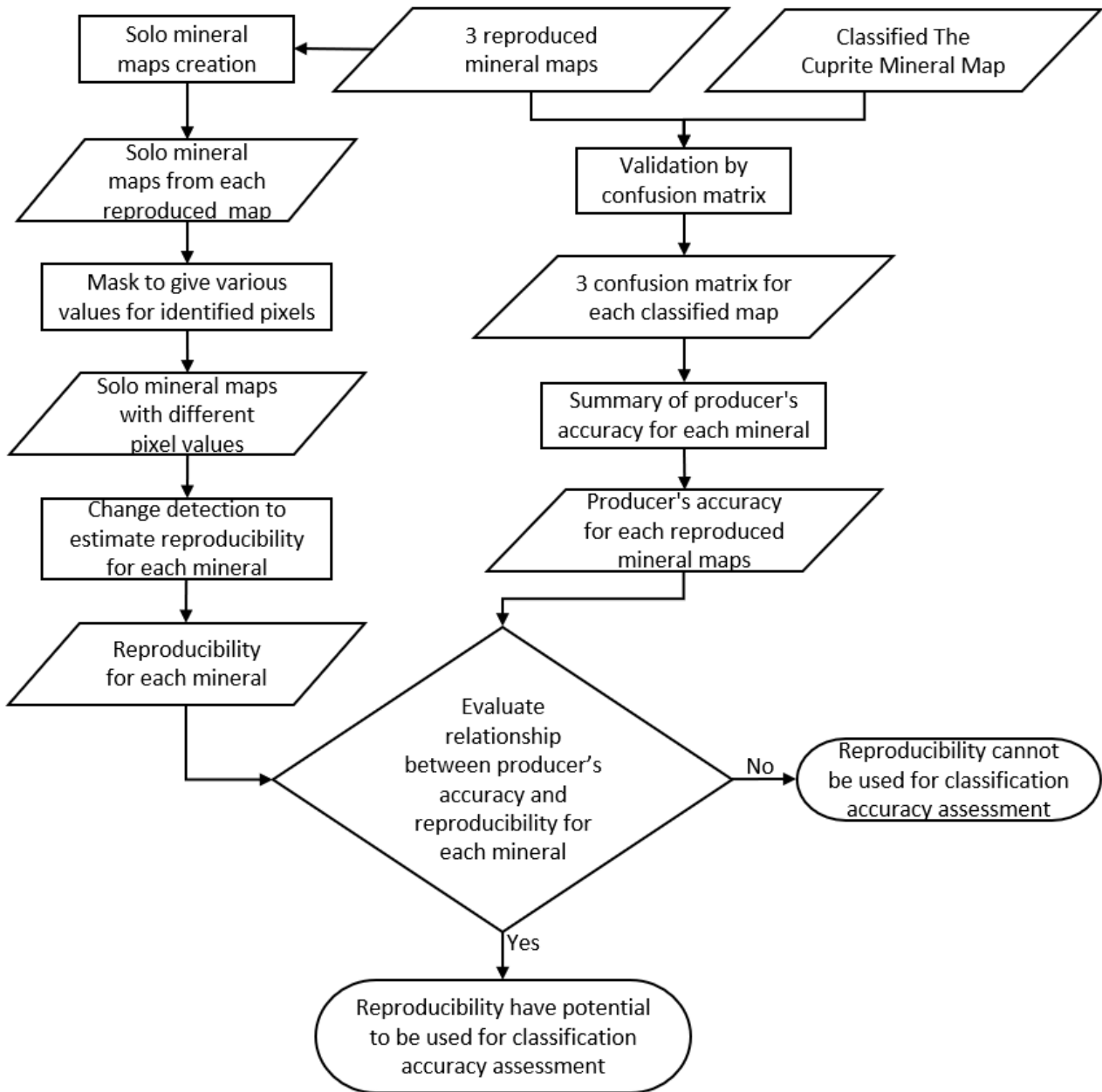
Detail flowchart 1



Detail flowchart 2









Detail flowchart 3



Appendix II. Two sets of thresholds for SAM







Classify by

Rule Image Parameters:

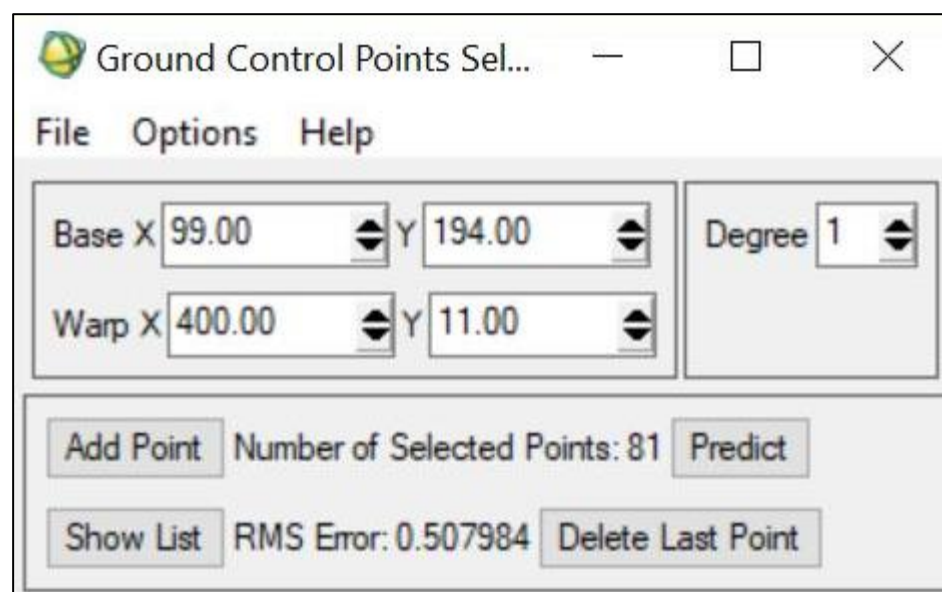
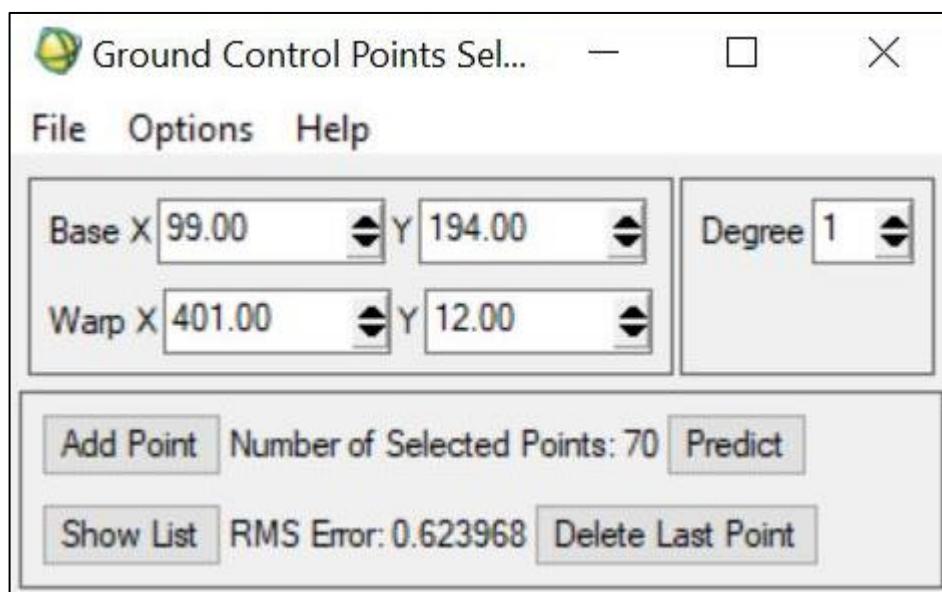
<input checked="" type="checkbox"/> On		<input type="text" value="Rule (Alunite060502)"/>	Thresh: <input type="text" value="0.08"/>	<input type="button" value="Hist"/>
<input checked="" type="checkbox"/> On		<input type="text" value="Rule (Buddingtonite060502)"/>	Thresh: <input type="text" value="0.0900"/>	<input type="button" value="Hist"/>
<input checked="" type="checkbox"/> On		<input type="text" value="Rule (Kaolinite060502)"/>	Thresh: <input type="text" value="0.1100"/>	<input type="button" value="Hist"/>
<input checked="" type="checkbox"/> On		<input type="text" value="Rule (Kaolinite+Alunite060502)"/>	Thresh: <input type="text" value="0.1100"/>	<input type="button" value="Hist"/>
<input checked="" type="checkbox"/> On		<input type="text" value="Rule (Hydrated_silica(chalcedony and/or opa)"/>	Thresh: <input type="text" value="0.03500"/>	<input type="button" value="Hist"/>
<input checked="" type="checkbox"/> On		<input type="text" value="Rule (Montmorillonite060502)"/>	Thresh: <input type="text" value="0.0200"/>	<input type="button" value="Hist"/>

Classify by

Rule Image Parameters:

<input checked="" type="checkbox"/> On		<input type="text" value="Rule (Alunite101014)"/>	Thresh: <input type="text" value="0.100"/>	<input type="button" value="Hist"/>
<input checked="" type="checkbox"/> On		<input type="text" value="Rule (Buddingtonite101014)"/>	Thresh: <input type="text" value="0.100"/>	<input type="button" value="Hist"/>
<input checked="" type="checkbox"/> On		<input type="text" value="Rule (Kaolinite101014)"/>	Thresh: <input type="text" value="0.100"/>	<input type="button" value="Hist"/>
<input checked="" type="checkbox"/> On		<input type="text" value="Rule (Alunite+Kaolinite 101014)"/>	Thresh: <input type="text" value="0.100"/>	<input type="button" value="Hist"/>
<input checked="" type="checkbox"/> On		<input type="text" value="Rule (Hydrated silica 101014)"/>	Thresh: <input type="text" value="0.100"/>	<input type="button" value="Hist"/>
<input checked="" type="checkbox"/> On		<input type="text" value="Rule (Montmorillonite 101014)"/>	Thresh: <input type="text" value="0.100"/>	<input type="button" value="Hist"/>

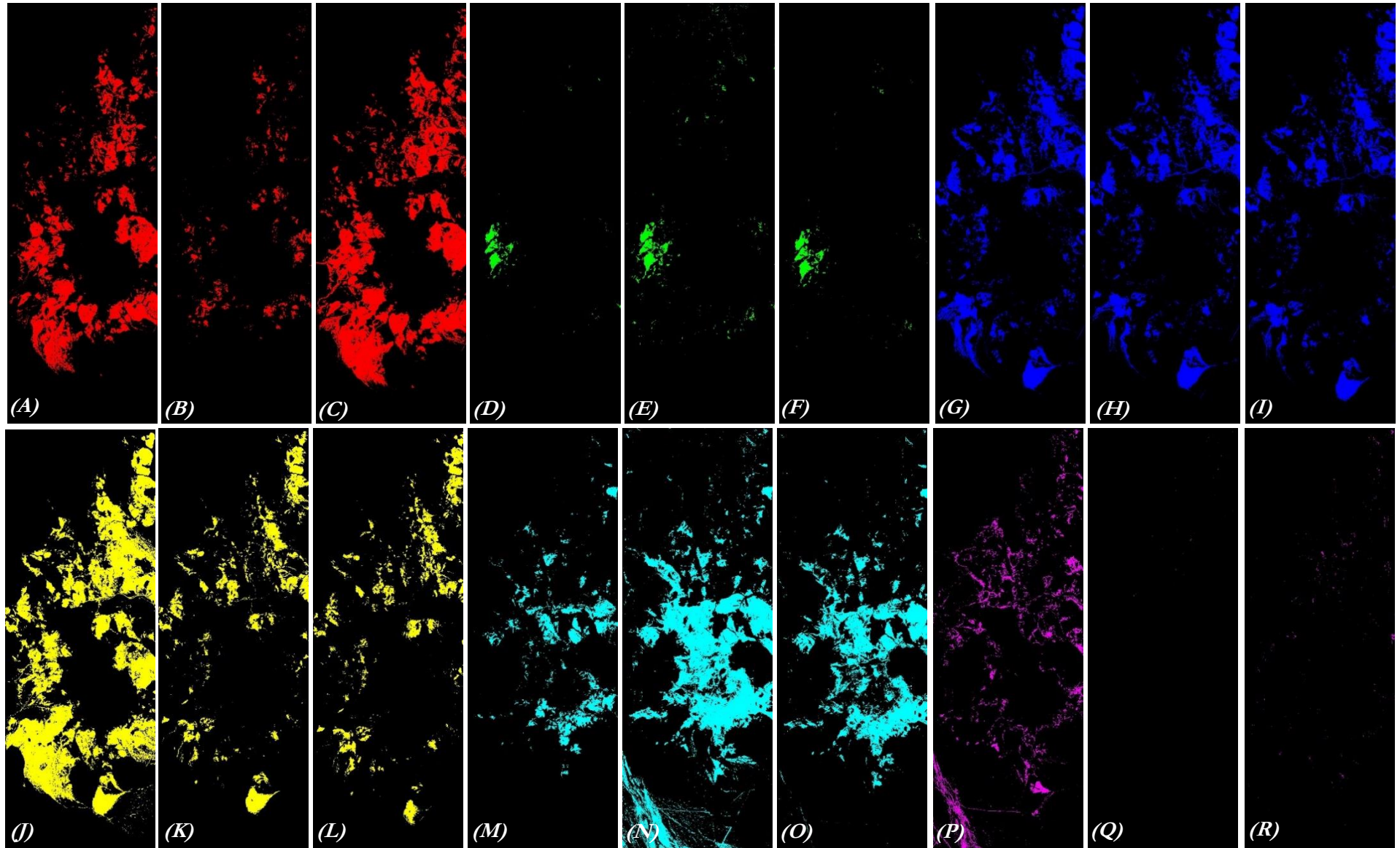
Appendix III. The self-assessment for the GCPs



Appendix IV. The threshold for change detection

Class 1	Change (+7)	> ▾	1200.00		
Class 2	Change (+6)	> ▾	1000.00	and	<= ▾ 1200.00
Class 3	Change (+5)	> ▾	800.000	and	<= ▾ 1000.00
Class 4	Change (+4)	> ▾	600.000	and	<= ▾ 800.000
Class 5	Change (+3)	> ▾	400.000	and	<= ▾ 600.000
Class 6	Change (+2)	> ▾	200.000	and	<= ▾ 400.000
Class 7	Change (+1)	> ▾	0.0000	and	<= ▾ 200.000
Class 8	No Change	= ▾	0.0000	and	= ▾ 0.0000
Class 9	Change (-1)	< ▾	-0.0000	and	>= ▾ -200.000
Class 10	Change (-2)	< ▾	-200.000	and	>= ▾ -400.000
Class 11	Change (-3)	< ▾	-400.000	and	>= ▾ -600.000
Class 12	Change (-4)	< ▾	-600.000	and	>= ▾ -800.000
Class 13	Change (-5)	< ▾	-800.000	and	>= ▾ -1000.000
Class 14	Change (-6)	< ▾	-1000.000	and	>= ▾ -1200.000
Class 15	Change (-7)	< ▾	-1200.000		

Appendix V. The 36 solo mineral maps



(A), (B), and (C) show the distribution of Alunite in May image, Sep image, and Oct image respectively; (D), (E), and (F) show the distribution of Buddingtonite in May image, Sep image, and Oct image respectively; (G), (H), and (I) show the distribution of Kaolinite in May image, Sep image, and Oct image respectively; (J), (K), and (L) show the distribution of Alunite & Kaolinite in May image, Sep image, and Oct image respectively; (M), (N), and (O) show the distribution of Hydrated silica in May image, Sep image, and Oct image respectively; (P), (Q), and (R) show the distribution of Montmorillonite in May image, Sep image, and Oct image respectively.

Appendix VI. The reclassified Cuprite Mineral Map

